Microscopy and Spectroscopy of Graphene: Atomic Scale Structure and Interaction with Foreign Atom Species

A Thesis Submitted to the University of Manchester for the Degree of Doctor of Philosophy
in the Faculty of Engineering and Physical Sciences

2012

Recep Zan

School of Physics and Astronomy

List of Contents

List of figures

and e) STM current image of another Moiré pattern with clearly resolved atomic structure (5nm frame).

Abstract

Since its discovery, the one atom thick material graphene has been at the centre of growing interest in two-dimensional materials. Due to its exceptional properties, graphene is a rich topic to explore by physicists, chemists, engineers and materials scientists. In addition to its use in the fundamental research, graphene is also a promising candidate for future electronics, photonics and energy storage devices.

The project presented in this thesis was carried out to explore the structure of suspended graphene in particular in order to probe the metal-graphene interaction via Transmission Electron Microscopy, as most graphene applications require interfacing with metals. As the work was based on free standing graphene, graphene layers obtained by mechanical cleavage or growth on a substrate were transferred onto TEM-grids. Therefore, fabrication, suspended sample preparation and identification of graphene layers were first discussed for a better understanding of how to obtain high quality graphene, as this was essential for the rest of the project.

Structural, topographic and chemical analysis of pristine suspended graphene layers were investigated in detail via Transmission Electron Microscopy and Scanning Tunnelling Microscopy. The latter technique was also employed for graphene on a substrate along with establishing annealing conditions for residue free graphene.

Metal deposited suspended graphene layers were then investigated in the electron microscopes. Different metal behaviours were observed on the graphene surfaces for the same amount of metal evaporation. Generally, metals interact only weakly with graphene as they are not observed on clean (residue free) parts and are mainly clustered. On the other hand, graphene etching has been observed in the presence of metals. The etching was initiated with graphene vacancy formation as a result of the interaction between metal and carbon atoms on clean graphene. Once a vacancy was created, a hole quickly formed and eventually the graphene layers were destroyed. However, those holes created by metals were healed spontaneously either by non-hexagonal or perfect hexagonal rings. The possible etching and healing mechanisms of the suspended graphene were also discussed.

Declaration

No portion of the work referred to in the thesis has been submitted in support of an application for another degree or qualification of this or any other university or other institute of learning.

Copyright Statement

i. The author of this thesis (including any appendices and/or schedules to this thesis) owns certain copyright or related rights in it (the "Copyright") and he has given The University of Manchester certain rights to use such Copyright, including for administrative purposes.

ii. Copies of this thesis, either in full or in extracts and whether in hard or electronic copy, may be made only in accordance with the Copyright, Designs and Patents Act 1988 (as amended) and regulations issued under it or, where appropriate, in accordance with licensing agreements which the University has from time to time. This page must form part of any such copies made.

iii. The ownership of certain Copyright, patents, designs, trade marks and other intellectual property (the "Intellectual Property") and any reproductions of copyright works in the thesis, for example graphs and tables ("Reproductions"), which may be described in this thesis, may not be owned by the author and may be owned by third parties. Such Intellectual Property and Reproductions cannot and must not be made available for use without the prior written permission of the owner(s) of the relevant Intellectual Property and/or Reproductions.

iv. Further information on the conditions under which disclosure, publication and commercialisation of this thesis, the Copyright and any Intellectual Property and/or Reproductions described in it may take place is available in the University IP Policy (see http://www.campus.manchester.ac.uk/medialibrary/policies/ intellectual-property.pdf), in any relevant Thesis restriction declarations deposited in the University Library, The University Library's regulations (see http://www.manchester.ac.uk/library/aboutus/ regulations) and in The University's policy on presentation of Theses.

Acknowledgements

First and foremost, I would like to express my sincere gratitude to my supervisor, Dr. Ursel Bangert, for her supervision, advice, support, encouragement and care throughout my studies and more importantly for believing in me.

I would also like to thank my supervisor, Prof. Konstantin Novoselov, for giving me a chance to work on graphene as a member of his research group. His humble personality, hard work and dedication were inspiring and motivating for me.

I owe a great many thanks to Dr. Quentin Ramasse for sharing his brilliant microscopy experience as a microscopy genius, helping to carry out STEM experiments, contributing to the publications, editing the thesis and of course, for his invaluable friendship.

I am grateful to Prof. Bruce Hamilton for providing STM opportunity and Dr. Chris Muryn for STM training and helping me to carry out STM experiments. I have learnt many things from him about materials, chemistry and vacuum systems.

I also thank Dr. Alan Harvey for his support and discussions about electron microscopy.

I would like to extend my gratitude to all my group members especially Dr. Rashid Jalil, Dr. Diby Kim, Dr. Reza Jalili Kashtiban (University of Warwick), Dr. Rahul Nair, Thanasis Georgiou and my dearest friend Antonios Oikonomou for their help in the lab and for their friendship outside. I also wish to express special thanks to all the Daresbury SuperSTEM team.

I am thankful to the Ministry of National Education of Turkey for awarding me a PhD scholarship and supporting my PhD studies. Without this scholarship, the completion of PhD thesis could not be possible.

I would like to also thank all my friends, especially Barış Alpaslan, for being in my life.

Furthermore, I am heartily thankful to my dear parents and grandparents. Their encouragement, moral motivation and prayers during my PhD studies have been a continuous source of energy for me, which has been invaluable.

Last but not least, I would like to welcome ‘you’.

List of Publications

- R. R. Nair, P. Blake, J. R. Blake, **R. Zan**, S. Anissimova, U. Bangert, A. P. Golovanov, S. V. Morozov, A. K. Geim, K. S. Novoselov, and T. Latychevskaia, "Graphene as a transparent conductive support for studying biological molecules by transmission electron microscopy," *Applied Physics Letters* **97** (15), 153102-153103 (2010).

- **Recep Zan**, Ursel Bangert, Quentin Ramasse, and Konstantin S. Novoselov, "Metal-Graphene Interaction Studied via Atomic Resolution Scanning Transmission Electron Microscopy," *Nano Letters* **11** (3), 1087-1092 (2011).

- Ursel Bangert, Mhairi Gass, **Recep Zan**, and Cheng Ta Pan, "Scanning Transmission Electron Microscopy and Spectroscopy of Suspended Graphene," in *Physics and Applications of Graphene - Experiments*, edited by Sergey Mikhailov (InTech, 2011).

- **R. Zan**, U. Bangert, Q. Ramasse, and K. S. Novoselov, "Imaging of Bernal stacked and misoriented graphene and boron nitride: experiment and simulation," *Journal of Microscopy* **244** (2), 152-158 (2011).

- **Recep Zan**, Ursel Bangert, Quentin Ramasse, and Konstantin S. Novoselov, "Evolution of Gold Nanostructures on Graphene," *Small* **7** (20), 2868-2872 (2011).

- C. T. Pan, R. R. Nair, U. Bangert, Q. Ramasse, R. Jalil, **R. Zan**, C. R. Seabourne, and A. J. Scott, "Nanoscale electron diffraction and plasmon spectroscopy of single- and few-layer boron nitride," *Physical Review B* **85** (4), 045440 (2012).

- T. C. Lovejoy, Q. M. Ramasse, M. Falke, A. Kaeppel, R. Terborg, **R. Zan**, N. Dellby, and O. L. Krivanek, "Single atom identification by energy dispersive x-ray spectroscopy," *Applied Physics Letters* **100** (15), 154101 (2012).

- **Recep Zan**, Ursel Bangert, Quentin Ramasse, and Konstantin S. Novoselov, "Interaction of Metals with Suspended Graphene Observed by Transmission Electron Microscopy," *The Journal of Physical Chemistry Letters* **3**, 953-958 (2012).

- Quentin M. Ramasse, **Recep Zan**, Ursel Bangert, Danil W. Boukhvalov, Young-Woo Son, and Konstantin S. Novoselov, "Direct Experimental Evidence of Metal-Mediated Etching of Suspended Graphene," *ACS Nano* **6** (5), 4063-4071 (2012).

- **Recep Zan**, Chris Muryn, Ursel Bangert, Philip Mattocks, Paul Wincott, David Vaughan, Xuesong Li, Luigi Colombo, Rodney S. Ruoff, Bruce Hamilton, and

Konstantin S. Novoselov, "Scanning tunnelling microscopy of suspended graphene," *Nanoscale* **4** (10), 3065-3068 (2012).

- **Recep Zan**, Quentin M. Ramasse, Ursel Bangert, and Konstantin S. Novoselov, "Graphene reknits its holes," *Nano Letters* **12** (8), 3936-3940 (2012).

Chapter 1

Introduction

One of the most important goals of materials science research is to identify, exploit and control the properties of new material systems with a view to replacing existing technologies with superior solutions. Durability, flexibility, functionality and adaptability are essential features for any material to be used in emerging technologies and it is widely accepted that a step change in materials design will soon be needed to keep the current pace of technological innovation. The isolation of graphene and of other two-dimensional (2D) crystals around 2004 [1] appears to have provided just that. Often dubbed the 'wonder material', graphene consists of a single layer of carbon atoms arranged in a honeycomb (hexagonal) pattern. It is an allotrope of carbon, one of the most abundant elements on earth which is an essential component of life existing in many different forms from air to soil. Interestingly, until 2004 it was thought that materials could not be thermodynamically stable in 2D form, as theoretical calculations originally predicted [2]. But following the breakthrough of the isolation of graphene and the demonstration of its remarkable properties, the study of 2D materials has become a vast field of research, uncovering a wealth of new physical phenomena. The need to understand and control the properties of graphene in order to apply them to concrete technological solutions brought together scientists from many different backgrounds in a rather uniquely interdisciplinary research field, including material scientists, physicists, chemists and engineers.

In no particular order, graphene is the thinnest [3], strongest [4], most stretchable [5], highest thermally [6] and electrically [7] conductive material known at present. These exceptional properties can potentially be employed for a range of applications from electronic devices to DNA sequencing, to energy storage. One of the most promising electronic applications of graphene is the manufacture of transistors [1]. However, transistors, as any other graphene-based electronic device, must involve the incorporation of metal contacts, which link the graphene to the other device components. The choice of the metal used as a contact has been shown to dramatically affect the performance of the resulting devices [8, 9], with little understanding hitherto of why this is the case. While the macroscopic properties of graphene devices are readily measured and characterised, understanding the metal-graphene interactions necessitates an investigation and direct

‘visualisation’ at the atomic level, which is a remarkably challenging task. Indeed, there are only few reported observations at the atomic scale of the metal-graphene system, especially for suspended (or ‘free-standing’) graphene. A large effort has in fact been recently devoted to suspended devices [10]. Using suspended graphene (rather than supported on a different material) eliminates substrate effects, which are known as a limiting factor for the mobility in graphene based devices [11, 12]. A fully suspended geometry also allows exploiting directly the intrinsic, exceptional properties of the material. It is thus essential to carry out detailed systematic studies of the nucleation following deposition and of the resulting coverage of metals on suspended graphene, in order to determine what the optimal contact might be and ultimately to improve device performance.

Transmission Electron Microscopy (TEM) or Scanning Transmission Electron Microscopy (STEM) are an ideal, perhaps the only, tool for such studies. Indeed, the technique’s ability to image and identify directly each and every atom in 2D materials has already played a significant role in improving our understanding of graphene properties [13, 14]. Rapid progress in microscope components in recent years, in particular the successful implementation of aberration correctors for electron optical lenses, has heralded a new era in materials- and nano- science research. These instrumental advances have substantially improved the overall performance of electron microscopes: much higher resolutions are now attainable in both structural and spectroscopic data, with very clear benefits to the understanding of the investigated material’s structure. More crucially, they enable the use of much lower acceleration voltages (a high voltage, typically ranging from 40kV to 300kV is used to accelerate the electron beam towards the specimen inside the microscope column) whilst maintaining atomic resolution. Structural changes and damage to the specimen due to its interactions with the high energy electron beam can thus be reduced without losing any of the structural details in the micrographs. Most of the results presented in this dissertation were obtained on a Nion UltraSTEM microscope. The additional specificity of this instrument is its ultra-high-vacuum (UHV) design, such that no unwanted contaminants would hinder the observation: when studying a sheet of single atoms, any additional contaminant is nefarious to the experiment! The microscope was operated at 60 kV acceleration voltage to prevent knock-on damage to the graphene [15]. High angle annular dark field (HAADF) imaging was employed to produce micrographs whose intensity is approximately proportional to the square of the average atomic number Z of the material under the electron probe. This chemically-sensitive ‘Z-contrast’ mode is

ideally suited to directly identify the nature of individual atoms and it is usually complemented by further chemical fingerprinting through Electron Energy Loss Spectroscopy (EELS).

The graphene layers used in the project were obtained either by mechanical cleavage or growth on a metal substrate. Following several chemical steps, single layer graphene sheets were transferred onto TEM support grids ahead of metal deposition. A variety of metals were investigated in this project: Au, Cr, Ti and Pd as they are very widely used as contacts in graphene devices, Ni due to its catalytic activity on graphene [16] and Al because of its great potential for energy storage applications using graphene [17]. One of the most striking results of this study revealed that all deposited metals form non-uniform distributions or clusters, which adhere preferentially to hydrocarbon contamination patches (ubiquitous on graphene) rather than to the clean graphene surface [18, 19]. This indicates a very weak interaction between metal and graphene. While this situation can be somewhat improved through chemical modification of the graphene surface, such as hydrogenation [19], high temperature vacuum annealing was demonstrated to be the only way to get rid completely of the hydrocarbon contamination [20]. This is important for instance for *in situ* observations of catalytic activity and of the movement of metal nanoclusters on graphene. It is however not really practical as real-life devices will have to be re-exposed to air and will thus contaminate again. A fascinating etching phenomenon was also observed. Nano-scale holes form in locations where metal clusters are in close proximity with the graphene sheet, and in particular at the border between a contamination patch and pristine graphene [21]. Theoretical models predict that vacancy formation energies in graphene are substantially lowered in the presence of metal atoms [22] and it was indeed observed that the metal atoms appear to catalyse the carbon-carbon bond dissociation and lead to the formation of holes. Some individual metal atoms can occasionally be dragged by the electron beam onto the pristine graphene surface [23], where they can then initiate the etching. Holes form rapidly and expand until the local metal atom reservoir is exhausted. Although for theoretical calculations [22] no oxygen is required in this metal-mediated vacancy formation, it was suggested that oxygen or hydrogen, which are abundant in the hydrocarbon contamination patches, play a vital role and may in fact assist the etching via graphene oxidation or hydrogenation. In further calculations, the oxidation mechanism was found to be energetically favourable over the hydrogenation mechanism. Importantly, etching was not observed in the presence of gold atoms, which of course do not oxidise. The role of the scanning electron probe in the etching process is not perfectly understood.

However, it is suspected that the beam might act as a heat source since graphene etching also occurred in nearby regions not directly irradiated by the beam.

These results might have consequences for the macroscopic electrical transport properties in graphene devices. The presence of contamination appears to be an issue with graphene structures in that it has an effect on the charge transfer between graphene and metals. Furthermore, the observed metal-mediated etching of graphene could provide an explanation for the degradation of device performance over time. This etching could also be exploited in controlled tailoring and self-assembly processes for future graphene based devices as the etched holes can be healed spontaneously. The healing process occurs in a very short time (from few to tens of seconds) and depends on the presence of a local reservoir of loose carbon atoms, such as hydrocarbons on the sample or sputtered atoms from the sheet edges [24]. This completely new observation can be added to graphene's superior properties list as 'self-healing'.

In addition to (S)TEM and EELS investigations, which concentrated on the structural and chemical characterisation of the metal-graphene systems, Scanning Tunnelling Microscopy (STM) was also employed in this project. As a surface sensitive technique, STM can provide topographic information about the samples, along with additional electronic structure data. It was therefore a natural technique to apply when studying the interaction of metals deposited on a flat surface. Furthermore, another important aspect of employing STM was the prospect of performing the metal deposition *in situ*, directly in the STM's UHV environment. This configuration would eliminate any possible oxidation of the metals and would allow for ultra clean graphene surfaces (contamination-free) by annealing the samples to high temperatures (~600 ^{o}C) in the deposition chamber. The annealed surfaces can be expected to be mostly free of hydrocarbon residues, on which the (S)TEM characterisation showed preferential deposition of metal clusters. Preparatory steps were however necessary to develop the experimental capabilities for this study, which resulted in the first observation of free-standing graphene with an STM when all previous reports in the literature used graphene layers placed on a metal substrate [20].

This dissertation consists of eight chapters. Some of the properties of graphene are highlighted in Chapter 2. An introduction to the metal-graphene system is provided and includes a review of previous studies using TEM and STM, as well as transport properties measurements.

Chapter 3 discusses the methodology and instrumentation used in this work: graphene fabrication, suspended sample preparation for TEM and STM, metal deposition, electron

and probe microscopy, (S)TEM and STM instrumentation as well as some technical details of the graphene characterization through (S)TEM and STM.

A more thorough discussion of graphene characterization using TEM and electron diffraction is provided in Chapter 4, while the first STM observation of suspended graphene is presented in Chapter 5 with details of the sample preparation methodology and the adapted measurement techniques that made this technical accomplishment possible.

In Chapter 6 the interaction between deposited metals and graphene is studied in detail. Different metals are considered, varying in a carefully controlled way the coverage of both pristine graphene sheets and of chemically-modified (hydrogenated) graphene surfaces.

Graphene etching in the presence of the metals is discussed in Chapter 7 from both experimental and theoretical perspectives. The theoretical work, based on Density Functional Theory (DFT) simulations, was undertaken to support the experimental observations. A novel phenomenon of graphene healing is also presented along with possible lattice re-knitting scenarios that might lead the healing process.

Finally, this study is summarized in Chapter 8 with an outlook of future work on the interaction of metals with graphene and with other 2D materials.

The work carried out within this project has been published in various scientific peer-reviewed journals. Material from some of these publications is used extensively in Chapters 5, 6 and 7. For completeness, the original papers are attached to each of these chapters.

Additionally, most of the electron microscopy data presented in the thesis were obtained at Daresbury SuperSTEM Laboratories, which is a National Facility for Aberration Corrected (AC) STEM, with the help of Dr. Quentin Ramasse and DFT simulations were performed with collaboration Dr. Danil Boukhvalov, Korea Institute for Advanced Study, Korea.

Chapter 2

Graphene Background

Graphene, just one atomic layer, is a two dimensional crystalline form of carbon and a basic building block for carbon allotropes such as fullerene, carbon nanotubes and graphite [1, 25]. Although it was initially thought that 2D crystals could not exist due to thermal fluctuations, the first single layer sheet of graphite, or graphene, was first isolated in 2004 followed by other examples 2D crystals in 2005 [3]. In graphene, carbon atoms are packed in a planar honeycomb network. The unit cell of single-layer graphene consists of two carbon atoms, separated by 1.42 Å, with a lattice constant of 2.46 Å. These two carbon atoms are equivalent and have the same potential. Each atom has s, p_x and p_y orbitals and is bonded to three neighbour atoms in the lattice, forming an sp^2 atomic network. The p_z orbitals overlap between neighbouring atoms resulting in so-called filled π and empty π^* states, which respectively form the valence and the conduction bands in graphene. However, so-called Bernal stacked bi-layer graphene has four electrons in the unit cell: in this configuration, the individual layers are stacked but shifted with respect to one-another, so that the carbon atoms in one layer sit on top of the empty hexagon centres in the underlying layer. The electronic behaviour of a small number of stacked graphene layers (also called 'few-layer graphene', up to approximately 10 layers) thus differs substantially from the single layer case, but also from bulk graphite [25], due to overlapping between the conduction and valance bands. For instance, electrons behave in single-layer graphene as if they were mass-less, relativistic fermions, and exhibit a linear dispersion near the Dirac point. By contrast, in so-called bi-layer graphene, electrons are described as non-zero effective mass Dirac fermions with a parabolic electronic dispersion [1]. This unique electronic structure makes single layer graphene such a fascinating material to study: it possesses high carrier mobility [1], ballistic transport [25], quantum Hall effect [26], thermal conductivity [6] and mechanical strength [4]. Another interesting property of graphene shows ambipolar behaviour in an electric field as result of its mass-less Dirac nature. Charge carriers can be tuned by electric field to be either electrons or holes (doping) in the graphene at very high concentrations [1, 3]. Mass-less carriers in graphene also lead to absorption of normal incident light (2.3%) independent of the wavelength [27,

28]. In other words it is transparent and its unique 2D structure suggest it can be utilized in flexible display in electronic devices, such as touchscreens [28]. But arguably one of the most interesting and promising feature of graphene that can be employed in electronic devices is its high carrier mobility. Recently measured values of ~150 000cm^2/Vs [29] (interestingly, this is comparable to the theoretical prediction of 200 000cm^2/Vs for pure suspended graphene) are significantly higher than in silicon (~1400cm^2/Vs) [30], which most of today's electronics are based on. Graphene could thus be used in transistors to increase their operational speed. Poor electrical contacts (junctions) and defects such as ad-atoms, ad-molecules or vacancies, can however deteriorate the mobility [31].

Due to the absence of any measurable band gap in both single- and bi-layer graphene these materials are often called zero-gap semiconductors. The lack of a bandgap is a serious limitation to the use of graphene in electronics as switching off any graphene-based device would be extremely difficult. As a result of the gapless nature of graphene, graphene devices have only demonstrated to date a mere ~10^3 on/off ratio, far behind required value of ~10^6 used in logic transistors [28]. Thus band gap 'engineering' and increasing the on/off ratio are essential research areas in graphene electronics. By creating a potential difference between the atoms in the unit cell or by breaking the symmetry in the lattice, it is nevertheless possible to 'open' a bandgap and thus engineer graphene 'variants' that may be more useful from an electronics applications point of view. However, due to the small separation between the atoms, creating such a potential difference is extremely difficult. Researchers have therefore developed many techniques to modify graphene and introduce a bandgap, including the reduction of its dimensionality (graphene nanoribbons and quantum dots) [32, 33], the introduction of defects [34], doping by exposing graphene to gases, ad-atoms and molecules [35-37], and the application of an electric field (in case of bi-layer graphene) [38].

Reducing the material's dimension from 2D to 1D by shaping it into a thin strip or nanoribbon can open a bandgap in graphene through the 1D confinement of the electrons. However, the nanoribbon should be less than 10 nm-wide to open a reasonable (*i.e.* useable) bandgap (200meV), which seriously limits the practicality of this technique. Indeed, it was shown that the nanoribbon and band gap width are inversely proportional: the narrower the nanoribbon the bigger bandgap [33]. Unfortunately, reducing the size of the nanoribbon to open a bandgap has the nefarious additional effect of reducing the carrier mobility. Moreover, the exact geometry of the ribbon's edges, which is extremely difficult to control accurately, also has an enormous influence on the ribbon electronic properties

[33, 39]. Applying strain [40] or varying the substrate [41, 42] the graphene sheet is placed on can also be used to open a band gap in single layer graphene. Bandgaps of the order of few hundreds of meV have been reported in the case of 1% uniaxial tensile strain and of a few meVs when deposited on various substrates. Again, from an applications point of view, these values are too small to be practical.

The deposition of a single layer of graphene over hexagonal boron nitride (h-BN), which is an insulator and whose structure is similar to that of graphene, was predicted to be able to open a bandgap [41]. A gap opening of up to ~0.26 eV has been also been demonstrated for graphene epitaxially grown on silicon carbide substrates [42]. As in the h-BN case, this is explained by the symmetry breaking in the lattice due to the interaction between the graphene and the substrate.

None of the above techniques is able to open a gap of more than 0.36 eV [28], and as a result the most promising method to open a band in graphene arguably remains chemical modification or doping. Substitutional doping of the carbon lattice with similar-sized-elements such as B and N can indeed open a bandgap in graphene: this effect was predicted by DFT simulations and demonstrated experimentally [43]. Importantly, carrier type and concentration can also be controlled through this mechanism. For example, introducing B atoms within the graphene lattice leads to p-type doping as B has one fewer electron than carbon. Similarly, introducing N leads to n-type doping in graphene. Other avenues for doping graphene are also being investigated: water molecules on graphene have recently been shown to open a reasonable bandgap of ~0.206 eV. Adsorbed water molecules act as defect centres and their amount can be easily controlled by the absolute humidity level [44].

A technique known as hydrogenation, which consists of exposing graphene to atomic hydrogen, has also been used to successfully open a bandgap [45]. It is thought that the atomic hydrogen reacts and binds with each of the carbon atoms in the lattice, converting the sp^2 graphene bonding network to a diamond-like sp^3 bonding type with some insulating character. Crucially, hydrogenation was shown to be a reversible process: the properties of pristine graphene can be recovered by thermal annealing after the initial hydrogenation. Experimental observations of this effect were also reported after adsorption of atomic hydrogen onto graphene grown and still supported on Ir (*i.e.* not suspended graphene) [46]. It appears the band gap can be tuned by varying the hydrogen coverage of the graphene surface: full surface hydrogenation was shown to result in a bandgap of ~0.73 eV, while half-hydrogenated graphene yielded a bandgap of only 0.43 eV [47]. Furthermore,

fluorinated graphene, which is obtained by exposing graphene to xenon difluoride gas is thought to turn graphene into a wide-gap semiconductor or insulator with an optical gap of 3 eV [48].

Finally, theoretically calculations predict that a bandgap can be opened in Bernal stacked bi-layer graphene by applying a strong electric field perpendicular to the layers [49]. This effect was experimentally demonstrated for epitaxial graphene grown on a silicon carbide surface [38]. This bandgap could in principle be tuned by varying the external electric field, and a tunable bandgap of few hundred meV was indeed experimentally demonstrated for electrically gated bi-layer graphene using an oxidised silicon (SiO_2) substrate as well [50, 51]. It should be mentioned that devices made using bi-layer graphene have also shown a dramatic improvement in their on/off current ratio (albeit at the very low temperature of 20 K) [51].

Researchers have shown that the substrate on which graphene layers are placed has dramatic effects on its transport properties. Graphene devices were initially fabricated on SiO_2/Si substrates: graphene flakes were simply obtained by exfoliation directly on top of them. The use of SiO_2 substrates for graphene exfoliation is particularly convenient and straightforward. Unfortunately, due to their surface roughness and to the presence of charged impurities graphene devices built directly on SiO_2 substrates could not demonstrate any marked improvement over more traditional designs: they were seemingly never able to utilise the intrinsic properties of graphene [52]. The limiting role of the substrate can be understood by comparing graphene device performance with that of suspended devices, which eliminate any substrate effect. For example, the mobility in graphene devices is about 10 000 $cm^2V^{-1}s^{-1}$ on SiO_2 but can reach up to 200 000 $cm^2V^{-1}s^{-1}$ for suspended devices [53]. Suspended devices are particularly fragile, however, and their handling and fabrication is difficult. Other substrates such as hexagonal boron nitride (h-BN) [52, 54] and recently dichalcogenides [55] have therefore been tried as support. h-BN consists of boron and nitrogen atoms arranged in a hexagonal structure such that each boron atom is bonded to three neighbouring nitrogen atoms and *vice versa*. The resulting structure resembles graphene, with a similar lattice constant of 2.52Å (compared to 2.46Å for graphene). However, in contrast to graphene, h-BN has a large bandgap of 5.97 eV, which makes it the thinnest possible insulator. When stacked, h-BN adopts a so-called AA' configuration whereby each boron atom sits atop a nitrogen atom, and *vice versa* [56]. By contrast, graphene is most frequently observed in an AB stacking arrangement where the two stacked layers are displaced by half a lattice vector. In addition, h-BN is mostly inert,

its surfaces missing dangling bonds, and it has large optical phonon modes, making it an ideal substrate for high-quality graphene electronics [52]. Carrier mobility measurements of graphene devices placed on h-BN substrates show great promise, with reported values up to 500 000 $cm^2V^{-1}s^{-1}$ at liquid helium temperature [29].

Fabricating such a device of course requires the transfer of graphene flakes on top of an h-BN substrate. Different techniques were thus developed to achieve this geometry, which can typically be grouped in two categories, known as wet and dry transfers [57, 58]. The precise alignment of graphene flakes relative to the h-BN layers is crucial as it can affect device performance. As previously mentioned, it was even theoretically suggested this geometry may lead to the opening of a bandgap [41].

Finally, recent results suggest that dichalcogenides such as MoS_2 and WS_2 could also be appropriate substrates for graphene device fabrication. By stacking graphene and h-BN layers, graphene and MoS_2 layers, or through a combination of the above, a new type of graphene device, a layered heterostructure device can be created. These new devices are built vertically and based on ballistic transport [55].

2.1 Graphene Applications

Due to its unique properties, graphene can be employed in a variety of applications. It is thought it may eventually replace many of the materials currently used in today's technology and result in higher performance, energy efficiency, flexibility and durability [28]. Graphene is already being used in electronics (prototype devices) [55, 59], energy storage [60, 61], photonics [62, 63], composite materials [64], sensor technology [65] and as a sample support for TEM applications [66]. The most promising and extensively studied area is its use in high frequency transistors, where graphene-based solutions can already compete with traditional semiconductors such as GaAs. However, the absence of a band gap in graphene, resulting in low on/off ratios, means that a practical use of graphene in logic transistors is not yet a reality. However, the use of graphene in electronics is not limited to transistors. It can also be integrated in flexible electronics as a transparent conductive coating thanks to its low resistance properties: commercial graphene-based flexible touch screens and organic light emitting displays are in fact expected in the coming months [28, 59]. Thanks to its conductivity, inertness and large surface area (high aspect ratio) graphene is ideal for composite materials. Graphene-based composites have been used as protection barriers against corrosion, fillers in carbon fibres, and strain

reducing element in polymers [67]. Graphene can also be used in energy storage applications such as batteries and capacitors to enhance their performance and reduce their size [60, 61, 68]. Graphene is used as transparent conductive electrodes in solar cells and as anode in lithium-ion batteries [61]. Having two identical surfaces makes graphene particularly attractive for use in sensor applications such as gas, strain, pressure and magnetic field sensing.

Finally, graphene is now widely used as sample support for TEM in both material and life sciences enabling the observation of metal clusters [69], molecules [70], bio-particles [71] and sequencing of DNA molecules [72]. The background signal generated by a graphene support is extremely weak compared to other available solutions (such as amorphous carbon or Si films, all of which are at least a few nm thick) resulting in a dramatic increase in the signal-to-noise ratio in the TEM images. Although crystalline (which is not an attribute normally sought after in a TEM support), the graphene lattice can most of the time be easily subtracted from the TEM micrographs by Fourier filtering, thus enabling the direct visualisation of particles for both material and biological specimens [73, 74]. The excellent electrical and thermal conductivity of graphene also increases the stability of the sample under the electron beam by minimizing the charging effect.

2.2 Graphene Fabrication

In order to be able to use graphene in various applications, developing scalable sample fabrication techniques is essential [75]. Several methods have been developed in recent years, including: i) mechanical cleavage [1], ii) epitaxial growth (SiC) [76], iii) chemical vapour deposition (CVD) [77-79], iv) chemical reduction [80] and v) liquid phase exfoliation [81, 82].

The mechanical cleavage or mechanical exfoliation method was the first ever used method to isolate graphene. Graphene layers are obtained by progressively peeling a thick graphite crystal using a strip of adhesive tape. The tape is then pressed onto a substrate, such as an oxidised silicon wafer, quartz, glass or mica, ‘depositing’ the exfoliated graphite flakes. Few-layer graphene flakes are easily obtained in this fashion, but it is far more difficult to peel off single-layer graphene flakes, which are also generally of limited size (from a few microns to a few hundred microns). The size of the single-layer graphene regions produced by exfoliation depends on the quality and uniformity of the starting graphite slab, as well as the carefulness during the fabrication process. In particular, great

attention must be paid to the pre- and post-cleaning and baking steps. Despite the limitation on the size of the graphene flakes, mechanical cleavage is a very reproducible and reliable technique for the fabrication of high quality graphene: the very good crystallinity of the resulting flakes makes them particularly suitable for use in electronics applications (transistors). Graphene produced by exfoliation still outperforms material obtained by any other means.

Thin graphene layers can be also obtained by graphitization in vacuum of a SiC single crystal, through silicon depletion of the exposed surface [76]. Although these so-called 'epitaxial graphene' layers can be produced in wafer size with this method, they tend to be fragile and contain many defects due to the large lattice mismatch between the SiC substrate and the graphene. Further limitations for the large-area synthesis of epitaxial graphene are: the cost of SiC substrates, the processing conditions at high temperature (~1400 ^{o}C) and very high vacuum (~10^{-10} Torr), which all contribute to increasing the total cost. On the other hand, epitaxial graphene is by definition already on a dielectric substrate (SiC) and can thus be used directly for device manufacturing, which in some cases is a great advantage. But it also means the graphene layers cannot be transferred to an arbitrary substrate, which may be seen as a limitation. The epitaxial growth of graphene on SiC is still under active development and further optimization is probably needed before the technique can become more widespread [28].

Due to the high demand for graphene and other 2D materials, alternative, more easily scalable methods have been developed. Chemical vapour deposition (CVD) on metal substrates is perhaps the most common large scale growth technique [77] yielding quite uniform samples with a higher fraction of single layer areas than exfoliated graphene [59]. The growth mechanism is based on the decomposition of hydrocarbon gases at elevated temperature and the diffusion of carbon atoms onto a metal surface, followed by rapid cooling to 'freeze' in any graphene layers formed on the surface of the substrates. Hydrocarbon gases, such as methane (CH_4), acetylene (C_2H_2) and benzene (C_6H_6), are brought into contact with the metal substrates like Ni, Cu, Ru, Ir, Co and Pd at high temperature in a CVD chamber that kept at low pressure [83-85]. Key parameters for the fabrication of large areas of graphene with low defect density by the CVD method are the temperature stability, the purity of the hydrocarbon gas sources, their flow rate (H_2/C_xH_x), the overall growth times, the exact chamber pressure, the cooling rate and crucially the purity of the metal substrates.

The most widely used combination at present consists of methane gas and a copper substrate; the low solubility of carbon in copper provides a means of restricting the graphene growth to a single layer (rather than 'thicker' graphene obtained on other metals) [78]. Here the growth is initiated by the adsorption of C at the Cu crystal surface, rather than through a precipitation process like for graphene growth on nickel as has been reported by Reina *et al.* for instance [77]. For the latter, non-uniform graphite films with thicknesses ranging from single to a few layers are typically obtained: the solubility of carbon in Ni is relatively high and any excess carbon precipitates readily, which makes controlling the number of layers difficult and explains why Ni is not favoured anymore as a substrate for graphene growth.

Graphene flakes obtained on metal surfaces need to be transferred for subsequent characterisation, in particular to be able to perform transport measurement, for which an insulating substrate is needed. Although many transfer methods were developed with a hope to obtain fully crack-less, clean (contamination-free) and defect-free flakes after transfer [57, 58], the electronics properties of the flakes are still often deteriorated to the extreme. The carrier mobility measured on CVD-grown graphene layers ranges only from a few hundred to a few thousand cm^2/Vs, much lower than for graphene obtained via exfoliation (~10 000 cm^2/Vs on SiO_2). It is thought that the presence of grain boundaries due to the multitude of nucleation sites for the growth on the metal surface, defects and impurities that can be induced during transfer process, are responsible for the reduced performance.

In order to overcome the production costs and to be able to produce large amounts of graphene for industrial application, chemical routes such as exfoliation of graphite in solvents are often favoured. For example, graphite powder can be initially oxidised in acids to ease the exfoliation process in the liquid phase. The resulting graphene oxide is then reduced either thermally or chemically to obtain graphene [80, 86]. Graphene obtained in this fashion is also known as chemically-modified graphene because hydroxyl groups often remain on the surface. Although the reduction step is designed to get rid of some of the impurities [80], O^- and OH^- groups on the surface as well as structural defects generated during the oxidation process persist in the final material. Thus, beside the small size and low percentage of single layer flakes obtained through this process, the properties (and in particular the conductivity) of the resulting graphene material are also poorer. Further development and progress are needed to obtain purer graphene through reduction of graphene oxide. On the other hand, the liquid phase exfoliation of graphite powder in

organic solvents such as NMP has been demonstrated as a more efficient way to obtain graphene. The graphene layers obtained with this technique are unoxidised, defect free and mainly less than 5 layers as evidenced by X-ray photoelectron spectroscopy, Raman spectroscopy and TEM-diffraction analysis [81, 82]. The great potential for up-scaling and the remarkably low cost of this technique make it perhaps the most viable solution to date for industrial production of graphene and other 2D materials [87]. This technique has its own limitations (disadvantages) to be used in electronics e.g. transistors due to small size of single layer flakes and obtaining those with mixture of thicker flakes. However, the graphene flakes obtained via this technique can be used to produce graphene based composites or films, solar cells and lithium-ion batteries.

2.3 Graphene Identification

Identifying graphene flakes and distinguishing between single- and multi-layer areas in thicker flakes is essential as the number of layers will determine the properties of the material. Optical Microscopy [1, 88], Raman Spectroscopy [89], Atomic Force Microscopy (AFM) [1], Transmission Electron Microscopy (TEM) [14] and Electron Energy Loss Spectroscopy (EELS) [13, 90] are some of the techniques that can be used for this purpose.

Light microscopy is one of the preliminary techniques used in any graphene identification process. It is a quick and convenient method to identify and locate graphene layers reliably, especially when working with material obtained via exfoliation on a substrate. Because the size of the graphene flakes is much smaller (microns) than the full wafer width (cm), being able to quickly search across a wide field of view is essential. The identification is relatively straightforward, the optical contrast changes continuously as the layers get thicker [88]. Other experimental techniques should however be employed for more accurate results, in particular if the identification of the precise number of layers is essential.

Raman spectroscopy is perhaps the most straightforward technique to identify graphene layers at the macroscopic level [89]. Depending on the presence of single-, double-, and few-layer areas, the reflections observed in the Raman spectra change dramatically, which allows for an unambiguous, high-throughput and crucially non-destructive identification of the number of graphene layers. Raman spectroscopy is also sensitive to defects and contamination, which can be used to check the quality of the observed graphene. A particular peak in the spectra, called the D-peak, is associated with

defects and disorder and is distinguishable from the peaks used to identify the number of layers (2D- and G-peaks). The amount of doping present in graphene layers can be also identified by Raman spectroscopy by observing shifts and intensity variation in the Raman peaks. With similar observations, Raman spectra can be also used to evaluate the majority type of graphene edges present in a particular flake [91]. For obvious spatial resolution reasons (~800 nm), this characterisation is not entirely conclusive.

Another technique to determine layer numbers uses *AFM*. It is based on measuring the thickness of the flakes by comparison with a substrate of known thickness. Although it can be very precise and reliable, AFM is a low throughput technique for counting layers, and any surface roughness of the substrate can be misleading.

Finally, one of the most unambiguous methods to determine the number of layers in graphitic flakes is *TEM*, in particular through the analysis of electron diffraction patterns [92]. Suspended graphene samples are used for all TEM studies which includes transferring the graphene layers from substrates to grids unlike most of the other techniques that generally do not require the graphene layers to be suspended. A more thorough discussion of these methods will be provided in Chapter 4.

2.4 Tailoring the Atomic Structure of Graphene

2.4.1 Defects in Graphene

Defects whether they are introduced deliberately or formed intrinsically are important in crystals and in particular in 2D materials as they can affect the material's structural, electronic, mechanical and even magnetic properties [93]. These effects can be employed intentionally to modify materials systems and engineer specific, desirable properties. In the case of graphene, defects act as scattering centres that reduce carrier mobility, thermal conductivity, and affect the mechanical properties due to weaker bonding in the vicinity of the defects [93-96]. Different techniques can be employed to create defects in the graphene lattice: from a simple interaction with energetic electrons in a TEM, to controlled bombardment by heavy particles (Ar-ion or Au atoms by pulsed laser deposition) [97], exposure to oxygen plasma [98] and chemical treatment [99]. Different types of defects have been observed in graphene: point defects (such as interstitial ad-atoms) and grain boundaries [93, 100].

Point defects are usually formed in graphene as result of bombardment with energetic particles (electrons [101] and ions [102]). The main types of point defects typically

observed in graphene are: single-vacancy, double-vacancy, Stone-Wales defect and ad-atoms (interstitial or substitutional). A single vacancy is the simplest type of defect and consists of a single missing carbon atom in the lattice, for instance ejected from the lattice when the transferred energy from an incoming beam of particles is higher than the displacement threshold. One of the most interesting and unique properties of graphene defects is their propensity for structure reconstruction. When a defect is created in the graphene lattice, the surrounding carbon atoms tend to undergo a spontaneous reorganise, leading to a different arrangement that complies with specific symmetry rules. For instance, a single vacancy will typically be accommodated through the rearrangement of the lattice into a pentagon (5-membered ring) and a nonagon (9-membered rings) ($V_{5\text{-}9}$) [103]. By contrast, a double vacancy is formed either by merging two single vacancies or by removing two neighbouring carbon atoms from the lattice. After reconstruction, four hexagons are replaced by two pentagons and one octagon ($V_{5\text{-}8\text{-}5}$). This structure can further evolve by bond rotations to more energetically favourable configurations such as a combination of three pentagons and three heptagons ($V_{555\text{-}777}$) or of three pentagons one hexagon and three octagons ($V_{555\text{-}6\text{-}777}$), the former being the most energetically stable arrangement [93]. Theoretical calculations suggest that the formation of a double vacancy is favoured over single vacancies [93, 104]. However, if more than two carbon atoms are removed from the lattice the subsequent rearrangements would be more complex: the graphene layer has to be bent (deformed in the third dimension) to satisfy geometric boundary conditions. An alternative would be for the hole to be filled with only pentagons and heptagons: although predicted theoretically, this arrangement was never observed so far experimentally [105]. The filling of large holes in graphene with a mixture of 5-, 6- 7- and 8-membered rings into a quasi amorphous 2D structure was nevertheless very recently observed [24]: these results are discussed in great detail in Chapter 5.

So-called Stone-Wales defects are created by simple 90^{o} bond rotation of any carbon bond in the lattice, rather than through the ejection of atoms: as a result, they can be created by irradiating the graphene sheet with a lower energy beam than the knock-on threshold for carbon [106].

Finally, mobile adsorbents, either carbon or foreign species such as silicon (one of the most abundant contaminants in graphene) can also participate in filling holes [21]. Ad-atoms or adsorbents are trapped at defective sides, their mobility being decreased in these regions by the lattice symmetry interruption, and point defects are therefore preferential sites for the incorporation of foreign atoms in graphene [73, 95].

2.4.2 Graphene Edges

Graphene sheets can be terminated by two different edge types and due to their appearance called ‘zigzag’ or ‘armchair’ edges, which are differentiated by the position of the hexagons along their length. Due to having an unpaired electron the zigzag edges are chemically more reactive than armchair edges. Graphene edges can be easily investigated either by specifically fabricating thin strips of material also called nanoribbons [91] or simply by damaging a single layer of graphene and observing the structure of the resulting perforation [107].

Nanoribbons are obtained using various methods such as e-beam lithography [108], chemical treatment [91], CVD growth [109], electron beam sculpting in the TEM [110], cutting by metals [111, 112] or even ‘unzipping’ of carbon nanotubes [113]. The type of edges determines the electronic behaviour of graphene nanoribbons. For example, zigzag edges are metallic and armchair edges can be either metallic or semiconductors [39, 114]. The mechanical, elastic and chemical properties of graphene nanoribbons also depend on their edge configuration. It is therefore quite important to identify and understand the edge structure: HRTEM is perhaps the most straightforward tool for this purpose. Zigzag edges were found to be more stable under electron beam than armchair edges in recent TEM studies [107, 114].

Once a vacancy is formed in the graphene lattice, the removal of neighbouring carbon atoms is much easier as the threshold for their ejection is lowered [115] due to a smaller number of dangling bonds. A hole is then created in the lattice, which can be terminated either with zigzag or armchair edges, or as recently demonstrated by a mixture of both. The latter was in fact suggested to be a reconstruction of zigzag edges with non-hexagonal rings. This new type of edges that was dubbed ‘reczag’ and is expected to have higher stability comparing to other types of edge structures [116].

2.5 The Metal-Graphene System

The understanding of the metal-graphene interaction is significantly important to improve graphene-based devices as metals are being used for contacting, patterning and cutting of the graphene layers. In particular, the stability of metals on the graphene surface, their distribution, bonding, doping should be well understood. Metal-graphene interactions have been studied predominantly by means of DFT calculations so far, while any experimental exploration has been limited. A short review is presented here of the

information gathered so far on this system, from both experimental (TEM, STM, Raman and transport measurements) and theoretical (DFT- and Molecular Dynamics- simulations) points of view.

2.5.1 Interactions with the Graphene Surface

There are only few TEM-based metal-graphene interaction studies, arguably because the tools to observe the system at true atomic resolution have only been recently developed. The first TEM investigation was performed for Au and Pt on few-layer-graphene by Gan et al. [117]. The metals were found to be in cluster form and not stable (extremely mobile) on the graphitic structures, which was due, it was suggested, to a stronger interaction between gold atoms than between a gold atom and the graphene [118]. The tendency of metals deposited on graphite to cluster is well-known, especially when the deposition is performed at room or elevated temperatures. Because no metal atom was seemingly observed sitting on top of the graphene plane, it was claimed they systematically occupied double or triple vacancies sites (the small size of single vacancies making it unsuitable to host Au or Pt atoms). These observations received theoretical support, with a suggested diffusion mechanism whereby Au is in single vacancy sites would merge with neighbouring double vacancies, followed by diffusion into a triple vacancy [119]. Other calculations verified that it was energetically favourable for all metal atoms to form clusters at defect sites [120, 121].

Metal species were found to be quite mobile on graphene at room temperature [117, 122, 123], which DFT simulations for the case of gold suggested was due to a weak interaction between graphene and the metals [124, 125]. However, this high mobility can be mitigated in the presence of defects, which can act as trapping centres [120, 123, 126]. Metals occupying monovacancy sites should not move at room temperature [122], a prediction which is compatible with other theoretical results [119] but contrary to the observed high mobility of the transition metal ad-atoms on pristine graphene. The attraction mechanism for ad-atoms (metal or even carbon ad-atoms) and the subsequent reconstruction of the lattice are attributed to either a breaking of the sp^2 nature of graphene that results in hybridization with the orbitals of the attached metal [121] or to local strain around defects [122]. Strain has indeed been employed to functionalize and dope graphene layers [125] while in a separate study, based on DFT calculations, is found that applying a reasonable tensile strain (~10%) in graphene decreases the adsorption energy barrier for metal clusters by at least 100% [127]. Larger bonding energy of ad-atoms on defective

graphene in comparison to pristine graphene surface also explains the reason for their stability. It is also interesting to note that graphene edges (zigzag) were found to provide more favourable sites for ad-atoms due to having more dangling bonds than a planar sheet [123, 128].

Researchers also proposed that hydrogen ad-atoms on graphene can trap small molecules to specific sites, the molecules remaining stable at room temperature. Attaching hydrogen ad-atoms to the graphene surface could thus be used to alter the properties of graphene with specific molecular groups [129]. This suggestion was one of the motivations for the study of metals on hydrogenated graphene detailed in Chapter 4.

Finally, although the displacement of heavy metal atoms by electron irradiation is more difficult than the displacement in identical conditions of carbon atoms in graphitic layers [117, 130], researchers have shown that large metal clusters can be broken into small clusters of a single to a few atoms under a highly focused and intense electron beam, giving the appearance of decorated graphene layers [19, 131].

2.5.2 Graphene Etching via Metals

In graphene-based device fabrication, metals are used for patterning purposes, catalysing in a controlled way the cutting and etching of graphene sheets [99, 108, 132]. Although shaping graphite layers in a gaseous environment using catalytic metal nanoparticles is a relatively well-known technique [111, 133], its usage in single- and few-layer graphene has only been recently demonstrated [16, 134]. The etching of graphene layers in the presence of metals is due to either by hydrogenation or an oxidation mechanism. For the former; the metal nanoparticles (such as Fe, Ni and Co) are deposited on the graphene surface and annealed at reasonably high temperatures ranging from 600 to 1000^{o}C. During annealing the samples are also exposed to a mixture of hydrogen and argon gas. Hydrogen atoms are thought to be adsorbed at the surface of the catalyst metal nanoparticles. Following the dissociation of some carbon into the nanoparticles or at the metal-graphene interface, hydrogen and carbon atoms can interact and eventually destroy/etch the graphene by methane formation. The metal particles only participate as a catalyst in the process as they are systematically left on the surface after the reaction is terminated. A controlled hydrogen gas flow was found to be crucial for this catalytic behaviour, as annealing in a gas-free environment (or using only a pure Ar) did not result in any graphene etching [134]. The suggested oxidation mechanism is quite similar and

relies on oxygen adsorption at the surface of metal nanoparticles, followed by a direct interaction with the carbon atoms of the graphene lattice, resulting in an etching of the graphene and the formation of CO and CO_2 [111]. The width of the produced perforation of the graphene is directly related to size the particles [133]. The length of the perforation is related to gas flow and to the heating and cooling rate during annealing [16].

Almost all these results involved the *ex situ* examination of the samples using scanning probe microscopy, AFM or STM, the graphene layers being placed on a conductive substrate. Graphene cutting using metal nanoparticles has also been demonstrated on suspended graphene using *in situ* TEM, where the effect can be observed in real time. The channelling of silver nanoparticles in graphene is performed under oxygen flow at elevated temperature (300-500^{o}C) and the suspended graphene membrane is cleaned in the microscope column at 500^{o}C for 5 hours ahead of the metal deposition (which is carried out *ex situ*) to reduce contamination on the graphene surface [112].

While the catalytic behaviour of metal nanoparticles for graphene and graphite tailoring is well-known, the same effect was recently demonstrated for non-metallic species such as SiO_x nanoparticles [135, 136]. SiO_x nanoparticles are typically not deposited from an external source but rather formed during annealing of graphene layers fabricated on SiO_2/Si substrate. When the graphene layers are further annealed under hydrogen or oxygen flow, graphene hydrogenation [135] and oxidation [136, 137] are also suggested as possible etching mechanisms, as was the case for metals. The use of SiO_x nanoparticles may in fact be more applicable for device fabrication technology, as this particular form of etching was found to provide well-defined edge orientations (zigzag). The graphene is furthermore already on a SiO_x/Si wafer and therefore needs no further flake transfer that could introduce damage and impurities.

2.5.3 Doping effects and Electronic Structure Alterations

The effect of metal doping in graphene has been investigated by transport measurements and by DFT simulations [8, 138]. Depending on their behaviour on graphene, metals can be divided into two categories, exhibiting either weak or strong adsorptions. Weakly adsorbed metals (Al, Cu, Ag, Au and Pt) do not significantly alter the graphene band (electronic) structure. The doping effect is subtle and results from a charge transfer to or from the graphene [36, 125]. By contrast, strongly adsorbed metal ad-atoms (Co, Ni and Pd) can modify the graphene electronic states to a large degree and even

destroy any π-band dispersion. This would indicate covalent bonding with a strong hybridization between the metal ad-atom's (d-) and graphene (π-) bands [36, 125, 139]. On the other hand, metal ad-atoms from groups I–III are thought to bond ionically to graphene. Although the band structure is altered drastically in the presence of strongly adsorbed metals, they are still the preferred choice for fabricating contacts on graphene: their strong bonds with graphene are believed to provide a more stable contact. In an attempt to provide strong bonding without altering the graphene electronic structure it was suggested to sandwich graphene layers with metal contacts, creating a double-sided contact which should improve device performance by decreasing the contact resistance [140, 141].

Although DFT simulation results are generally consistent with experimental observations there are discrepancies. These could be attributed to the use of different approximations for the calculations (the local density approximation or the generalized gradient approximation, for instance) and inconsistencies in the choice of variables such as the cut-off energy, the size of the supercells or the vacuum level [118, 142]. The exact doping mechanisms in graphene are still an object of debate. It is thought for instance that the charge transfer between the dopants and the graphene is governed by: i) the work function difference (graphene is p-doped if the work function of the metal is larger than that of graphene and n-doped if the work function of the metal is smaller than that of graphene); ii) the chemical interaction between graphene and the metal [36, 143]. Although initial experimental reports seemed to comply with condition i) [138], K. Pi *et al.* [8] showed experimentally that considering the work function only is not enough to determine the doping type. They found that the Dirac point shifts towards negative gate voltages in the presence of Ti, Fe, and Pt [8]. These transition metals thus act as donors, producing *n-type* doping in graphene as predicted by DFT calculations [124, 125]. However, the work function of Pt (5.9 eV) is higher that of graphene (4.5 eV) and it would therefore be expected to result in *p-type* doping of graphene [143].

One of the most widely used metals in graphene devices as a contact material is Au. The effect of Au on the transport properties of graphene was investigated both experimentally and theoretically [144]. It was found that gold deposition leads to *p-type* doping, which again complies with the work function approach: the work function of Au (4.7eV) is higher than graphene (4.5eV) and therefore Au should acts as an acceptor [124, 138]. However, n-type doping of graphene was observed when the Au deposition is performed at cryogenic temperatures. In these conditions, the carrier mobility appears to decrease which could be explained by scattering from point-like charged impurities.

Charlier *et al.* [145] have investigated the interaction between gold atoms and multiwall carbon nanotubes by combining first-principles calculations with a graphene model and experiments. Their calculations revealed that this interaction was quite weak, allowing Au migration on the graphene surface and the formation of large clusters, whereas when nanotubes have been exposed to an oxygen plasma this leads to the formation of defects (or 'active sites') where gold atoms may have been trapped. These oxygenated vacancies then play the role of nucleation centres for further gold clusters.

An interesting proposal for the Au doping mechanism is suggested by Pinto *et al.* [146] through DFT calculations. They propose that Au does not dope single layers since there is no significant change in the position of the Fermi level in the band structure, but it does dope bi-layer graphene. Shifts in the Fermi level position in the band structure relative to the Dirac point determine the charge transfer direction between the dopant and graphene: using this rule, bi-layer graphene was deemed to be n-type doped by Au. Most theoretical graphene doping studies are carried out on single layers. Mao *et al.* [147] studied bilayer graphene doped with Au: the single Au impurity is placed on top of a carbon atom in the lower layer positioned nearly midway between the two graphene layers in the interlayer direction, in agreement the calculations of Pinto *et al.* [146]. The Au atoms and the bilayer graphene interact with each other and as a result of that interaction the graphene appears to be n-type doped, exhibiting a metallic behaviour [146], when pure bi-layer graphene is semi-metallic.

The doping of graphene has also been experimentally demonstrated for alkaline metals such as K [148] and it was found in this case that the Dirac point shifts to more negative gate voltages with increasing doping amounts, which indicating *n-type* doping. This conclusion was also reached through theoretical calculations, which indicate that the mobility decreases [125].

Finally, it was found that the presence of metals on graphene surfaces, Au, Ag and Pd in particular increases the Raman spectroscopic signal [149-152]. This effect is known as surface-enhanced Raman scattering (SERS) of graphene, with signal enhancements factors as high as 100 times. The enhancement factor appears to change with the number of layers and it is found to be the highest for single-layer and decreases with an increasing number of layers. More tellingly, the Raman peaks appear to change as a function of the doping type, and Raman spectroscopy was thus be used to determine in that Ag leads to n-type and Au is p-type doping [149].

2.5.4 Optimising the Deposition of Metals on Graphene

Its crystallographic quality as well as its thermal and chemical stability make graphene an attractive support material to study nano-sized metal clusters. By reducing their size down to nanometre scale the metal clusters show different electronic, magnetic, chemical and catalytic behaviours than their bulk form. In particular, homogenously-dispersed and equally-sized metal clusters are quite important from applications point of view such as catalysis, plasmonic or electrical transport [153]. The influence of the substrate, the deposition and annealing temperatures, the coverage (the amount of metal being deposited) the stability of the deposited clusters, can all be studied most efficiently *in situ* by STM.

The influence of the graphene growth substrate was recently demonstrated by STM for Au- and Pt- doped graphene grown on Ru [84] and Ir [153] substrates. Different distribution and clustering behaviours were observed for similar amount of Au and Pt, attributed to the strength of the interactions among metal clusters, the graphene and the substrate metals. Similarly, the effect of post-deposition annealing was studied in the case of Au deposited on monolayer graphene with SiC substrate [154]. The deposition of a monolayer of gold on graphene was carried out at room temperature and followed by annealing at 1000K for 5 minutes. The STM investigation was then carried out at liquid nitrogen temperature and revealed the intercalation of gold clusters between the graphene and the substrate, forming Moiré patterns. The metal deposition temperature effect was studied by Sicot *et al.* [155] for Ni clusters on graphene for a Rh substrate. After deposition at 150K, the shape of the nanoclusters was found to be mostly hemispherical. Following a deposition at room temperature, however, the surface morphology was completely different: flat triangular-shaped islands were instead formed on graphene. This suggests that a deposition at higher temperatures does not lead to the formation of ordered arrays. Similar studies were also carried out for Ir clusters on graphene grown on an Ir surface by N'Diaye *et al.* [83]. For metal evaporation below 160 K, the fcc-type regions of the Ir substrate were partly populated, while cluster formation was never observed at all on fcc-type regions for deposition at 350K. In both cases, the hcp-type regions of the substrate were populated. Interestingly, the growth of triangular clusters was observed at a temperature of 550K [83].

The growth of Pt, W, Re, Fe and Au on graphene with an Ir substrate was also studied by the same group. Ir, Pt, W, and Re formed epitaxial cluster superlattices in contrast to Fe, Au and Ni that do not form superlattices [153]. In light of these results, three factors were

considered for selecting metals that are able to grow epitaxial cluster superlattices on graphene on Ir: (i) a large cohesive strength that indicates strong bonding; (ii) a large extension of the localized valence orbital, enabling an interaction with graphene and thus initiating the rehydridization of carbon atoms from sp^2 to sp^3; (iii) a good crystallographic match with the graphene unit cell.

Another extensive study through STM for Pd, Pt, Rh, Co and Au deposition on graphene on Ru was carried out by Zhou *et al.* [84] (room temperature). They show that Pt and Rh form finely dispersed small clusters on graphene on Ru as a result of the strong interaction between metals and rehybridized carbon, whereas Pd and Co form large clusters (3D), albeit with a similar coverage, due to the weak bonding with graphene. The result agrees with earlier observations that both the metal–carbon bond strength and the metal cohesive energies play significant roles. On the other hand, Au clusters were expected to form large 3D clusters on graphene due to the weak interaction between Au and carbon. Contrary to these expectations, Au formed a single layer film on graphene. This intriguing result could be attributed to the very good lattice match between Ru and Au.

Finally, Ag, Au and Al metal nanoparticles were also studied on graphite by means of STM [156]. It was found that single ad-atoms were stable for extended periods of up to a few seconds on graphite, this indication of relatively strong binding being attributed to the presence of defects on the graphite surface.

The substrate can also have a strong effect on the particle inter-atomic spacing, shape, alignment and electronic structure. Investigations of the morphology of gold clusters grown in nanopits on graphite at T= 623K were carried out by using STM by Irawan *et al.* [157]. Pit edges were found to act as condensation centres for gold clusters. Two different morphologies were observed; small clusters showed three dimensional growth and no facets, while with increasing deposition amount the cluster size increased, resulting in flat, thick rafts with hexagonal facets.

Chapter 3

Materials and Techniques

3.1 Graphene Fabrication

Two different techniques were used to produce the graphene membranes for the experiments described in this dissertation: mechanical cleavage of highly ordered pyrolytic graphite (HOPG) and chemical vapour deposition growth on metallic substrates (copper and nickel). Mechanically-cleaved graphene was only used for initial investigations, CVD-grown graphene was used otherwise.

3.1.1 Mechanical Cleavage (exfoliation)

Obtaining graphene by exfoliation or mechanical cleavage is simply done by pressing a piece of HOPG against some adhesive tape and peeling the tape off. Due to the layered structure of graphite and the weak interlayer bonding (the layers are held together by Van der Waals interaction), the graphite layers are easily separated, so that after repeating the peeling process a few times extremely thin layers are left on the tape. The thin graphite flakes obtained in this fashion are then transferred onto an oxidised silicon substrate. Although the thickness of the oxidised layer on top of the Si can be chosen to be between 90 and 315 nm, this coating is important as it provides good contrast for a quick identification of the graphene layers under an optical microscope [88]. The surface of the substrate is cleaned prior to exfoliation to minimize contamination and to enhance the adhesion of the graphene flakes. The cleaning consists of two steps: chemical solvent cleaning is carried out first with successive 10 mins ultrasonic baths in acetone, deionized water (DI-water) and isopropanol (IPA), followed by oxygen plasma cleaning (20 mtorr) for 10 mins. Once the substrate has been cleaned the tape is gently pressed onto it and then either simply peeled off or removed using a chemical treatment. After the tape removal, the substrate (on which thin graphite layers are now adhering) is cleaned further with solvents (acetone and IPA) to eliminate any contamination from the etchant and the adhesive tape. The sample is then baked at a temperature of 120^{o}C for 15 mins. Finally, a piece of fresh adhesive tape is applied to the substrate to peel off the thickest graphite layers and leave predominantly single layer graphene on the Si/SiO_2. These steps for the fabrication of graphene flake by exfoliation technique are summarized in Figure 3.1.

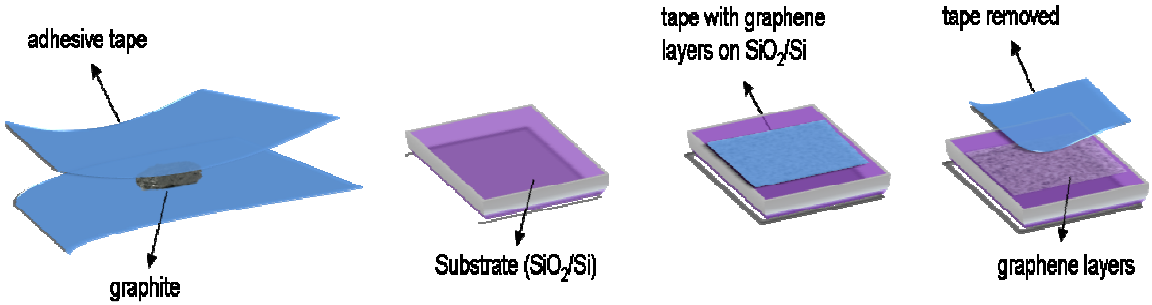

Figure 3.1 Step by step graphene fabrication by exfoliation of graphite on a substrate.

The obtained graphite layers are initially observed under the optical microscope to identify single layer regions, whose specific colour and contrast against the oxidised silicon wafer background provide a quick and convenient screening criterion. An optical micrograph of exfoliated graphene layers on 290 nm-thick oxidised silicon substrate is presented in Figure 3.2. The flakes on the wafer vary in thicknesses from single layer to much thicker regions: a single layer area, 100x100μm in size, is magnified. This size of the single layer graphene flake is adequate not only for electron microscopy but also for many other characterization techniques.

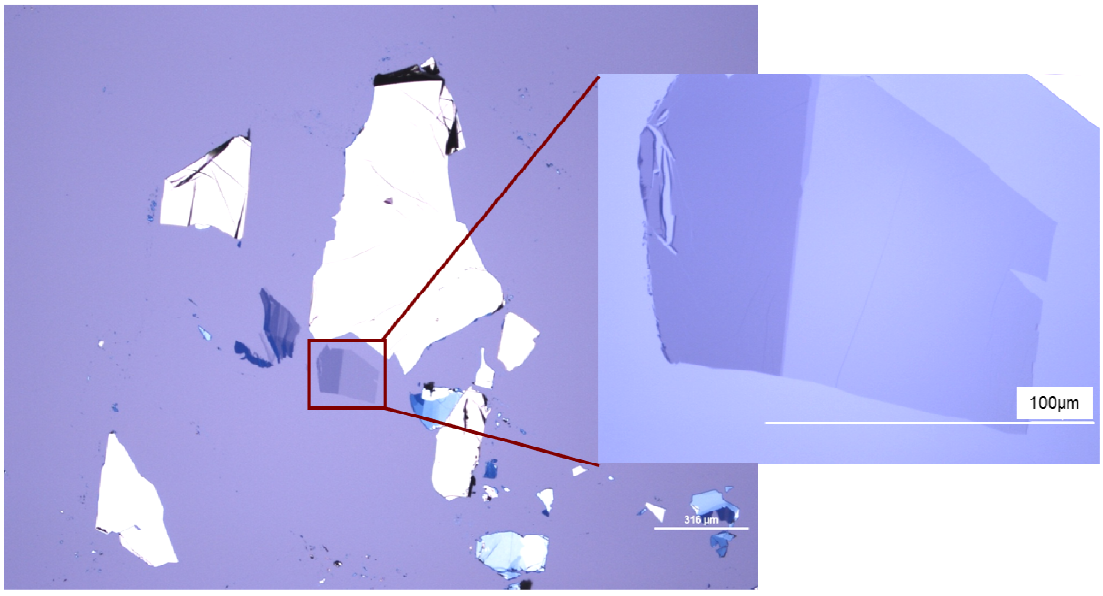

Figure 3.2 Optical image of the exfoliated graphene layers on 290 nm thick oxidized silicon wafers and enlarged view of single layer region is shown as inset.

3.1.2 Chemical Vapour Deposition

Graphene grown by chemical vapour deposition on Ni substrates was initially procured from external sources while the techniques necessary for local production on Cu substrates were being perfected. It was indeed found that graphene grown on Ni usually presents a large proportion of many-layer areas, with only very few single-layer regions. As explained in Chapter 2, this is due to the high solubility of carbon in Ni, making any control of the grown graphene thickness difficult [77]. By contrast, using copper for which the carbon solubility is low, enables a better control on the number of layers [79].

For our purposes, a 25 mm-thick Cu foil is loaded in a 4 inch quartz tube and heated up to 1000^{o}C, maintaining a 20 cubic centimetres per minute (sccm) H_2 gas flow at a pressure of 200 mTorr. The Cu foils were annealed in these conditions for 30 mins. This process is designed to reduce any oxidized layer on the foil surface, but also to extend the grown graphene grain size by coarsening the Cu grains. The precursor gas for the graphene growth is a mixture of H_2 and CH_4 with flow rates of 20 and 40 sccm, respectively: it is injected into the CVD chamber while maintaining the reactor pressure at 600 mTorr for a 30 mins period known as the growth time. This provides the right amount of time for carbon atoms to be adsorbed onto the Cu surface, act as nucleating sites for the single layer graphene which proceeds by grain propagation [78, 79]. After the growth period, the sample is cooled rapidly to room temperature under a hydrogen atmosphere at a pressure of 200 mTorr. A schematic representation of the graphene growth process is shown in Figure 3.3. The quality and number of layers of the grown samples was systematically assessed by Raman spectroscopy. The Raman spectra of graphene grown on Cu does not show any D peak, indicating the absence of any structural defect, while the 2D peak is a single sharp Lorentzian, which is the signature of single layer graphene [89].

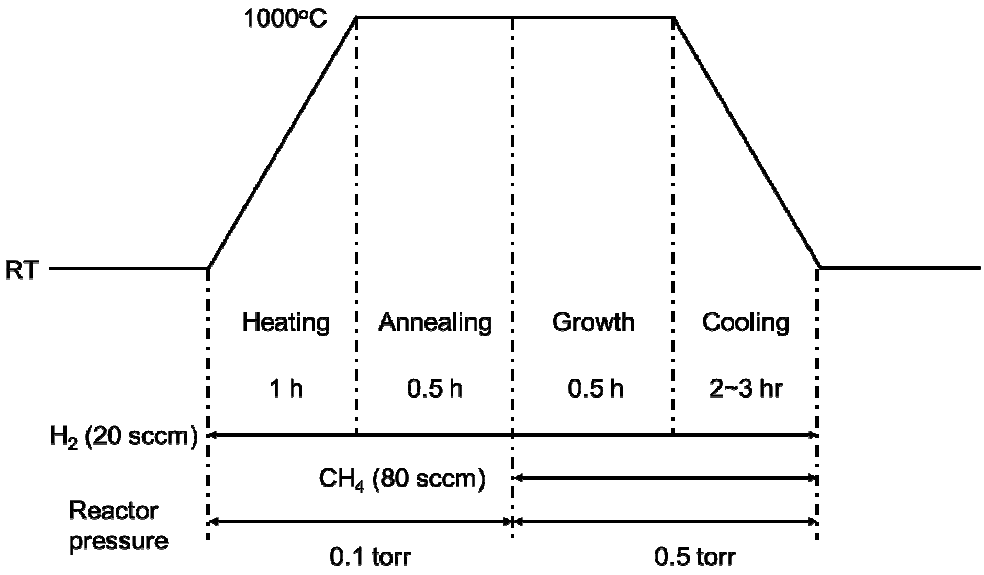

Figure 3.3 Sketch of the graphene growth process on a copper surface, showing gas flow rates, growth temperature and time.

3.1.3 Fabrication of Suspended Graphene Sample for Microscopy

A so-called *wet transfer* technique was used to prepare suspended samples for the microscopy experiments from both exfoliated and CVD-grown graphene flakes, with only small variation in the methodology depending on how the graphene was initially grown. Although more common in device fabrication and in particular for graphene heterostructures, a *dry transfer* technique case also can be used to prepare TEM samples. The main difference between these two techniques lies in the use of polymers and chemicals.

In the case of exfoliated graphene samples and after the initial identification of regions of interest on the oxidised silicon wafer under an optical microscope, a layer of ~300 nm of poly-methyl-methacrylate (PMMA) was 'spun' onto the graphene flakes using a spinner (typically 1 min at 3000 rpm), followed by a 130^{o}C bake of the samples for 5mins. This additional layer is designed to protect the underlying graphene layers, providing mechanical support and facilitating the handling of the flakes during the transfer procedure. The substrate, or more precisely the oxidised silicon topmost layer, is then etched away using a 3% potassium hydroxide (KOH) solution, detaching the PMMA and graphene flakes from the silicon wafer. Once almost detached, the wafers are dipped into DI-water, to fully detach the PMMA and graphene flakes and to rid them of chemical residues from the etcher and of any possible contamination from the silicon wafer. Rinsing

in DI water is repeated to ensure the best sample cleanliness. Once the graphene flakes are transferred onto TEM grid by simply 'fishing them out' of the DI water bath, the sample is dried at 50^{o}C for 10 mins, followed by a further 120^{o}C bake for 10 mins in clean room conditions to improve the adhesion of the flakes on the grid, get rid of any remaining water content, and importantly, to flatten out (anneal) any possible wrinkles, which may have been created during the transfer. Finally, the PMMA protective layer is dissolved by dipping the sample into acetone for 15 mins. The final samples are dried in a Critical Point Dryer (CPD) in order to protect the delicate, now suspended, graphene layers against any rupture, damage or deformation due to surface tension. At its critical point of temperature and pressure, a compound can indeed exist in liquid and vapour phase at the same density. The surface tension is therefore zero at the interface between the liquid and the gas. A CO_2 medium was used here for drying due to its low critical temperature of only 31°C and pressure 7.39 MPa (compared to 374°C and 22.064 MPa for water). The transfer process to TEM grid is schematically summarised in Figure 3.4.

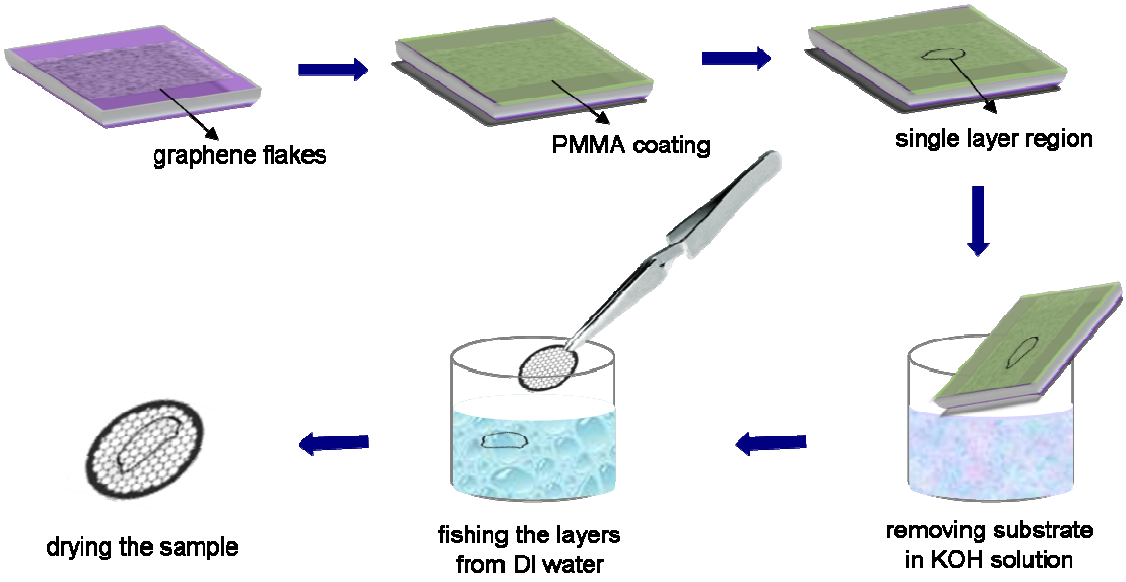

Figure 3.4 Schematic representation of the transfer of exfoliated graphene layers from an oxidized silicon wafer to a TEM grid by wet-etching using a KOH solution.

Optical images of graphene flakes on the substrate and after the transfer on the grid are shown in Figure 3.5a-c, along with low magnification TEM and STEM images in Figure 3.5d-f.

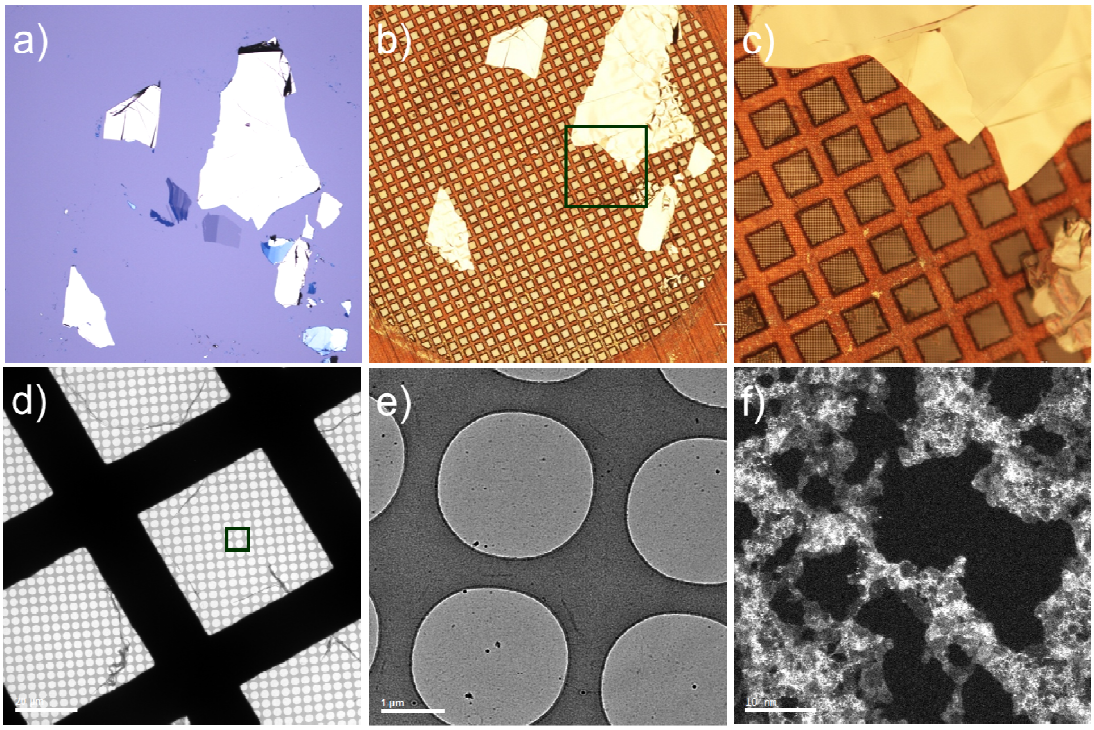

Figure 3.5 Graphene flakes a) as prepared on an oxidized silicon wafer, b) after transfer onto a TEM grid; c) magnified optical image of the green square indicated in (b) illustrating how suspended single layer regions are not easily visible; d) low magnification TEM image of a single layer area. Broken flakes and rolled up regions produce some visible contrast and hint at the presence of the single layer graphene sheet; e) enlarged view of the green square shown in (d); f) overview HAADF STEM image of a single layer graphene flake, with clean graphene areas (dark patches) surrounded by hydrocarbon contamination (brighter, heavier patches).

In the case of graphene obtained by CVD on either Ni or Cu, the graphene growth takes place on both sides of the metal substrate. An additional step is therefore necessary to remove the flakes present on one of the two sides. The side being prepared for transfer is covered with PMMA, in order to protect the underlying graphene and to ease the transfer process as was the case with exfoliated samples, while the other side is exposed to 20 mTorr of oxygen plasma for a few minutes.

An aqueous iron chloride ($FeCl_3$) solution is commonly used as an etchant to remove the nickel or copper foil, through a slow redox reaction. Depending on the concentration of the etchant it can take from one to a few hours to separate the graphene film from the substrate, at which point the PMMA and graphene layers are found floating at the surface of the solution. However, using $FeCl_3$ leads to really high concentrations of surface

contaminants on the graphene, as revealed by post-transfer X-ray spectrometry (EDX) measurements. To minimize this effect, a 0.1 mol ammonium persulphate ($(NH_4)_2\ S_2O_8$) solution was favoured as an etchant to produce the material investigated here, resulting in much cleaner graphene surfaces than when using $FeCl_3$. After the etching procedure, the PMMA/graphene layers are repeatedly rinsed in DI water, to remove further possible contaminants. The flakes are again directly transferred onto TEM grids by 'fishing them out' of the DI water bath. As for the exfoliated graphene transfer procedure previously described, the grids are then baked, the PMMA layers are dissolved in acetone and finally dried in a CPD.

3.2 Metal Deposition

Thermal and electron-beam evaporators were used to deposit metal impurities onto the suspended graphene membranes. Both techniques are based on heating the target metal sufficiently by either applying current or e-beam that leads to vaporisation of the metal. The evaporation rates were varied from 0.1 nm/s to 1 nm/s, as were the overall deposited thicknesses, which ranged from 0.1 nm to 3 nm. None of the deposition parameters led to a full coverage of the graphene membrane by the deposited metals. Instead, clusters of varying sizes were formed (depending in particular on the metal being deposited). Decreasing the deposition thickness is allowed nevertheless to control the amounts of impurities present on the flakes, with a view initially to study the interaction of individual atoms with the graphene structure.

Metal deposition can be affected by many factors: the substrate on which the graphene is placed, the evaporation rate and most importantly the vacuum levels and temperature during the evaporation. The latter have indeed been shown to have a strong influence on the behaviour of metal atoms on the graphene surface, resulting in different surface morphologies and transport properties [144, 155].

Two distrinct strategies were adopted here. Firstly, the amount of metal deposited was varied, keeping all other parameters constant. Au was chosen as a test case for this series of experiments. Secondly, a fixed amount of material was deposited in fixed conditions for a large variety of metallic species, allowing a thorough comparison between metals, of the distibution, size and shape of the clusters. A total amount of 0.2 nm of Fe, Cr, Ti, Ni, Pd and Au was thus evaporated onto different graphene TEM grids at a rate of 0.1 nm/s, in

vacuum better than 10^{-6} mbar (up to ~10^{-8} mbar). A schematic representation of the electron-beam evaporation chamber is shown in Figure 3.6.

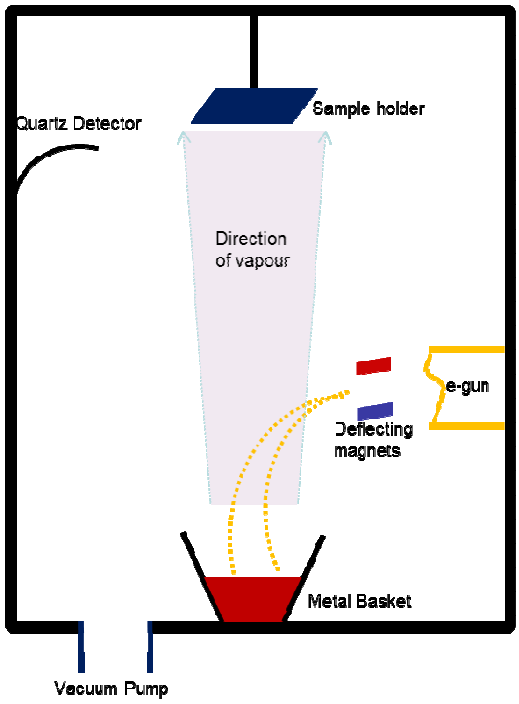

Figure 3.6 Schematic of the electron beam evaporator.

3.3 Basics of (S)TEM

3.3.1 Electron-Matter Interactions

Electron microscopy is based on the interactions of matter with a high energy beam of electrons (from a few keV to a few MeV). These interactions provide insights about the structure, topology, morphology and composition of a material. The main interactions between an incident beam of electrons and a specimen are schematically shown in Figure 3.7. When a beam of high energy electrons hits a specimen, the electrons penetrate into specimen and as a result of the electrostatic attraction between the electrons and the nucleus of the atoms present in the material, their path is deflected towards the atomic cores. Electrons travelling closest to the nuclei are scattered to higher angle, due to a larger Coulomb force. Scattering to high angles is stronger for heavier atoms, with a higher atomic mass Z, than for lighter ones: this property is the main mechanism used for HAADF imaging, which is also often called ‘Z-contrast’ imaging [158, 159].

The interactions of an electron beam with matter can be divided into two categories: *elastic* and *inelastic*. In the case of elastic interaction, the incident electrons do not lose any energy to the sample. If some energy transfer occurs between the incident beam and the sample, the interaction is called inelastic. Electron energy loss, X-ray, Auger or cathodoluminescence spectroscopy signals, or even secondary electron imaging, all exploit these inelastic interactions to provide structural and chemical information about the sample. These techniques are often collectively referred to as analytical electron microscopy [158]. The signals generated via *elastic* and *inelastic* interactions are used in the TEM and STEM to obtain structural and compositional information about the specimen.

Waves in electrons beam can be either coherent or incoherent. If waves have the same wavelength and are in phase with each other, they are called coherent, whereas if the beam constitute of waves with different wavelengths or have phase difference, they are called incoherent. Additionally, when two waves interfere (superposition) can result in *constructive interference* (maxima and minima of waves coincide) or *destructive interference* (maxima of one coincide with other's minima).

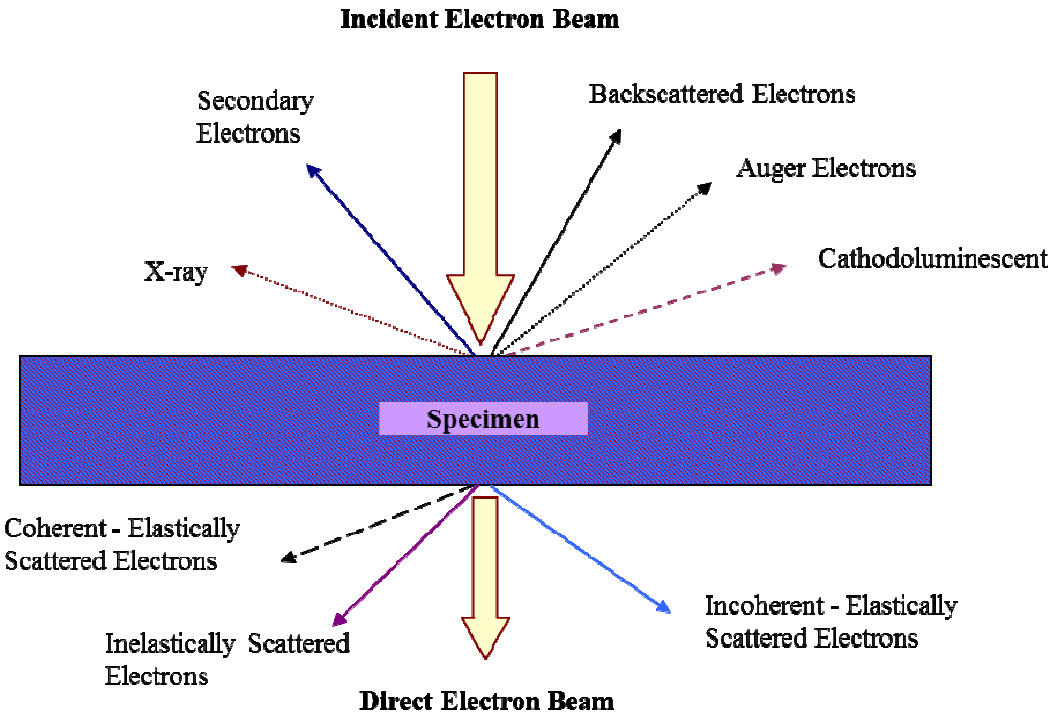

Figure 3.7 Basic interactions between an electron beam and a specimen.

TEM consists of several major components: its illumination system, comprising an electron source (or gun) and one or more condenser lenses; its image forming system, comprising at least an objective lens; a projector system, including one or more projector lenses and apertures. A basic ray diagram of the TEM is shown in Fig. 3.8a.

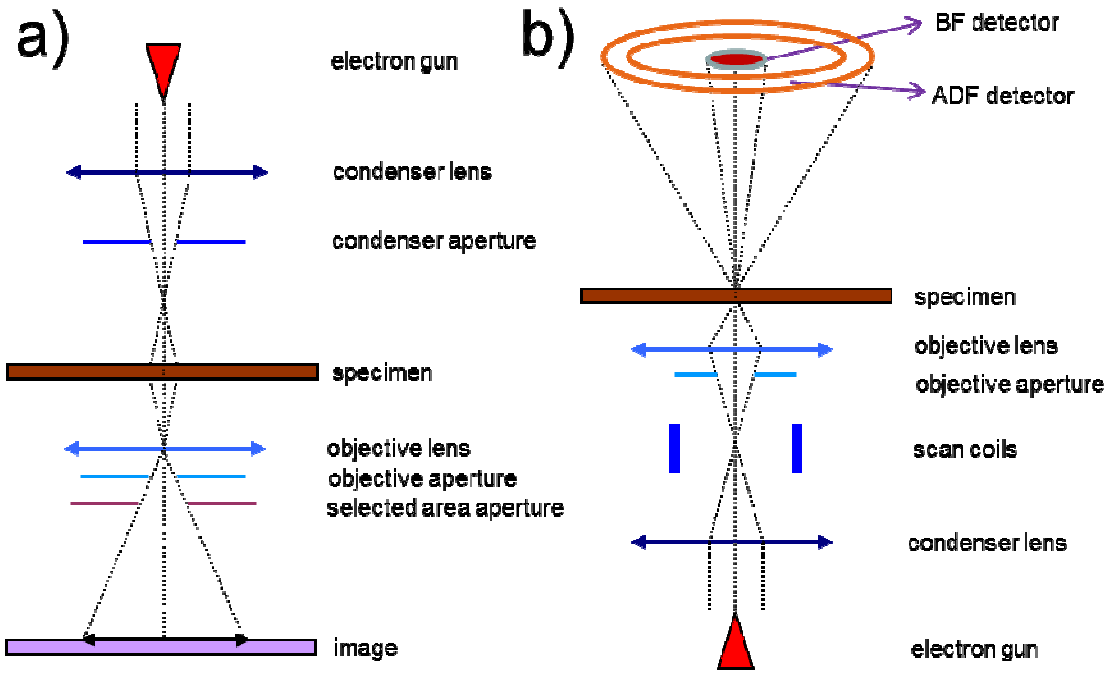

Figure 3.8 Schematic of a) conventional TEM and b) dedicated STEM

3.3.2 Bright Field and Dark Field Imaging in TEM

In the bright field (BF) imaging mode of a TEM only the direct unscattered electrons and small-angle scattered electrons are allowed to contribute to the image formation. This is achieved by inserting a small objective aperture into the back focal plane of the objective lens in the TEM, thus allowing only the direct beam to pass through it whilst blocking scattered beams of electrons. If a scattered beam of electrons is instead selected to form the images, a so-called dark-field (DF) image is formed.

The most important parameter for TEM imaging is contrast generation which is by definition the differences in intensity between two adjacent areas. Although there are few different contrast mechanism in TEM imaging, phase contrast is the main contrast mechanism in BF imaging and basis for the so called high-resolution TEM (HRTEM). Phase contrast occurs due to the difference in the phase of the electron waves produced by interaction with the thin specimen. By careful choice of defocus these phase changes can be converted into contrast which is observable in the image and the appearance of lattice

fringes [158]. Although the lattice fringes are not direct images of the atomic structure of the crystal but can give information about the sample, such as the lattice spacing. Phase contrast is present in every TEM micrograph because almost all electron scattering leads to a phase change of the electron wave. Phase contrast images are sensitive to many factors including acceleration voltage (wavelength), size of the apertures and aberrations (spherical aberration, astigmatism and focus) [158]. The phase shift produced by these effects can be described by a complex contrast transfer function (CTF) which oscillates as a function of spatial frequency. When the phase contrast is positive atoms appear dark against a bright background. When phase contrast is negative atoms appear bright against a dark background. When CTF = 0, no detailed information can be obtained in the image [158].

3.3.3 Scanning Transmission Electron Microscope

As a result of the reciprocity principle, a dedicated STEM is most easily described by a TEM system for which the direction of electron beam would be reversed. Condenser lenses demagnify the source, which is then focused by the objective lens to form a small probe at the specimen. This convergent electron beam is scanned over the specimen by deflection coils [160]. Detectors placed after the sample collect the transmitted or scattered electrons to build up images serially. Both BF and HAADF images can be acquired simultaneously in a STEM. A schematic representation of dedicated STEM is shown in Figure 3.8b.

In order to achieve atomic resolution in STEM a very fine electron probe is required. Thanks to the development of aberration correctors for the electromagnetic lenses used in electron microscopes, probes of diameter below ~1Å can now be routinely achieved, even at lower acceleration voltages such as 60 kV [15, 161]. The STEM probe shape (thus image resolution) is determined by the interference of electron wave components that have passed through opposite sides of the illumination aperture, whereas the resolution of the usual TEM BF images is determined by the interference between the unscattered electron beam in the centre of the TEM objective aperture and the scattered waves near the edges of the aperture [162].

In the STEM, images are obtained serially from a very large number of image points in a reasonably long time (for high signal/noise ratio), whereas in a TEM image recording is parallel (simultaneous for all image points) and thus usually much shorter. Annular Dark

Field (ADF) images can be obtained with much greater efficiency in a STEM than in a conventional TEM, however, by placing an annular detector after the sample to collect electrons scattered to high angles (the unscattered electrons are not used). The inner angle of the detector should be made large enough to be able to eliminate Bragg reflections (diffraction contrast) in the image that make image interpretation difficult [158]. Although the spatial resolution of STEM and TEM is comparable, due to its scanning nature a STEM usually has a poorer temporal resolution, which may limit real time dynamic/kinetic studies.

3.3.4 Annular Dark Field Imaging (Z-contrast)

One of the most important characteristics of ADF imaging is using incoherent image formation process in contrast to BF imaging which relies on mostly on phase constrast and therefore interference phenomena. STEM ADF signal is predominantly produced by electrons that have been scattered by the atomic nucleus (Rutherford scattering). This makes the ADF intensity of individual atoms depend on the charge of the atom's nucleus. Different Z atoms therefore give different ADF image intensities and this imaging technique was called Z-contrast by Albert V. Crewe as he was the first to demonstrate it [163, 164].

The localization of the ADF signal is much better than the localization of the signals used by TEM BF because the atomic nucleus is much smaller than the projected potential that imaged by TEM, and also smaller than the valence electron distribution imaged by STM [162]. When STEM ADF imaging uses only sufficiently high angles, it becomes largely incoherent. This imaging (collecting very high angle, incoherently scattered electrons) is also often called HAADF imaging as the intensity recorded in this mode by positioning the electron beam on an atomic site is approximately proportional to the square of the average atomic number Z of this site [162, 165, 166]. Incoherent images have the great advantage that they either show the correct contrast or no contrast at all, the images typically fade out with increasing defocus without changing character (no contrast reversal). This makes them straightforward to interpret and therefore often much easier than that of BF phase contrast images which their contrast reversible with the focusing settings. The HAADF-STEM imaging mode is particularly useful to visualise the structure and defects of materials, as its chemical sensitivity provides a direct visual guide to identify directly ad-atoms and impurities of a different weight than the surrounding

material [15, 96]. Sample drift may however affect the image quality as long recording times may be necessary for high signal/noise ratio images.

3.3.5 Filtering and Probe Deconvolution

Raw (unprocessed) ADF images suffer from statistical (shot) noise and electron probe tail. The shot-noise is due to the small signal per pixel for each atom in the image and is easy to smooth out by filtering out spatial frequencies higher than those containing the useful information. However, probe tailing is slightly complicated. Due to aberrations the electron probe has a relatively narrow central maximum and an extended tail. The tail spread from each atom contributes to the signal its neighbours (including the hole side) in particular for materials with narrow spacing. For example, in the case of graphene the tail contributes around 10% of each carbon atom's peak intensity to the centres of the carbon hexagons [15]. To be able to accurately compare atomic intensities and thus interpret irregular features in the sample the tail contribution should be removed. For this purpose, a filter that consisted of two Gaussians can be applied, a positive one which is relatively wide and which gradually cuts off spatial frequencies beyond those actually transferred by the microscope (smoothing) and a negative one which is narrower and which essentially adds a weak and spread-out negative skirt to the image of every atom [15, 161, 162].

Another way of removing the noise and the probe tail is using maximum entropy method. The procedures do not perform a direct deconvolution, but estimate a predicted image by convoluting it with the probe function [167]. These filtering procedures were applied to some of the graphene HAADF images presented in the thesis. As a result of the filtering the noise and removing the tail contribution from the graphene images, the intensity at the centre of the graphene hexagons (hole) went to zero (vacuum value). This enabled identification of foreign ad-atoms e.g., oxygen and silicon in the graphene lattice via comparing intensity profiles.

3.3.6 Electron Energy Loss Spectroscopy

As described above, as a result of inelastic interactions between the incident beam and the specimen, the scattered electrons can lose a part of their energy. This loss of energy can be measured by a spectrometer to yield elemental, chemical and dielectric information about the specimen [168]. EELS is an absorption spectroscopy however, energy dispersive X-ray spectroscopy (EDXS) is an emission spectroscopy which monitors the energy or

wavelength of the emitted X-rays produced as a result of the interaction of the incident electron with the sample [169]. Contrary to EELS, the EDXS only provides elemental information. EELS has high detection efficiency for elements with low Z, where the excitation edges tend to be sharp, well-defined, and at experimentally accessible energy losses, whereas higher Z elements are more efficiently studied using EDXS because relaxation of excited atoms by emission of X-ray becomes more efficient for heavier atoms (Z>30) and also EDXS has a considerably higher spectral range than EELS [158]. Furthermore, electrons can be collected by an EEL spectrometer with almost 100% efficiency, however, because X-rays cannot be deflected into an appropriate detector their collection will always be insufficient (usually less than 1%). Additionally, EELS detectors have a much higher energy resolution than EDX detectors, so that the absorption peak fine structure can be recorded with greater detail and analysed to give information about the bonding state and electronic band structure of materials, for instance [168]. An EEL spectrum is typically divided into three energy loss regions, as shown in Figure 3.9.

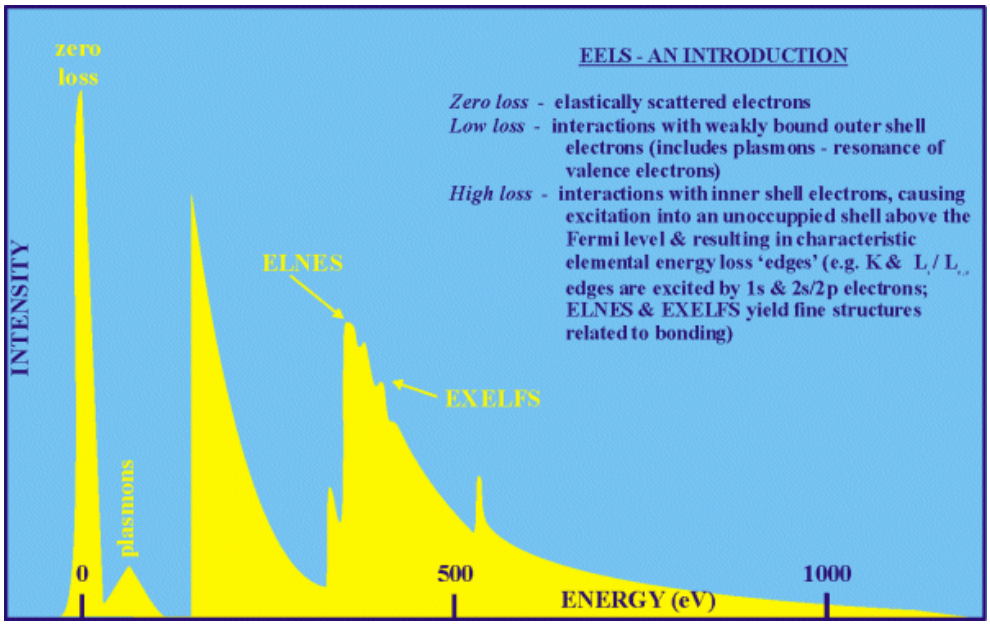

Figure 3.9 EEL spectrum with the three different energy loss regions. (http://www.see.leeds.ac.uk/see-research/igt/people/lloyd/eels.htm)

1. Zero loss peak (ZLP). This peak contains all the electrons that have passed through the specimen without any interaction or with an elastic, loss-less, interaction: as its name suggests, the zero loss peak is found at 0 eV energy loss in an EEL spectrum. If the sample is sufficiently thin, the ZLP is the most intense part of the spectrum.

2. Low loss region. This region typically includes energy losses between the ZLP and about 100 eV. The inelastic scattering of incident electrons by the outer-shell electrons of the sample's constituting atoms leads to the excitation (or promotion) of valance band electrons to the conduction band. Plasmon oscillations, which are collective excitations of free electron density, or inter- or intra- band transitions are also observed in the low loss regions typically <50 eV. The intensity of these most prominent peaks provides information about the sample thickness: as a rule-of-thumb, the more intense the plasmon peaks are (compared to the ZLP), the thicker sample is.

3. High (core) loss region. Energy losses in this region of the spectrum occur as a result of the interaction between the incoming electrons and the material's inner-shell electrons, which are strongly bound. When sufficient energy is transferred to the inner-shell electrons they are ejected from the atom, resulting in an ionized atom. As the ionisation energy is a characteristic of each element of the periodic table, edges observed in the core-loss region contains information about the chemistry of the specimen. In addition to containing quantitative elemental information, ionisations edge often have small intensity fluctuations above their onset. These features, called the energy-loss near-edge structure (ELNES) are sensitive to the local atomic environment of the ionised atoms, such as its coordination, valence and the type of bonding [168].

3.3.7 Aberration Corrections

In a perfect lens, all incident rays cross the optic axis at the same Gaussian focal point, thus enabling a true representation of the source image. In practice however, there is no such thing as a perfect lens: all round electromagnetic lenses suffer from optical aberrations. These are many types of aberrations including spherical aberration, astigmatism, coma, field curvature, which are geometric (monochromatic) aberrations, and there are also chromatic aberrations [170]. The first three are the most important aberrations and in an uncorrected instrument the main limiting aberration is known as spherical aberration (C_s). This results in image blurring as rays travelling at high angle to the lens optic axis are focussed more strongly than rays travelling close to the axis [171]. In brief, spherical aberration can be corrected through the addition of extra lenses in the microscope column. This is achieved using multipole lenses, such as dipole, quadrupole, hexapole and octupole [172]. The most important difference between multipole lenses and round lenses is that in the former the field lines are mostly perpendicular to the beam while in the latter they are largely parallel to the beam. These additional lenses are carefully

aligned to produce negative spherical aberration to compensate exactly the always positive aberration of the pre- or post- specimen round lenses. When pre-specimen lenses are corrected, the microscope is said to be probe-corrected. This configuration is employed for STEM-HAADF mode. When post-specimen lenses are corrected, the microscope is said to be image-corrected. This configuration is employed for HRTEM mode, in particular.

Astigmatism occurs when the lens is more powerful in one plane than in the plane normal to it that results in displacing the cross-over of the off-axis rays along the optical axis. The astigmatism can be controlled in the condenser and the objective lenses. Coma (comatic aberrations) is related primarily to rays which are emitted from an object point slightly off the optic axis. All the rays which travel through the centre of the lens will still be brought to a point focus off the optic axis but rays which travel through peripheral field of the lens will be focussed at different points.

Chromatic aberration can also cause image distortions. Optical lenses with chromatic aberrations have different refractive index for different wavelengths of the incident rays. For an electron lens, chromatic aberration effects will therefore result from any non-zero energy spread (or fluctuations in the gun accelerating voltage). The presence of chromatic aberration results again in image blurring as electrons of different energies are focussed at different focal points. Chromatic aberration has become the limiting aberration in particular for operation at low accelerating voltage.

The effect of geometric aberrations is easily assessed by a visual inspection of the shadow (projection) image of the sample called the electron Ronchigram [172]. Only the centre of the Ronchigram image, the so called “sweet spot” transfers the spatial information of the sample. Parts outside the featureless Ronchigram need to be cut out by the objective aperture. Automated aberration-tuning algorithms typically are used to measure the aberrations. In one automated tuning approach, after an initial Ronchigram is acquired, the probe is moved by calibrated (small) amounts in orthogonal (x and y) directions. At each probe position, a new Ronchigram is acquired. However, the observed shift in the Ronchigram is not uniform and therefore it is necessary to measure the distances at several observable points (or patches) in the Ronchigram (using cross-correlation). This data can then be used to determine the aberration coefficients [171, 172]. The effect of chromatic aberration is not easily assessed from a regular Ronchigram and is not corrected for any of the data in this thesis. When chromatic aberration is the dominant limit the resolution needs to be computed from the values of the two parameters that determine the magnitude of the aberration: the chromatic aberration coefficient Cc and the

energy spread of the electron beam δE. Cc can be measured simply by changing the high voltage and measuring the change in defocus. δE can be measured if an electron energy-loss spectrometer is a part of the STEM system.

3.3.8 Beam Effects

The electron beam might modify the structure of a material it interacts with, thus limiting the information that can be collected. For example, if an incoming electron transfers enough energy to an atom in the lattice to eject it from the lattice, point defects are formed and the sample is no longer representative of its pristine state. This process is known as knock-on damage. Another potentially nefarious effect of the electron beam is ionization damage, whereby the bonds between atoms are broken eventually resulting in damage to the specimen. Ionization damage is also known as radiolysis: so-called 'soft' materials such as polymers are typically sensitive to ionization damage.

Heat-sensitive materials might be damaged by the beam: energy from the incident electron beam is absorbed by the sample through the creation of phonons for instance. As a result, the material could become amorphous or even melt, with obvious disruptive consequences for the analysis. Phonons can also cause drift by heating the specimen [158].

Finally, incident electrons may become trapped within the sample which then becomes negatively charged. Although this charging effect is not an issue for conductive materials as the charge can be transmitted away, it is problematic for non-conductive surfaces because: the charge remains local and causes vibrations and drift that can prevent the investigation [173].

3.3.9 Instruments for Electron Microscopy

Tecnai

Initial experimental data to identify graphene layers and some of the high resolution data on the metal-graphene system were obtained on an FEI Tecnai F30 microscope operated at 300 kV. A photograph of this instrument is shown in Figure 3.6a. This high acceleration voltage is much higher than the knock-on threshold of carbon in graphitic structures, which therefore greatly restricts its use for graphene studies. The Tecnai is equipped with Schottky electron source, an EEL spectrometer and an EDX detector, enabling high resolution chemical analysis of the specimen.

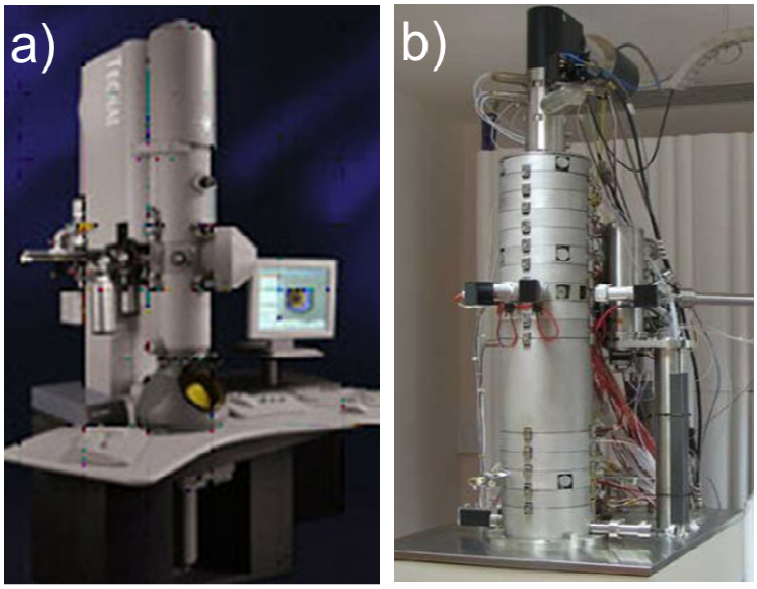

Figure 3.10 Photographs of a) FEI-Tecnai F30 and b) Nion UltraSTEM 100

SuperSTEM

Most of the experimental data were acquired at the SuperSTEM Laboratory on an aberration corrected (up to 5th order) Nion UltraSTEM dedicated STEM. It is equipped with a cold field emission gun with an energy spread of 0.35 eV and operated at 60 kV to prevent knock-on damage to the graphene samples. This instrument is shown in Figure 3.6b. The UltraSTEM microscope has a UHV design throughout, allowing pressures at the sample of below 5x10^{-9} torr for contamination-free observation [15]. The estimated probe size (full width at half-maximum) is about 1.2 Å for the typical operating conditions for graphene investigations at 60 kV acceleration voltage and 30 mrad probe convergence semi-angle. Detectors with different geometries are used to collect electrons scattered to different angular ranges. For example, the BF detector used to obtain phase contrast images can collect electrons scattered up to 6 mrad. The so-called medium angle annular dark field (MAADF) detector collects electrons scattered from 45 to 190 mrad (provide relatively high contrast and signal level) and the HAADF detector used to record the Z-contrast images has inner and outer radii of 70 mrad and 210 mrad, respectively (diffraction contrast almost suppressed). The instrument is equipped with a Gatan Enfina EEL spectrometer and its acceptance semi-angle was calibrated at 35 mrad for core-loss spectroscopy.

3.4 Scanning Probe Microscopy

Scanning probe techniques such as STM and AFM are ideal to obtain information about the surface morphology and the electronic structure of a sample. Combining microscopy and spectroscopy (STS) capabilities makes scanning tunneling microscopy in particular a very powerful tool in surface science. STM has been widely used to investigate carbon-based materials such as graphite, carbon nano tubes and more recently graphene [174]. An overview and atomic resolution STM images of HOPG are shown in Figure 3.11a-b. Due to its Bernal stacking the graphite shows a triangular symmetry rather than the hexagonal symmetry asscociated with the graphene structure, as is clearly observed in fig. 3.11b. The three carbon atoms of the top layer that lead to the triangular symmetry are located above holes (centre of the honeycomb hexagons) of the bottom layer. The other three atoms, which are located on top of three underlying carbon atoms in the bottom layer, cannot not be imaged due to the atomic interactions between the top and bottom. On the other hand, the honeycomb lattice structure of graphite can be observed by increasing the bias voltage, causing a decoupling of the two topmost layer as result of strong tip-sample interaction (electrostatic attraction) [175, 176]. This is shown for instance in fig. 3.11c. It was recently demonstrated that graphitic layers can be detached from bulk graphite in a controllable way, using so-called 'electrostatic manipulation STM' [177]. The appearance and electrical properties of graphitic flakes obtained in this fashion were shown to be distinct from those of bulk graphite [176].

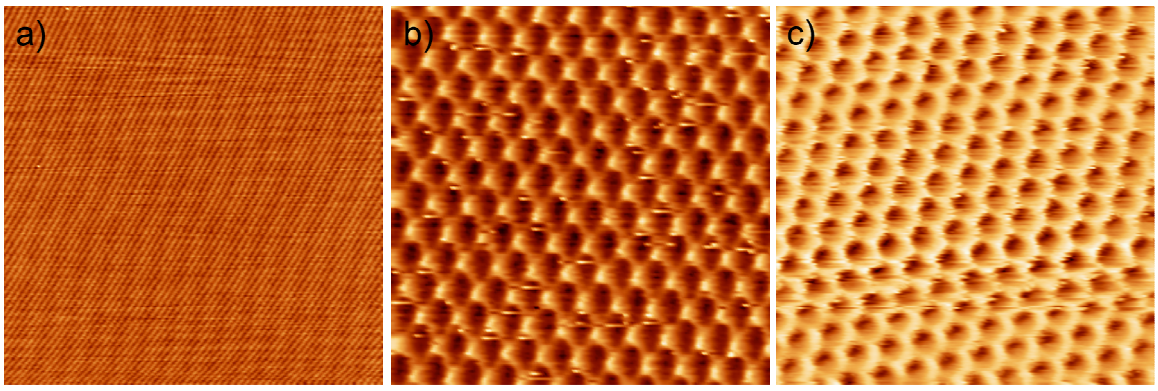

Figure 3.11 STM images of graphite: a) overview (50 nm frame); b) atomically-resolved triangular periodicity (3 nm frame); c) atomically-resolved hexagonal periodicity (3 nm frame) obtained by decoupling the topmost layer from the underlying bulk.

3.4.1 Scanning Tunneling Microscopy

In the STM, a sharp metallic tip, ideally terminated in a single atom, is scanned a few angstroms above the sample surface using a piezoelectric motor. The principle of STM relies on the tunneling effect. When applying a voltage bias between the tip and the sample, electrons can overcome the potential barrier and create a tunnelling current. Variations in this current are used to generate atomic resolution images (it is in fact the local density of the states of the surface of the sample that is being imaged). Spatial resolutions of 1 Å can be achieved in the STM, depending on the tip sharpness and the distance between the tip and sample (changes in this distance as small as 1 Å can cause an order of magnitude variation in the tunnelling current). The tip must be sharp in order to achieve atomic resolution and accurate spectroscopic data: a blunt tip or the presence of more than one fine point may lead to inaccurate interpretation of the STM data. As for STEM, the scanning nature of STM limits its temporal resolution.

Depending on the biasing conditions, that is whether the tip is kept at a positive or negative potential relative to the sample, electrons can tunnel from the tip to the sample (tip at a lower potential), or from the sample to the tip (tip at a higher potential). This requires that the investigated surface should be either conductive or semiconductive: imaging the surfaces of insulators is almost impossible in STM but can be achieved by AFM [174, 178].

The STM probe is scanned laterally in the *x*- and *y*- directions using the piezomotors while the height *z* of the tip above the surface is adjusted by a feedback mechanism to keep the tunnelling current constant on a scanned area in the STM. This imaging technique is also known as constant current imaging or *z*-imaging and provides topographic information about the sample surface. Impurities, ripples or even grain boundaries are thus readily observed by monitoring the relative height change of the surface. Furthermore, the electronic feedback mechanism is indispensible to avoid crashing the extremely fragile tip into the sample.

Gain parameters can be adjusted to tailor the tip response to changes on the sample surface to avoid possible tip and specimen damage. For example, a low gain is more suitable for flat surfaces where no quick response is needed. In these conditions, the tip height can remain almost fixed. In the case of a rough surface, a high gain feedback is required to allow the the tip to follow corrugations of the surface. The scanning speed is another essential parameter in STM experiments: it affects the signal/noise ratio of the

resultiing images and depending on the distance between the tip and the sample and the gain level, scanning too fast above a rough surface may cause damage to the tip. On the other hand, too slow a scan may damage the sample surface through tip-sample interactions. The biasing conditions, feedback parameters and scan speed are therefore adjusted depending on the sample's bandgap (or lack thereof), surface roughness and the size of the scanned area. Another less frequently-used STM imaging technique is known as 'constant height imaging'. Here, the height of the tip over the surface is kept constant and changes in the tunnelling current are recorded to form an image. The sample surface must naturally be extremely flat to employ this imaging mode.

Scanning tunnelling spectroscopy on the other hand is based on measuring the tunnelling current as a function of bias voltage between the tip and the sample at a given tip position. When acquring a spectrum, the tip height over the surface is fixed while the bias voltage (±V) is varied. The collected spectra can be represented by plotting either the current (I) versus voltage (V) or the normalized conductance (dI/dV) as a function of the voltage (V). The latter generages spectra that resemble the local density of electronic states (n(e)) versus energy (e) [178]. A schematic of an STM is shown in Figure 3.12.

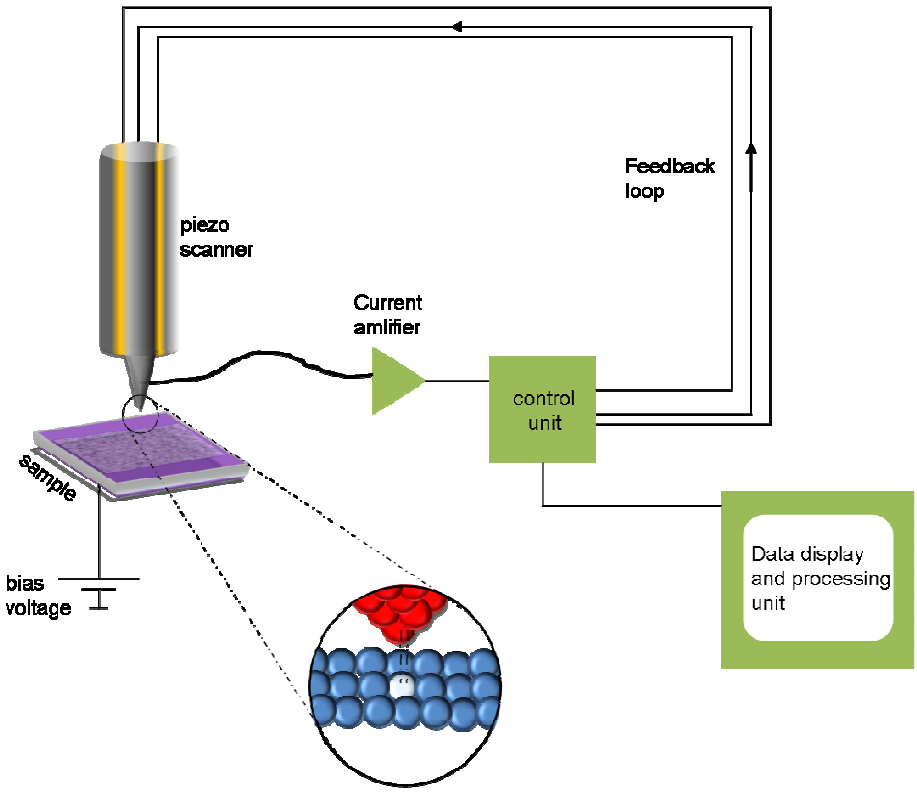

Figure 3.12 Schematic of an STM.

STM instruments are composed of two main UHV chambers. One chamber houses the microscope while the other chamber is used for sample preperation. By having seperate chambers it is possible to maintain a better ultimate pressure in the microscope and thus eliminate contamination from impurity gases such as water vapour, carbon monoxide, carbon dioxide and methane [178]. The STM preparation chamber can be equipped with several tools for surface preparation and analysis: sputter guns, heating stages, low energy electron diffraction detectors and Auger electron spectrometers. STM and STS can also be performed at a range of different temperatures: from high (up to 1500K) to liquid helium temperature (4K). Low temperatures are desirable to do meaningful spectroscopic analysis as stability of the sample is crucial: collecting a spectrum from a single point on the sample might take a few minutes, either because the voltage bias range is large or because a high signal-noise ratio is required. The mobility of adsorbants on the surface of the sample is also minimized at low temperatures, thus increasing the accuracy of the measurements.

3.4.2 Instrument for STM

An Omicron low-temperature UHV STM system with a base pressure of ~10^{-11} mbar in the main chamber and ~10^{-10} mbar in the preparation chamber was used for the experiments. This instrument can be operated from liquid helium up to room temperatures. The maximum scan ranges in the *x* and *y* directions are 10 μm x10 μm, 4 μm x4 μm and 2 μm x2 μm for room, liquid nitrogen and liquid helium temperatures, respectively. A photograph of this Omicron LT-STM system is shown in Figure 3.13.

The tips used to analyse the graphene surface were made of tungsten that has been electrochemically etched in NaOH, then rinsed in DI water and subsequently degassed by annealing in the preparation chamber. The tips were systematically tested by scanning over a known substrate like HOPG or Si(111) in the main chamber.

Figure 3.13 Photograph of the Omicron LT-STM.

Chapter 4

Transmission Electron Microscopy of Graphene

4.1 Introduction

Some of the TEM based graphene studies are reviewed in here to provide a general perspective regarding existing studies that also include some of our own results as introduction to investigations presented later. TEM has been widely used in graphene research for applications as varied as: number of layers determination [14, 92], elemental identification [15, 179, 180], surface roughness (ripples) [92, 181], detection of sheet edge types [107], observation of defects [93, 95] and stacking faults [182, 183], impurities, such as contamination [66] and individual ad-atoms [103], effect of radiation [184, 185] and investigation of graphene based heterostructures [186].

4.2 Identification of Graphene Layers

The TEM is a versatile method to differentiate single-, double- and few- layer graphene through selected area electron diffraction. The layers can be identified from the intensity ratios of the diffraction spots in the diffraction pattern [14, 92]. In addition, diffraction peak intensities vary only weakly with the tilt angle between the graphene membrane and the incident beam for single layer graphene, whereas for bilayers, tilting of a few degrees leads to strong variations in the diffraction intensities [14].

The roughness of suspended graphene membranes can be also studied via diffraction analysis [14] and it is found that the diffraction peaks from monolayers broaden with tilting of the sample but the spot broadening in bilayer samples is approximately half as strong as in monolayers and completely disappears for multilayer graphene or graphite. This spot broadening is attributed to the roughness of graphene membranes, which indicates graphene is not perfectly flat. Researchers also suggested the microscopic roughening could be essential for the structural stability of 2D membranes [92]. In addition to small height variation (few nm) called ripples, graphene also shows macroscopic corrugations (few micrometres). The corrugations can be related to unintentional bending of the supporting grid or mechanical strain during fabrication [187]. In these cases, ripples are claimed not to be intrinsic as opposed to observations by Meyer et al. [92]. Moreover, in

contrast to Meyer et al. [92] and Wang et al.' [188] claiming that the ripples were seen to be static (at least for a certain period of time), changes are observed to occur in specially filtered HREM images over a time period upon defect formation [181]. Researchers stated that the ripple formation is related to local changes in the graphene stiffness, which arises from point defects, so it is argued that point defects facilitated the ripple formation [181]. Hence the origin of the ripples in graphene, whether they are intrinsic features driven by energy minimisation of the 2D structure or are introduced externally, is not perfectly understood [20, 189]. Despite the unclearness, ripples seem to be an intrinsic feature of graphene and other 2Ds, however, the ripples can be more pronounced or enhanced in presence of external agents.

EELS can be used to confirm the presence of single layers and differentiate between one, double and few layers [13, 90]. Experimental studies and DFT calculations of π- and σ+π- surface plasmon modes in free-standing monolayer graphene were found to be compatible with each other and plasmon energies of ~4.5 and ~14.5 eV, respectively, were established, which are substantially shifted from their values in graphite [90]. These plasmon peaks are broadened and their energies shifted up as the number layers increased. However, the presence of hydrocarbon contamination on the graphene surface may alter the EEL spectra values resulting in slightly higher plasmon energies than expected.

As mentioned in Chapter 2, Light microscopy, Raman spectroscopy and AFM studies of graphene are generally used to determine the number of graphene layers. However, these techniques are not straightforward for the determination of the orientation of the layers with respect to each other and of the stacking configuration, whether AB stacked or misoriented, since both types of bi-layer graphene would appear almost the same when analysed by AFM or optical microscopy. To overcome this difficulty electron diffraction is an unambiguous way to identify rotational stacking faults in few layer graphene that reveal themselves in a diffraction pattern by multiple diffraction spots. Rather than having only 6 spots in each ring of the pattern as in the case for single and AB-stacked few layer graphene several orders of 6 spots appear for misoriented layers (6, 12, 18 etc.) where each 6-spot pattern represents one layer [182, 183]. When graphene layers are rotated with respect to each other it gives rise to Moiré patterns and changes the periodicity in the graphene lattice (larger than single- or AB-stacked multi- layer graphene). However, the periodicity depends on the rotation angle that can be determined by measuring the angle between neighbouring diffraction spots in the same ring of the diffraction pattern. Rotation of graphene layers on top of each other is also known as turbostratic graphene.

Turbostratic graphene is frequently observed when grown on Ni [190], grown on SiC [191] and in graphene obtained from graphitic suspensions [182]. The rotation between the layers might be a result of folding of layers during the exfoliation or the transfer process. It has been demonstrated both, theoretically and experimentally, that the graphene layers become electrically decoupled when the layers are misoriented [192]. Parabolic band behaviour of Bernal stacked two layer graphene changes to linear dispersion when the layers are decoupled, meaning a change in the electronic structure upon layer rotation. An external electric field does not open a band gap in the spectrum in case of turbostratic bi-layer graphene unlike in Bernal stacked bi-layer graphene. The Moiré pattern of turbostratic graphene can be also used to determine lattice strain effects because the lattice strain between the layers affects the appearance of the moiré pattern by distorting the hexagonal shape (stretched or/and rotated) of the supercell [191].

4.3 Beam Effects on Graphene in TEM

Electron beam irradiation has a strong effect on the properties of graphitic structures due to knock on damage (vacancy formation) [193]. The carbon knock on energy threshold for graphene is calculated to be ~17 eV per atom. This energy can be transferred to a carbon atom from a 86 kV electron beam [194, 195]. Although the electron dose of the beam is an issue [66], an incident beam with 80 kV or lower is suitable for maintaining graphene defect free in the TEM [13, 107, 184]. However, displacement of carbon atoms from graphene edges and defective regions is known to be easier compared to basal plane damage [107] and is found to be ~14 eV for the edges [102]. Additionally, as more recently suggested beam energies of below ~50 kV should be employed to minimize any knock on damage of graphene in the basal plane, in defective regions and at edges [115]. The radiation damage in graphene or other carbon based systems can be minimized by annealing at moderately high temperatures in the microscope column at high vacuum conditions by giving rise to self repairing mechanism [196]. Moreover, irradiation of nanostructures does not always introduce damage, it can also have beneficial effects such as doping pre-selected areas of graphene sheets and sculpting graphene layers [130].

Electron beams (>80 kV) combined with high temperatures can be used to tailor graphene into desired shapes [110], such as nanoribbons and graphene chains. The latter can be also obtained by narrowing the nanoribbons from both sides down to one carbon

chain under a more energetic electron beam [114, 185]. In these studies, high temperatures were used for self-repairing of vacancies which were created during sculpting and for protection against fast amorphisation which arises under more highly accelerated electron beams at room temperature.

Annealing under extreme heat either by using a hot stage holder [196, 197] or applying bias [198] in a high vacuum environment (inside the TEM column) is also the most efficient way to get rid of hydrocarbon contamination on the graphene surface [66]. Furthermore, amorphous carbon layers can be converted into crystalline structures with high temperature treatment in TEM at around 2000K [199].

Another role of the beam in the microscope is to fill point defects (single or double vacancies) in graphene by nearby adsorbents even at room temperature; this is accepted to be driven only by the electron beam. However, filling a hole rather than a point defect in graphene has not been observed in (S)TEM studies at room temperature until this year [24]. On the other hand, graphene healing has been recently achieved under extreme heat in the range of 400 up to 1200°C in TEM. In addition to high temperature influence, the electron beam (80 kV) was also proven to have a real impact on the healing process as no healing was observed without beam irradiation even at high temperatures [196]. In fact, in this report carbon atoms that were sputtered from the edge of holes and those that were knocked-out of hydrocarbons or out of thick regions are competing in enlarging and filling the hole under the electron beam irradiation. Healing of a hole in graphene has been also shown to occur due to current-assisted annealing at a high bias in the presence of carbon ad-atoms. The temperature due to Joule heating is estimated to reach between 2000 and 3000^{o}C. The healing is suggested to start from the edges of the hole in the graphene by carbon atom addition to the edges [200].

The other known effect of electron beam irradiation is ionization damage, which causes chemical and structural changes of the specimen. Ionization damage is becoming predominant at decreased primary beam energy as the ionization cross-section increases opposite to the knock on cross-section [159]. Graphene ionization damaging in the TEM is also related to vacuum level of the microscope column (due to presence of vacuum contaminations).

4.4 TEM Characterisation of Pristine Graphene

Due to the substantial amount of hydrocarbon contamination, foreign ad-atoms and other residues from the chemicals used during fabrication and transfer graphene layers were found not to be perfectly clean as evidenced by low magnification TEM micrographs. Although presence of contamination can be reduced with careful and cleaner fabrication and transfer procedures, 'unintentional' contamination (due to handling of the samples in air or to residual gases in the TEM column [13, 73] albeit to lower amounts, was observed to exist on the surface at all times. Raw AC-TEM BF and AC-STEM HAADF images of a reasonably large area single layer graphene flake are shown Figure 4.1. It can be clearly seen in both images that clean graphene regions (residue free areas) are limited in size (from few to few hundred nm^2) and surrounded by contamination, which was found to consist of H, C, O and Si in our EDX analysis carried out in the TEM. As seen in fig. 4.1 carbon atoms appear dark and the centres of hexagons (hole sites) bright in the BF image (reversible by changing the focus) and *vice versa* in the HAADF image, here carbon atoms are bright and holes dark. Contaminations are also more visible in HAADF due to higher scattering in regions with heavier atoms and larger thickness.

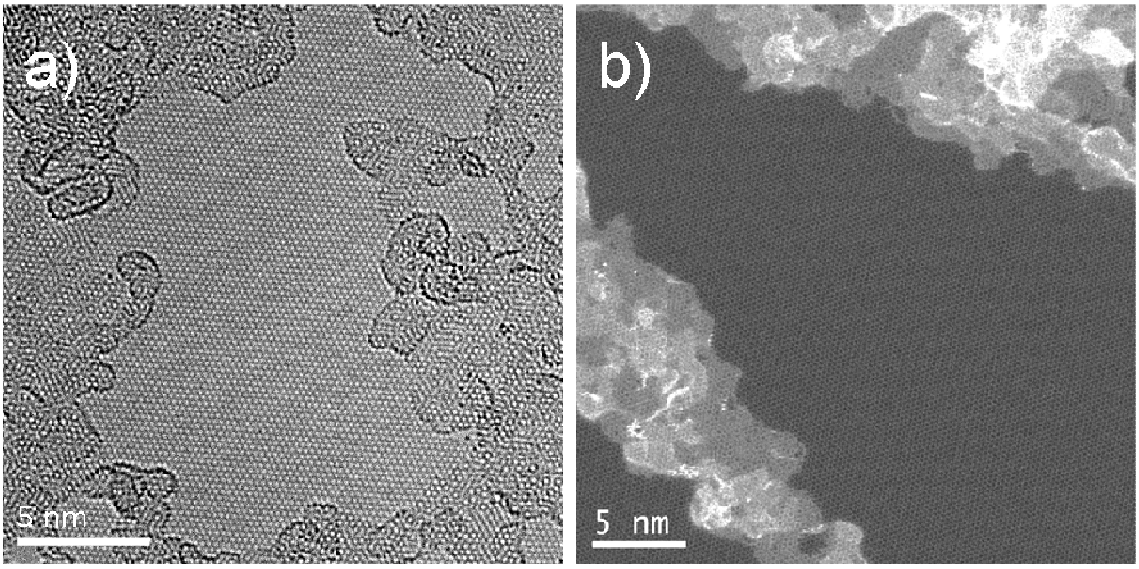

Figure 4.1 High resolution (raw) a) TEM-BF and b) STEM-HAADF images of pristine graphene. The first image was acquired with Jeol ARM 200F and second image with Nion UltraSTEM 100.

TEM electron diffraction is a straightforward technique to distinguish single- from double- and few-layer graphene by comparing the intensities of the first and second ring of the diffraction spots [14, 92]. For single layer graphene the intensity of the outer hexagon

spots is roughly the same as or less than that of the inner one. In contrast, for double layer graphene the outer hexagon intensity is higher than the inner one. Figure 4.2 shows diffraction patterns for single and double layer graphene and their intensity profile.

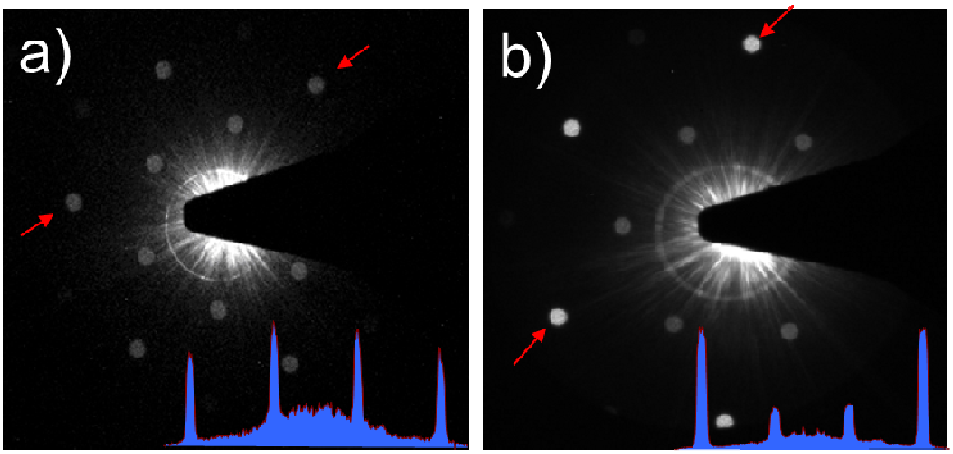

Figure 4.2 Diffraction patterns of a) single layer and b) double layer graphene. Intensity profile plots taken between the red arrows are shown in the inset. The diffraction patterns were acquired with a Tecnai F30.

After identifying monolayer graphene high resolution TEM (HRTEM) and STEM (HAADF) micrographs were recorded. Although both HRTEM and STEM can be used to visualise the graphene structure, STEM-HAADF images are more powerful to identify individual atoms in the lattice due to its approximate Z^2 sensitivity. Thus, atomic resolution STEM was used to visualise the hexagonal atomic structure of graphene as well as individual carbon atoms in the graphene lattice. Atomic resolution STEM- BF and HAADF images of single layer graphene are shown in Figure 4.3a and d, respectively. Although the images are unprocessed and acquired at 60 kV, hexagonal periodicity and individual carbon atoms, especially in the HAADF image, are visible. Simulated STEM-BF and HAADF images with the respective STEM parameters are also shown in fig. 4.3b and c, respectively. The simulations were performed with the Kirkland TEMSIM simulation software [201]. This program uses the multislice approximation to calculate the electron wave function exiting the specimen. In the multislice method the specimen is divided into thin slices and each of these adds a phase shift to the wave function depending on the specimen potential. The incoming plane electron wave interacts with each slice and propagates through the specimen and exits from the last plane [201]. Since STEM (BF and HAADF) image simulation requires a multislice calculation for each point (each position of the probe) in the image, the electron wave function was sampled with 512x512 pixels

but the final image is calculated for 256x256 pixels to reduce computing time. To create a supercell (12x12) for the simulation, atomic coordinates have been generated with the Matlab program. The simulated images look sharper and less noisy than experimental images because the simulations were performed without thermal broadening. Realistic microscope parameters were used, namely 60 keV beam energy, -5nm defocus, -0.03 mm Cs value, 27 mrad convergence angle, 0-6 mrad BF detector and 70-210 mrad HAADF detector angular range.

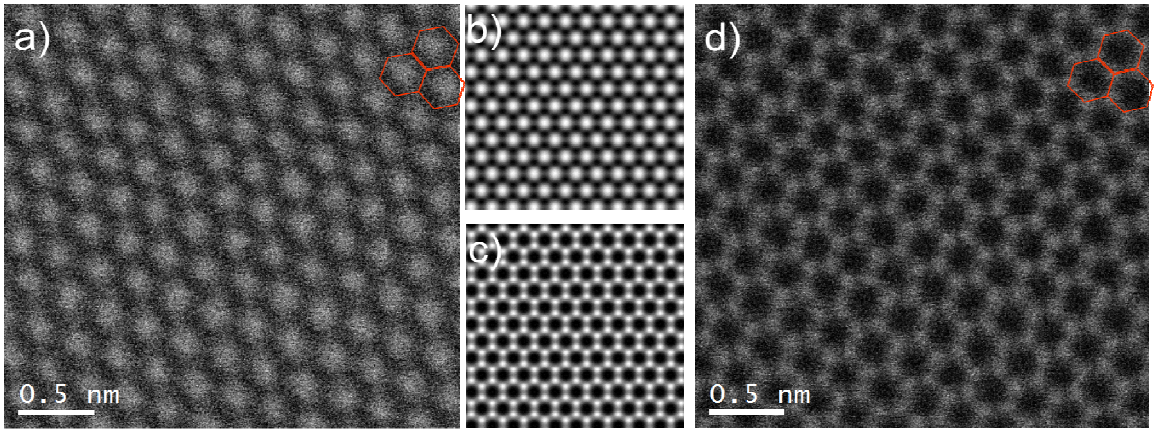

Figure 4.3 Atomic resolution a) experimental raw STEM-BF, b) simulated STEM-BF, c) simulated STEM-HAADF and d) raw experimental STEM-HAADF images of pristine single layer graphene at 60kV.

HAADF images are found to be very useful for observing foreign ad-atoms on/in graphene and most of them can be identified via intensity/contrast analysis by utilising the sensitivity of HAADF images to the atomic number [15, 161]. However, HAADF imaging in combination with EELS dramatically increases the accuracy of chemical analysis. For example, Si, one of the most abundant and stable contaminants in graphene, was observed and identified by simultaneous HAADF imaging and EELS analysis shown in Figure 4.4. The point spectrum was taken on the red circled bright atom, which was identified to be Si by its $L_{2,3}$ absorption edge (energy loss of ~100eV).

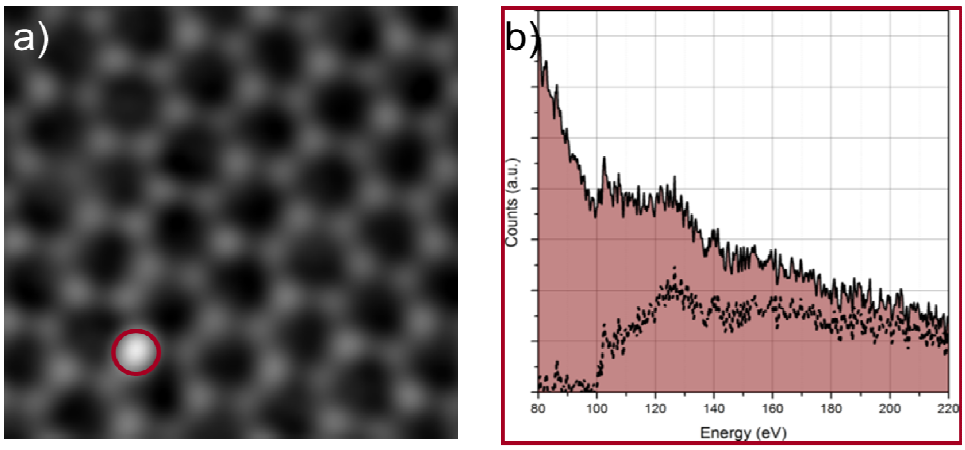

Figure 4.4 a) Noise filtered STEM-HAADF image of single layer graphene with bright atom at bottom left side, b) EEL spectra taken on the red circled bright atom in a) and background subtracted spectra shown as inset with dotted line showing that the bright atom is Si.

Despite being inconvenient, an alternative way to count the layers in graphene sheets is to observe the edges due to the TEM signature of folded regions similar to nanotubes. The layer number can be determined by counting the dark lines at the edge as shown in Figure 4.5. One line in fig. 4.5a and two lines in fig. 4.5b can be seen which represent single and double layer graphene, respectively.

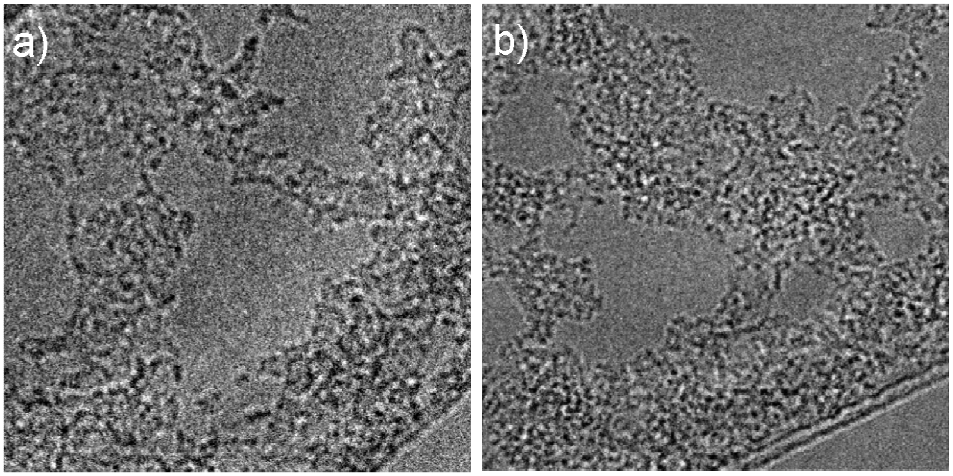

Figure 4.5 BF images of a) single layer and b) double layer graphene identified as such by the number of lines at the edges.

Diffraction patterns and Fourier Transforms (FT) of TEM micrographs are also utilised to identify and observe disordered or misoriented graphene membranes known as turbostratic graphene. The turbostratic double layer graphene were easily identified by

multiple diffraction spots, there are 12 spots in each ring rather than just 6 in and each group of 6 spots arises from different layers [182, 183]. The rotation angles between layers have been found to be vary from 1° to 59° degree. Diffraction patterns for turbostratic graphene are shown in Figure 4.6 and the rotation between layers are 8°, 12° and 30° as measured from neighbouring spots.

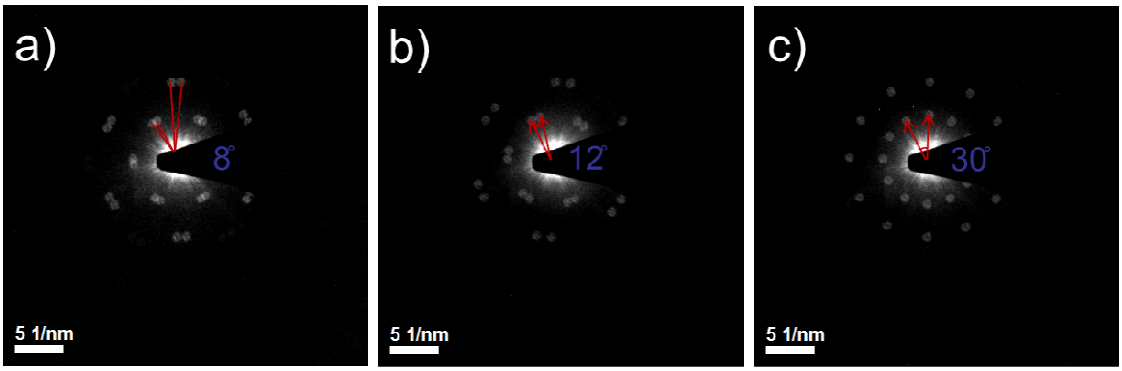

Figure 4.6 Diffraction patterns of turbostratic graphene. The angles between the spots are 8°, 12° and 30° in (a), (b) and (c), respectively.

The Moiré periodicity in the turbostratic graphene is larger than the lattice periodicity of single layer or AB-stacked few layer graphene. This can be clearly seen in a schematic of AB-stacked two layers and turbostratic double layer graphene as shown in Figure 4.7. The Moiré pattern changes with rotation angle, and increasing angles (up to 59^{o}) result in smaller Moiré periodicities.

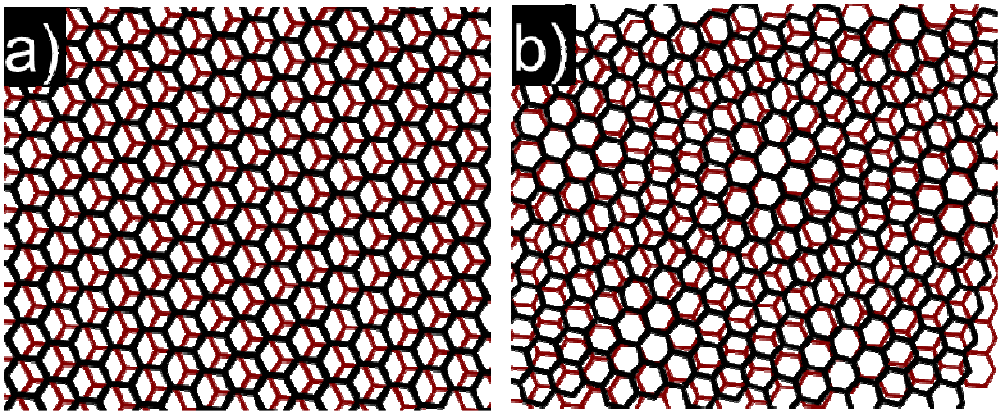

Figure 4.7 Schematic representation of a) AB stacked double layer graphene and b) turbostratic double layer graphene showing a Moiré pattern.

Although diffraction patterns can be used as a straightforward method to identify the presence of turbostratic graphene, it is important to witness the Moiré pattern at a reasonably high magnification because single, double and turbostratic graphene layers

appear quite similar to each other when observed at low magnification. Atomic resolution STEM-BF images of turbostratic graphene are shown in Figure 4.8. The change in the Moiré pattern can be observed as the rotation angle increases resulting in smaller periodicities.

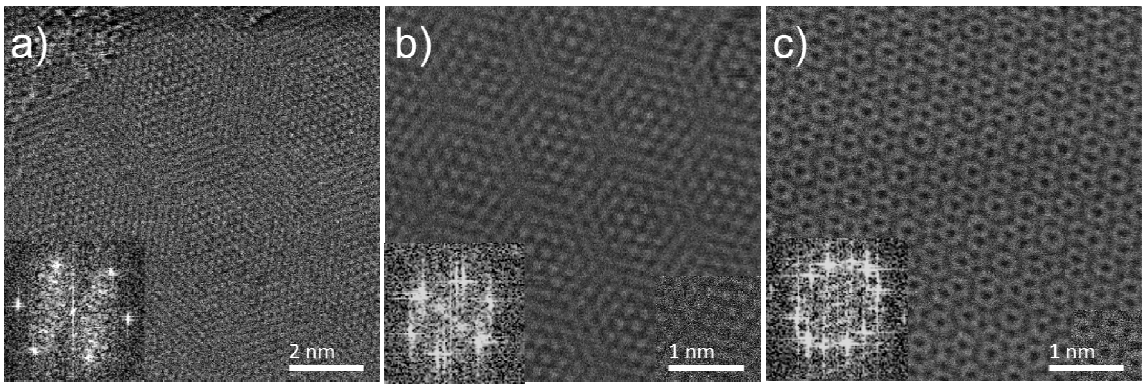

Figure 4.8 Turbostratic double layer graphene STEM-BF images that are taken at 60kV. The rotation angles between the layers are 5^{o}, 8^{o} and 15^{o} in a), b) and c), respectively. The rotation angles are measured on their respective FFTs, shown as insets.

These misalignment in between layers might be formed during exfoliation of graphene with different orientations on top of each other or during the growth process [202], in particular graphene grown on nickel. However, it is not perfectly clear whether they originate from the fabrication process or intrinsic stacking faults (any deviation from known graphite stacking).

Graphene layers are not perfectly flat and show some height fluctuations called ripples. There is a consensus that the ripples in graphene are essential to stabilize 2D materials in 3D [189]. Ripples are important in graphene research due to possible detrimental effect on the transport and mechanical properties [12]. Ripples are frequently observed topographic features for both suspended and supported graphene, however, as previously mentioned, it is still unclear whether they are an intrinsic feature or induced during preparation or measurement [181, 203]. Large ripples (macroscopic) are believed to be induced by the substrate, however, microscopic ripples are accepted to be intrinsic. The latter property was ascertained by broadening of the diffraction spot upon tilting [92], or by special filtering of TEM micrographs [181], or by employing monochromated aberration-corrected microscope [188]. In the latter case the monochromation expand temporal coherence envelope function which increases information limit by reducing the energy spread and thus enhances the local contrast for a small tilt of the graphene surface that

resulting from the ripples. The wave length and amplitude of ripples is suppressed for few layer graphene and almost no ripples are observed in graphite even at large scale [188]. However, relatively small sized ripples were observed directly with an aberration corrected STEM probe due to the small focus depth without monochromator or special filtering as shown in Figure 4.9. Due to the height differences in the middle right of the 5x5nm frame, the focus is changing in the rippled region relative to the rest of the area this leads to visualisation of topography. However, due to limited size of the frame it was not possible to determine the wavelength of the ripple exactly. Both figures are the same and unfiltered HAADF images taken at 60 kV in SuperSTEM. False colour has been used for better visualisation of the ripples in the fig. 4.9b.

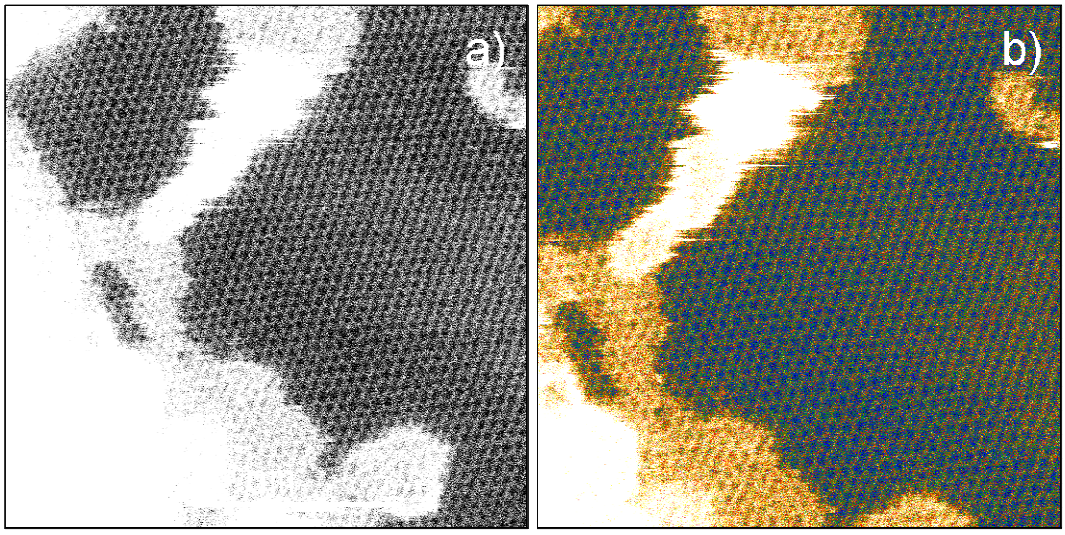

Figure 4.9 a) STEM-HAADF images of rippled single layer graphene and b) false colour image of (a).

Chapter 5

Scanning Tunnelling Microscopy of Graphene

5.1 Introduction

It was decided to combine TEM and STM techniques to compare the results with regards to detailed information of the topography and the metal-graphene interaction, in particular gaining electronic information by spectroscopic measurements. Metals have been extensively studied on supported graphene up to date by STM, so STM studies would not have provided new informations about those interactions, and would furthermore not be comaprable to TEM data, unless such studies will be done on suspended graphene. Thus, as one of the main challanges STM would have to be carried out on suspended membranes. As well as eliminating the substrate effect, the ability to anneal the graphene samples to get rid of organic contamination, in-situ metal depositions and investigations in the UHV system makes STM a powerful technique to investigate graphene-metal interfaces. Performing preparations and experiments in the same instrument in UHV minimises most of the possible contaminations, such as air exposure of the sample during handling. STM also provides much control over the metal deposition that can be performed at variable temperatures which will also affect the metal behaviour.

As mentioned above STM studies of single layer graphene have so far been performed mainly on a substrate onto which the graphene was grown or transferred [85, 204]. However, quasi suspended graphene layers have been studied on graphite [176, 177] and on SiO_2 [203] due to decoupling of the layers in the first case and due to the substrate surface roughness in the second case. In addition, there are some recent attempts to study suspended graphene samples [177], however, the investigation of truly suspended graphene has not been achieved yet.

Here a technique has been developped to study truly suspended graphene membranes in the STM. Annealing of the graphene membranes was found to be crucial to rid the surface of most of the organic contaminations as these are preferential nucleation sites for the metal ad-atoms and clusters as will be shown in Chapter 6 and 7 in our (S)TEM studies. The metal deposition on the graphene samples for the TEM studies was performed as ex-situ with poorer vacuum conditions (~10^{-8} - 10^{-6} mbar) so using UHV for metal

evaporation can minimize oxidation of the metals during evaporation. Discarding the subtrate impact, getting rid of the contaminations on the surface and in-situ metal deposition in UHV at different temperatures are the main goals behind the project to analyse the effect of metals on the physical and electronic properties of graphene. STM studies of suspended pristine graphene have been achieved as a part of the project, however, investigations of the metal- graphene interaction are still underway.

5.2 Methodology

The CVD-grown graphene layers were used to make suspended graphene membranes for STM investigations. TEM grids were used to be able to suspend the graphene layers. Lacey carbon and quantifoil TEM grids were used to provide the necessary mechanical support for graphene membranes. Layers grown on copper substrates were transferred to these TEM grids in the same way as in the preparation of TEM samples. However, the specimen has to be fixed on a flat plate for the STM experiments. Thus, ahead of loading the sample to the STM chamber the grid was mounted to specially designed sample carrier which provides mechanical support and does not affect its suspended form. The grid carrier consists of two metal pieces between which the grid is fixed as shown in Figure 5.1.

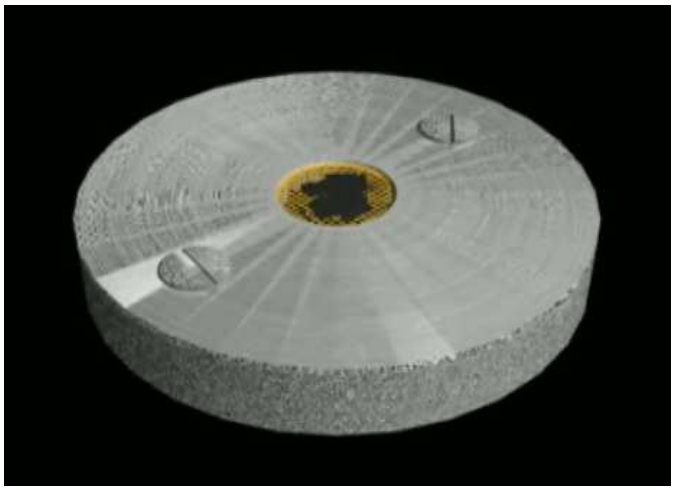

Figure 5.1 Schematic of the TEM grid carrier. The grid is at the center of the carrier with the graphene layers on it.

An Omicron low-temperature UHV STM system with base pressure of ~10^{-11} mbar in the main chamber was used in the experiments. An electrochemically etched tungsten tip was tested for its sharpness on Si(111) or graphite surfaces because of their well-known

structure and flatness. The STM data for suspended graphene were obtained only at room temperature.

5.3 STM Characterisation of Pristine Graphene

Before investigating suspended graphene, CVD-grown graphene layers were studied as grown on the copper substrate. STM data were taken at liquid nitrogen temperature (77K). Prior to scanning the graphene surface on the copper, the samples were initially degassed for few hours at <100°C and then annealed at elevated temperature ranging from 400°C to 600°C for few hours or overnight depending on the cleanliness of the surface. The annealing enabled to study residue free graphene surfaces [66, 205]; without these cleaning procedures STM imaging of graphene was found to be almost impossible. Figure 5.2 shows low and high magnification unprocessed STM images of single layer graphene on the copper upon annealing. The experimental data were analysed by using the WSxM software [206].

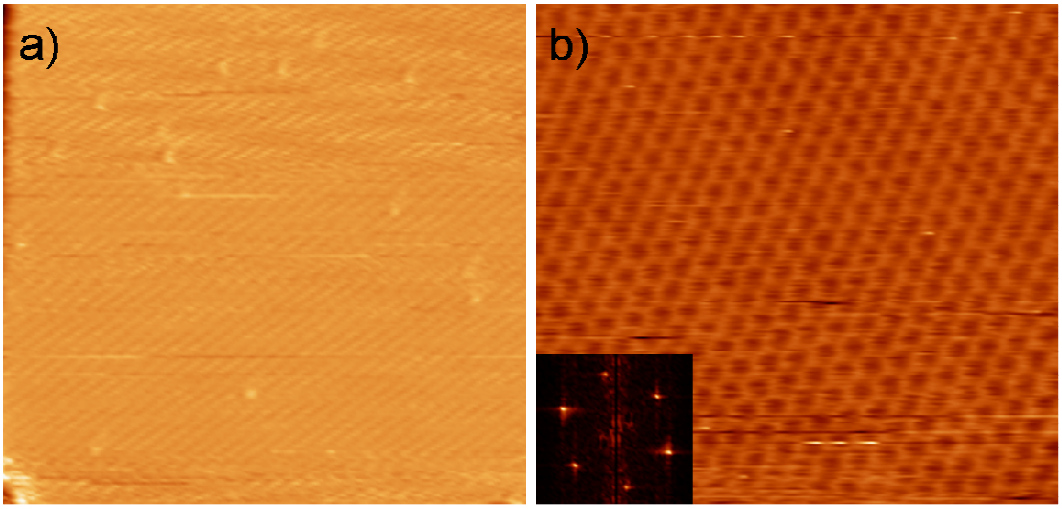

Figure 5.2 Unprocessed STM images of CVD-grown single layer graphene on a copper surface, a) 35nm frame and b) 5nm frame and its FFT shown as inset indicating the hexagonal symmetry of the graphene.

As well as obtaining atomic resolution imaging of graphene, detailed STM-constant current imaging of graphene on copper has lead to many different observations, such as ripples, wrinkles, buckling and Moiré patterns. The wrinkles that are random corrugations (larger than ripples) of the graphene surface most probably were formed during the growth followed by a fast cooling step in the CVD chamber, or

it might have been introduced during annealing due to the opposite sign of the expansion coefficient of graphene and copper [205]; whilst copper shrinks during cooling graphene expands resulting in wrinkle formation to release the induced strain [207]. The observed wrinkles are between 2 and 4 nm in width and up to 1.4 nm in height. Figure 5.3a shows a 20x20 nm frame of a wrinkled area of graphene on copper and an enlarged area of fig. 5.3a is shown in fig. 5.3b. Due to height diffrences on the wrinkle, the structure could not be resolved everywhere in the fig. 5.3. Corrugations are seen much more clearly in 3D representations of the images, shown as insets.

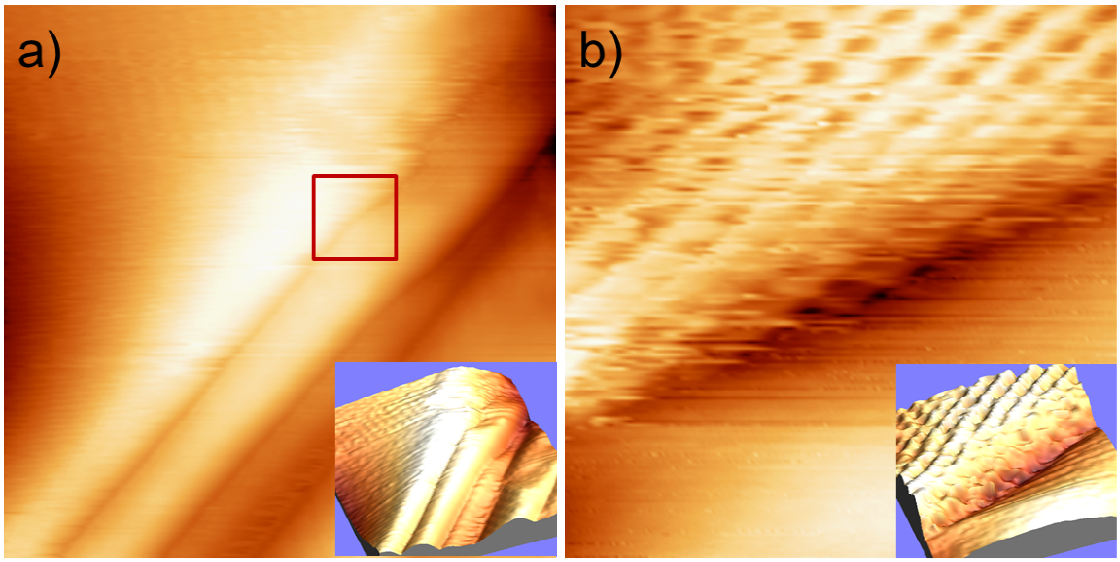

Figure 5.3 Corrugated single layer graphene STM images on a copper surface a) 20nm frame and b) 3nm frame which is the enlarged image of the red square in (a). 3D representations are shown as insets.

Due to lattice mismatch between the graphene and the underlying copper or as a result of rotation of the graphene layer on the copper surface, Moiré patterns have been observed frequently when a reasonably large area was scanned [85, 205, 207, 208]. Similar to turbostratic double layer graphene in the TEM, when the rotation angle increases a smaller Moiré periodicities have been observed for graphene on copper in the STM. Similar patterns were witnessed in our work for graphene grown on polycrystal copper rather than single crystal Cu(111). Polycrystalline copper has two major orientations that are predominantly Cu(100) and to a lesser extent, Cu(110). Thus, different Moiré patterns could in principle be observed even without layer rotations. Two different Moiré patterns are observed in our investiagtions as shown in Figure 5.4. However, without additional experiments like XRD we cannot confirm

directly from these images whether they are arose as a result of different orientations of the polycrystalline copper or rotation of the layers.

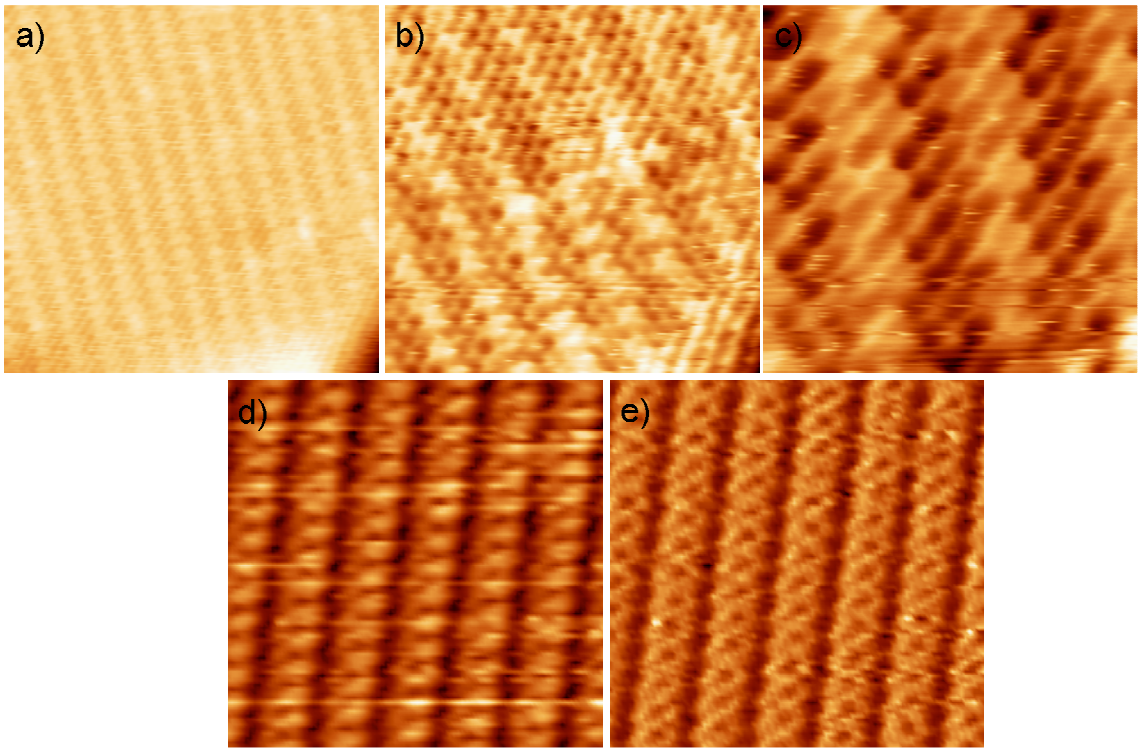

Figure 5.4 Moiré appearance of single layer graphene on copper surface 10nm, 5nm and 2.5nm frames in a), b) and c) respectively, taken of the same area by zooming in. Simultaneously taken d) STM constant height image and e) STM current image of another Moiré pattern with clearly resolved atomic structure (5nm frame).

Steps on the copper surface and how the graphene film follow the steps were also observed during the STM experiments. Figure 5.5a shows an overview image of the graphene on copper along with its 3D representation in which the steps, in fact multisteps, are clearly observable. The graphene layers are continuous throughout the step edges. This is shown in the atomically resolved image in fig. 5.5c, which is the magnified area of the blue square in fig. 5.5a.

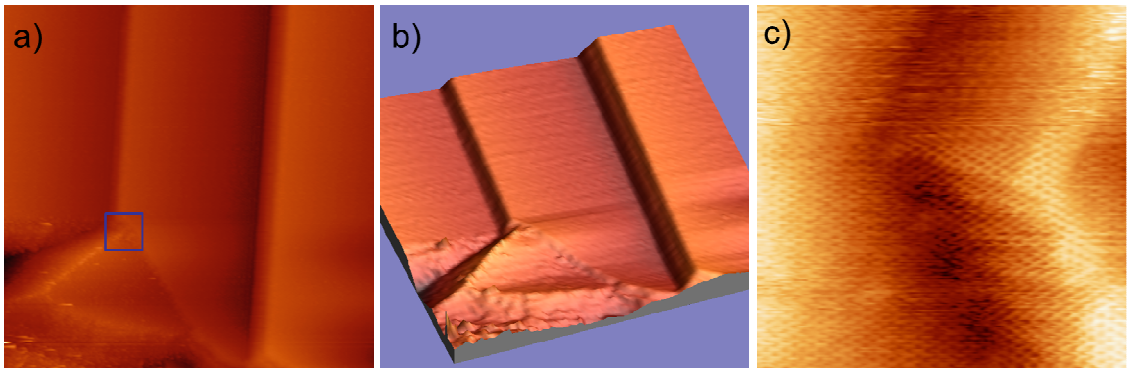

Figure 5.5 CVD-grown graphene are shown to follow the surface and steps on copper. a) an overview STM image of single layer graphene, 100nm frame, b) 3D representation of (a) showing multisteps of copper and c) magnified image of the blue square in (a), 10nm.

5.4 Results and Discussion

The results of this project were published in Nanoscale in 2012. The original manuscript for **"Scanning Tunnelling Microscopy of Suspended Graphene"** *(Nanoscale, 2012, 4, p.3065)* is presented below.

Scanning Tunnelling Microscopy of Suspended Graphene

Recep Zan, Chris Muryn, Ursel Bangert, Philip Mattocks, Paul Wincott, David Vaughan, Xuesong Li, Luigi Colombo, Rodney S Ruoff, Bruce Hamilton, Konstantin S Novoselov

Nanoscale, 2012, 4, p.3065

ABSTRACT

Suspended graphene has been studied by STM for the first time. Atomic resolution on mono- and bi-layer graphene samples has been obtained after ridding the graphene surface of contamination via high-temperature annealing. Static local corrugations (ripples) have been observed on both types of structures.

TOC

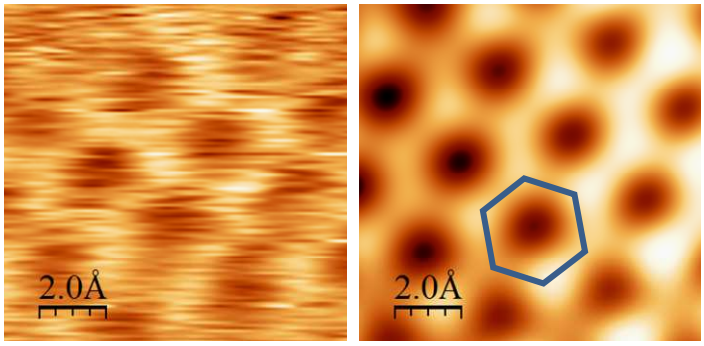

Graphene offers new, unexplored opportunities in surface science: it is a rare case of surface without a bulk, so the methods of surface science give us unique information about this material. Scanning tunnelling microscopy (STM), in particular, is a powerful technique for studying surface morphology as well as electronic structure on the atomic scale. STM studies of graphene have been carried out for material prepared on a number of substrates such as SiO_2, SiC, Cu, Ir, Ru and others.[1-8] The graphene layers prepared on these substrates were obtained by different techniques, for example by

exfoliation,[9] chemical vapour deposition (CVD) using different types of gases (e.g., methane or ethylene) on different substrates,[10-12] as well as by graphitization of SiC.[13] Characterization of such films has typically exploited Z-imaging scanning tunnelling spectroscopy (STS) and low energy diffraction pattern analysis, all in situ and in UHV. Initial reports involved pure graphene,[1-5, 7] but STM analysis of metal clusters on graphene has also been performed, exploiting the crystallographic quality and chemical stability of graphene as a substrate for cluster measurement.[1, 8, 14, 15] Graphene was also studied on graphite via STM where graphene flakes had decoupled from the substrate and showed characteristic behaviour of monolayer graphene.[6] Geringer et al.[16] claimed that quasi-suspended graphene was studied since the roughness of the SiO_2 substrate is higher than that of the graphene on top of it, implying that some areas of the graphene do not touch the surface, and hence suspended regions are present. Luican et al.[17] have also recently attempted to study graphene on transmission electron microscopy (TEM) grids using STM; they have imaged graphene layers on non-suspended parts of the sample, i.e., on grid bars, but they were unable to image suspended regions of graphene because they consisted of relatively large areas, causing excessive spatial fluctuations for STM imaging, even at 4K. Truly suspended graphene has so far been studied mainly in TEM.[18, 19] Both, theory [20, 21] and experiment [8, 22] suggest that the substrates on which graphene is typically deposited, for characterisation and for applications, have a significant influence on its properties. Because of this and because of uncertainties concerning the invasiveness of TEM or STEM experiments as a result of the high energy density of the electron beam even at energies below the displacement threshold of carbon atoms in graphene (i.e. <80 keV),[23, 24] we have attempted STM z-image studies of freely suspended graphene. Here we present for the first time examples of atomic scale resolution imaging of freely suspended graphene layers which point to the conclusion that nanoscale, temporally static ripples can be reproducibly observed, at least with the preparation and suspension methods described. The ability to obtain such data rests largely on in-situ cleaning procedures used, which we also outline in this paper.

The graphene samples used in this experiment were grown by chemical vapour deposition (CVD) onto copper substrates.[11] The graphene on Cu was then spin-coated with poly-methyl methacrylate (PMMA) to provide mechanical support and to facilitate handling after Cu substrate removal. The Cu substrate was etched away in a 0.1 molar ammonium persulphate ($(NH4)_2S_2O_8$) solution, rinsed in deionised water, and then

transferred to a 400 mesh lacey-carbon-coated Cu grid. The lacey carbon network coating consists of narrow (50nm) interconnected strips of amorphous carbon bordering holes of a few microns in diameter, providing a predominantly open structure, thus giving rise to suspended graphene over about 90% of the area. The fact that the suspended parts are only few microns in diameter and conducting measurements in the proximity of the grid bar, helped ensure the mechanical stability of the graphene on the carbon coated Cu grid during the experiment. The PMMA was subsequently dissolved by immersion in acetone for a few minutes. The TEM grid was then dried in a critical point dryer to avoid collapse or deformation of the membranes due to surface tension. The transfer of graphene involves chemical treatment, and so residues, e.g., PMMA and other unintentional impurities, may be left on the graphene surface, which affect the imaging conditions in the STM. In fact, introduction of chemical surface contamination at some level is common for all film transfer or processing steps, e.g. similar residues are likely to form as a result of lithographic procedures when defining contacts or mesa structure on graphene on nonconductive surfaces like SiO_2.

Both UHV RHK and Omicron low-temperature UHV STM systems (residual pressure 10-10 mbar) and electrochemically etched tungsten tips, formed and cleaned in UHV, were used to analyze the surface of graphene in our experiments. All STM data were taken at room temperature (300 K) and sample-tip bias voltages were typically between 0.5V and 1.5V with tunnel currents ranging from 0.1 nA to 1.0 nA; for atomic resolution a higher tunnelling current was used. To ensure optimised tip performance, gold on mica and graphite (HOPG) samples were used as references. Also, in order to ensure that tunnelling was occurring on the suspended parts, we systematically took images at small spatial separation across entire grid squares with all high quality images yielding similar result, which was repeated on a number of different samples. In the following we demonstrate an annealing process to minimize residue on the suspended graphene, as well as hexagonal and triangular atomic structure and topographic ripples. The experimental data were analysed by using WSxM software.[25]

Prior to mounting the TEM grid in the STM chamber, we ascertained the presence of graphene flakes and their coverage in the TEM, and ensured, via electron diffraction, that the deposited material was predominantly monolayer graphene: the films we used also showed the presence of bilayer regions over less than 5% of the sample area. Unfortunately most of the area was covered with polymeric, hydrocarbon residue,

from, e.g, the PMMA, as described above as a result of wet chemistry, consisting of carbon, oxygen and hydrogen, as revealed by our EDS and EELS measurements. This residue sometimes forms randomly oriented thick amorphous layers, The residue also contains metal impurities from the growth substrate e.g., Cu, and inevitably Si, a well known impurity on graphene regardless of the production method. Thus only small, nanometre scale clean patches exist on the untreated graphene surface, as is commonly observed in TEM studies,[24] (fig. 1a). Better surface preparation techniques will have to be employed to have access to residue free graphene.

Since we observed surface contamination, principally consisting of hydrocarbons, on the graphene surface by TEM, we annealed the graphene in both TEM and STM in UHV environment at various temperatures, ranging from 50^{o}C to 550^{o}C in an attempt to find the best conditions to achieve stable tunnelling and good image quality. Figure 1 shows TEM and STM images of suspended graphene before and after annealing; these indicate presence of residue (figs. 1(a) and (c)) and effects of annealing at elevated temperatures (figs. 1(b) and (d)). It is clear from both TEM and STM images that annealing at 550^{o}C shows the cleanest surface and stable tunnelling in STM.

By further exploring the annealing regimes in terms of time and temperature it was found that annealing for 24 hours at 500°C is usually sufficient to remove almost all organic (hydrocabon) contamination, so the size of the clean graphene patches has increased from few nm^2 to several hundreds of nm^2 (see inset fig. 1(b)), and with a well formed tip we were able to obtain atomic resolution images (Fig. 2).

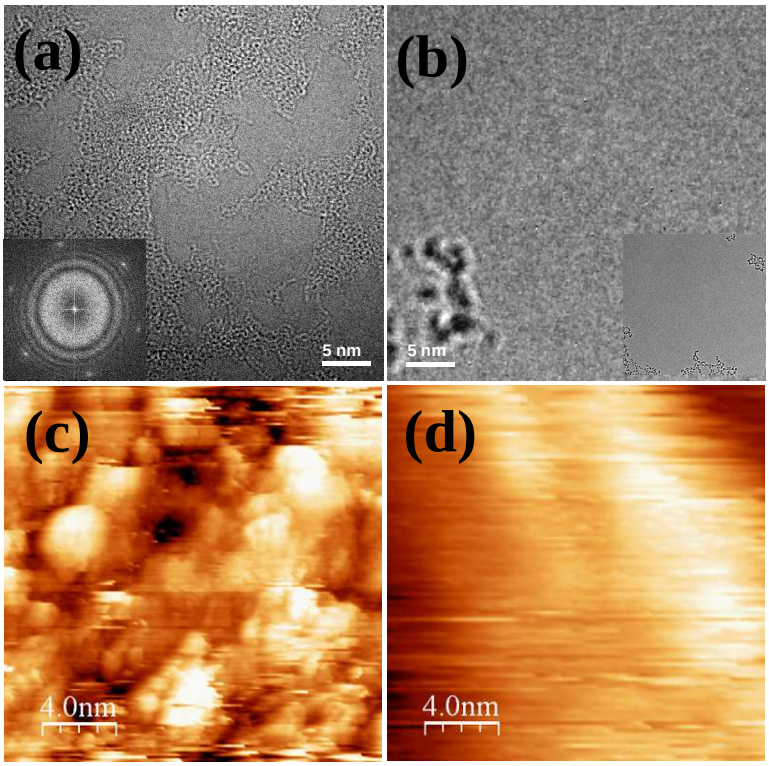

Fig.1 TEM images of suspended graphene (a) before annealing with FFT shown in the inset; (b) after annealing at 550°C for few hours, a low magnification image shown in inset (700nm^2 frame); STM images (c) before annealing; (d) After annealing at 550°C. All images represent raw data. The STM scanning conditions were: tunnelling voltage of 0.5-1.5 V, current 0.1-1 nA.

A clear honeycomb monolayer structure was observed with an interatomic distance of 1.4 Å, consistent with literature values. Consequently fig. 2(a) shows six spots in the Fourier transform (inset), indicative of the graphene lattice. This cleaning procedure allowed us to acquire atomic resolution graphene images at almost every probing position on the suspended layer.

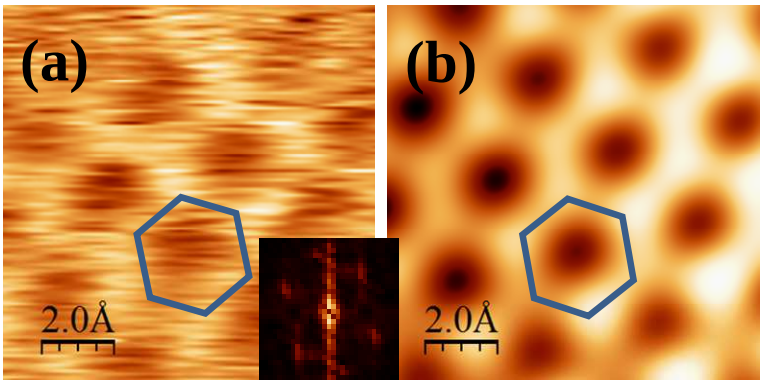

Fig. 2 High resolution STM images of monolayer graphene. (a) Raw and (b) FFT filtered image. Hexagonal monolayer structure can be observed in both images. The image acquisition parameters were: V_{bias} = +0.6 V and I = 0.3 nA. Inset in shows the FFT.

In some areas of the sample both hexagonal and triangular structures were observed in a single image frame, corresponding to monolayer and bilayer graphene respectively, as shown by the raw and FFT filtered images of such regions in figs. 3(a) and 3(b), respectively.

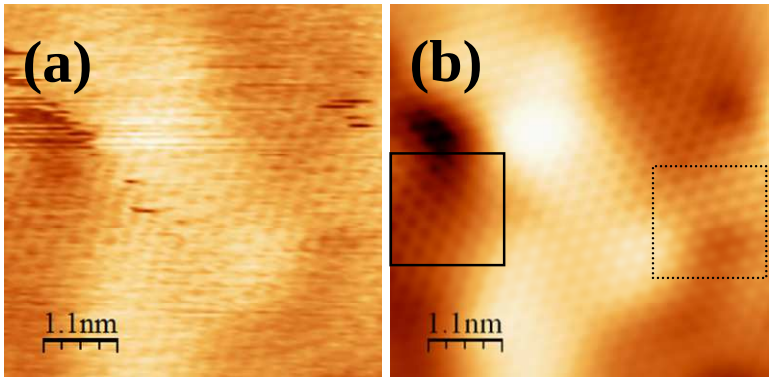

Fig. 3 High resolution monolayer and bilayer graphene region. (a) Raw and (b) FFT filtered images. Hexagonal monolayer (solid line square) and triangular bilayer (dotted line square) structures can be observed in both images. The image acquisition parameters were: V_{bias} = +0.6 V and I = 0.5 nA.

The stability of 2-D structures has long been debated,[26, 27] and ripples in graphene layers, although commonly imaged in supported films,[2, 4, 16] are of great interest. Their origin, whether they are intrinsically driven by energy minimisation of the 2-D structure[28] or are rather due to essentially extrinsic phenomena, has not been resolved in the existing literature. Many such extrinsic causes could exist depending on sample

preparation e.g. defect mediated local changes in graphene stiffness, unintentional bending of a supporting grid or mechanical strain during fabrication.[29] Equally, the question as to whether these ripples are dynamic or static, is a subject of great interest and is hitherto unresolved. In a previous STEM study,[30] using Fourier filtering procedures, we have shown that ripples in mono-layer graphene have wavelengths on the scale of 5 to 10 nm, and amplitudes of typically 0.5 nm. Ripple patterns observed in the STEM have proven to change in subsequent scans, being strongly influenced by the time varying point defect distribution which is driven by the electron beam interactions with the film. In the present STM images of suspended graphene we observe distinct topographic ripple features, which strongly resemble the ripples of STEM data in terms of shape, wavelength and height. We have systematically imaged graphene addressing many different areas of suspended material, and conducting repeat scans in given areas. In doing so we established the general topography and also the stability of ripples in suspended graphene; examples are given in figs. 4(a) and (b), where height variations (ripple amplitude) of the order of 1 nm were observed. A line profile (blue dotted line in fig. 4(b)) shows the height variation across a 10 nm frame size in the inset fig. 4(b). The images of figs. 4(a) and (b) represent the first and last in long sequence of repeated imaging. The ripples are stable, i.e. no changes, aside from small sample drift, are detected over a time period of about 5 minutes of continuous imaging. The same situation, on a magnified scale, is evident in figs. 4(c) and 4(d), showing a different area of graphene. Again, the images of figs. 4(c) and 4(d) are the first and the last of a series. The ripple amplitude here is about 4Å, which can be seen from line profile shown in the inset. In both sets of images (a,b and c,d) the lateral periodicity or wavelength of the ripples is a few (~5) nm.

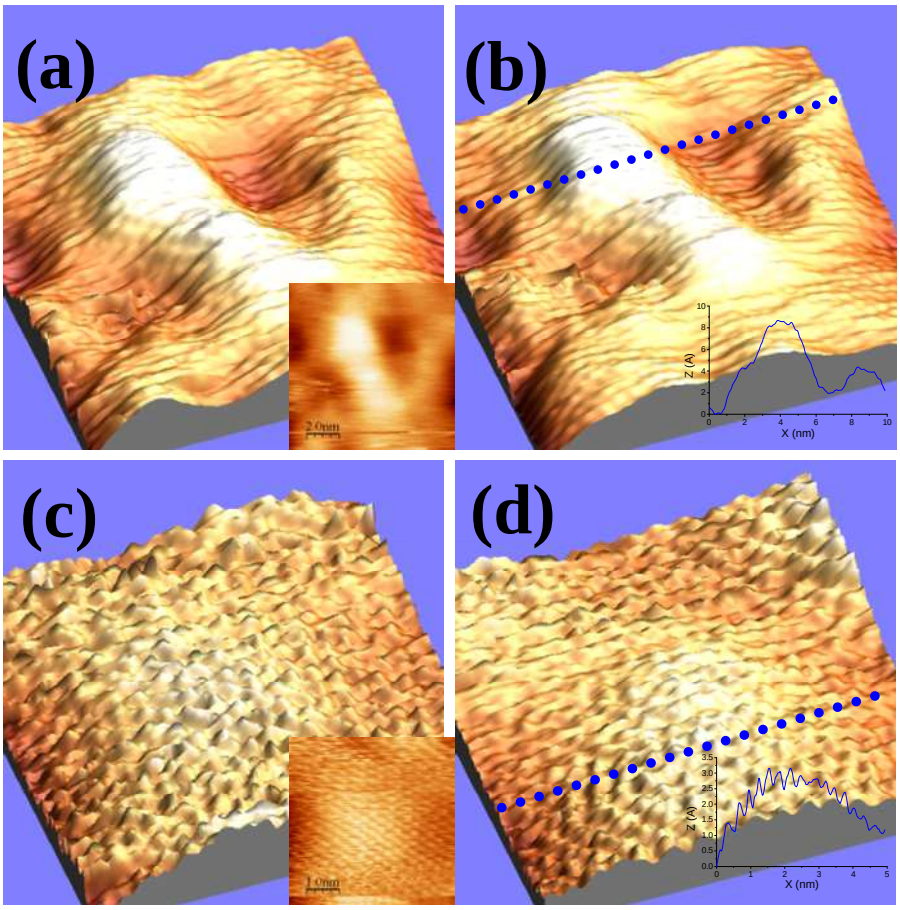

Fig. 4 High resolution 3D STM images of monolayer graphene. (a) First and (b) last image from an image series showing a $10nm^2$ area; (c) first and (d) last image from an image series showing a $5nm^2$ area. Both image pairs demonstrate that the ripples are static. The acquisition parameters were: V_{bias} = +0.6 V and I = 0.5 nA for (a) and (b) and 0.8V and 0.6nA for c, and d. Insets in (a) and (c) show the 2D counterparts. Insets in (b) and (d) show a line profile taken along the blue dotted lines.

Stolyarova et al.[2] and Ishigami et al.[4] have attributed such ripples to the interaction between graphene and the underlying substrate surface (in their case silicon dioxide) whose roughness may have led to corrugations with strong and defined patterns; they do not ascribe the ripples to intrinsic properties of graphene, in contrast to observations by Geringer et al.[16] However, in the absence of any substrate or support, our measurements on suspended graphene strongly suggest that the observed ripples are not related to substrate interactions so they might be either formed via an interaction with the still present contamination or an intrinsic feature of graphene or as a result of the interaction between the tip and the graphene flake. However, the latter is unlikely because no change has been observed on the ripples appearances as is stated above.

We can also elimate ripple formation as a result of impurities left on graphene by scanning areas of tens of nm^2 where no contamination is observed. The ripples we observe in unsupported graphene are static in nature; the long term stability and reproducibility of the images and the ability to perform atomic resolution imaging both mitigate against a ripple structure which is varying on any time frame that would perturb STM imaging. Equally the bias polarity independence of our images strongly supports the view that topology rather than electronic image information is present in these images.

It is important to note that STM z-images are sensitive to both, the surface local density of states (LDOS) variation and topology variation. The sensitivity of the STM tip response to each of these is a strong function of tip proximity and tunnelling current. The measurement conditons may be tuned to enhance sensitivity to electronic phenomena (electron density or LDOS magnitude) or to topology.[31] In general a high tunnelling current enhances LDOS sensitivity. Such considerations have been applied to STM imaging of graphene grown by CVD onto polycrystalline copper by Xu et al.[32] These workers optimised the LDOS imaging of filled states and showed that the high values of LDOS characteristic of graphene produced a near sinusoidal and unusually large z variation of the tip, with a spatial period of 0.25-3 nm and an amplitude of around 0.05 nm. This degree of tip displacement is a direct conseqence of the unusually high density of filled states in graphene. The same sinusoidal ripple structure is seen in this work (Figure 4(d)); it is the filled state LDOS response as the tip passes over each hexagonal benzene ring structure. However the gross ripple structure measured here corrseponds to tip displacement around one order of magnitude greater than that resulting from the graphene LDOS and can only be assigned to topological variation in these unsupported films.

In conclusion, suspended graphene has been studied in the STM for the first time. Annealing conditions have been established for imaging free-standing graphene membranes with atomic resolution and both, monolayer and bilayer regions as well as ripples were observed. The ripples were stable over the entire measurement period, and hence appear to be static. The here established imaging conditions set the scene for future spectroscopic investigations of suspended graphene at low temperature in the STM (I-V), which are expected to provide new experimental insight into intrinsic and fundamental properties of pristine graphene, through elimination of substrate and impurity effects.

Notes and references

[a,] School of Physics and Astronomy, The University of Manchester, Manchester, M13 9PL, United Kingdom; *Tel: 0044 161 306 2255; E-mail: recepzan@gmail.com*
[b] School of Materials, The University of Manchester, Manchester, M13 9PL, United Kingdom
[c] *School of Chemistry, The University of Manchester, Manchester, M13 9PL, United Kingdom*
[d] *Photon Science Institute,* The University of Manchester, Manchester, M13 9PL, United Kingdom
[e]*School of Earth, Atmospheric and Environmental Sciences,* The University of Manchester, Manchester, M13 9PL, United Kingdom
[f] *Department of Mechanical Engineering and the Materials Science and Engineering Program, The University of Texas at Austin, Austin, TX, 78712, US*
[g] *IBM, T.J. Watson Research Center, Yorktown, NY*
[h] *Texas Instruments Incorporated, Dallas, TX 75243*

1. A. T. N'Diaye, S. Bleikamp, P. J. Feibelman and T. Michely, Physical Review Letters, 2006, 97, 215501.
2. E. Stolyarova, K. T. Rim, S. Ryu, J. Maultzsch, P. Kim, L. E. Brus, T. F. Heinz, M. S. Hybertsen and G. W. Flynn, Proceedings of the National Academy of Sciences, 2007, 104, 9209-9212.
3. P. Mallet, F. Varchon, C. Naud, L. Magaud, C. Berger and J. Y. Veuillen, Physical Review B, 2007, 76, 041403.
4. M. Ishigami, J. H. Chen, W. G. Cullen, M. S. Fuhrer and E. D. Williams, Nano Letters, 2007, 7, 1643-1648.
5. K. Xu, P. Cao and J. R. Heath, Nano Letters, 2009, 9, 4446-4451.
6. G. Li, A. Luican and E. Y. Andrei, Physical Review Letters, 2009, 102, 176804.
7. L. Gao, J. R. Guest and N. P. Guisinger, Nano Letters, 2010, 10, 3512-3516.
8. Z. Zhou, F. Gao and D. W. Goodman, Surface Science, 2010, 604, L31-L38.
9. K. S. Novoselov, A. K. Geim, S. V. Morozov, D. Jiang, Y. Zhang, S. V. Dubonos, I. V. Grigorieva and A. A. Firsov, Science, 2004, 306, 666-669.
10. A. Reina, X. Jia, J. Ho, D. Nezich, H. Son, V. Bulovic, M. S. Dresselhaus and J. Kong, Nano Letters, 2008, 9, 30-35.
11. X. Li, W. Cai, J. An, S. Kim, J. Nah, D. Yang, R. Piner, A. Velamakanni, I. Jung, E. Tutuc, S. K. Banerjee, L. Colombo and R. S. Ruoff, Science, 2009, 324, 1312-1314.
12. K. S. Kim, Y. Zhao, H. Jang, S. Y. Lee, J. M. Kim, K. S. Kim, J.-H. Ahn, P. Kim, J.-Y. Choi and B. H. Hong, Nature, 2009, 457, 706-710.
13. C. Berger, Z. Song, X. Li, X. Wu, N. Brown, C. C. Naud, D. Mayou, T. Li, J. Hass, A. N. Marchenkov, E. H. Conrad, P. N. First and W. A. de Heer, Science, 2006, 312, 1191-1196.
14. B. Premlal, M. Cranney, F. Vonau, D. Aubel, D. Casterman, M. M. De Souza and L. Simon, Applied Physics Letters, 2009, 94, 263115-263113.

15. M. Sicot, S. Bouvron, O. Zander, U. Rudiger, Y. S. Dedkov and M. Fonin, Applied Physics Letters, 2010, 96, 093115-093113.
16. V. Geringer, M. Liebmann, T. Echtermeyer, S. Runte, M. Schmidt, R. Ruckamp, M. C. Lemme and M. Morgenstern, Physical Review Letters, 2009, 102, 076102.
17. A. Luican, G. Li, A. Reina, J. Kong, R. R. Nair, K. S. Novoselov, A. K. Geim and E. Y. Andrei, Physical Review Letters, 2011, 106, 126802.
18. J. C. Meyer, A. K. Geim, M. I. Katsnelson, K. S. Novoselov, T. J. Booth and S. Roth, Nature, 2007, 446, 60-63.
19. R. Zan, U. Bangert, Q. Ramasse and K. S. Novoselov, Journal of Microscopy, 2011, 244, 152-158.
20. F. Varchon, R. Feng, J. Hass, X. Li, B. N. Nguyen, C. Naud, P. Mallet, J. Y. Veuillen, C. Berger, E. H. Conrad and L. Magaud, Physical Review Letters, 2007, 99, 126805.
21. G. Giovannetti, P. A. Khomyakov, G. Brocks, V. M. Karpan, J. van den Brink and P. J. Kelly, Physical Review Letters, 2008, 101, 026803.
22. J. Wintterlin and M. L. Bocquet, Surface Science, 2009, 603, 1841-1852.
23. R. F. Egerton, P. Li and M. Malac, Micron, 2004, 35, 399-409.
24. J. H. Warner, M. H. Rummeli, L. Ge, T. Gemming, B. Montanari, N. M. Harrison, B. Buchner and G. A. D. Briggs, Nat Nano, 2009, 4, 500-504.
25. I. Horcas, R. Fernandez, J. M. Gomez-Rodriguez, J. Colchero, J. Gomez-Herrero and A. M. Baro, Review of Scientific Instruments, 2007, 78, 013705-013708.
26. R. E. Peierls, Ann. Inst. Henri Poincare 1935, 5, 177-222.
27. L. D. Landau, Phys. Z. Sowjetunion, 1937, 11, 26-35.
28. A. Fasolino, J. H. Los and M. I. Katsnelson, Nat Mater, 2007, 6, 858-861.
29. T. J. Booth, P. Blake, R. R. Nair, D. Jiang, E. W. Hill, U. Bangert, A. Bleloch, M. Gass, K. S. Novoselov, M. I. Katsnelson and A. K. Geim, Nano Letters, 2008, 8, 2442-2446.
30. U. Bangert, M. H. Gass, A. L. Bleloch, R. R. Nair and J. Eccles, physica status solidi (a), 2009, 206, 2115-2119.
31. B. Hamilton, J, Jacobs and M. Missous, Jnl. Phys C. Condensed Matter, 2003, 15, S3083-S3093.
32. P. Xu, Y. Yang, S. D. Barber, M. L. Ackerman, J. K. Schoelz, I. A. Kornev, S. Barraza-Lopez, L. Bellaiche, and P. M. Thibado, Physical Review B, 2011, 84, 161409.

5.5 Conclusion

Suspended graphene has been studied in the STM for the first time. Atomically resolved single layer graphene images were obtained upon establishing annealing conditions that help to minimize surface contamination on the graphene. These annealing and imaging conditions can be employed to investigate metal-graphene systems along with spectroscopic measurements. Exploring metal onsuspended graphene in the STM are expected to provide new experimental insight into fundamental properties of these systems, through elimination of substrate and impurity effects and in-situ observations. Our first investigations showed microscopic corrugations, ripples, in the suspended graphene, which are comparable with TEM observations regarding their amplitude and wavelength. The ripples were also seen to be stable for the entire measurement period. So this static appearance indicates the ripples might be an intrinsic feature of suspended graphene.

Chapter 6

Metal Behaviours on Graphene

6.1 Introduction

Any electronic device irrespective of whether macro or nano sized has metal contacts to connect it to external device components. Thus, metal behaviour on material surfaces is an intriguing and important subject of study. The interfacing of graphene with metal contacts is a recurring theme for graphene based devices. This area of graphene research is still ripening and the consequences of particular dopants on graphene's electronic properties are still being investigated. Understanding of metal-graphene interaction on a fundamental level is of significance to the improvement of graphene based devices. In order to advance the device performance distribution, bonding, doping and stability of metals on the graphene surface needs to be understood. However, the metal-graphene interactions have been studied predominantly by means of DFT calculations so far and the experimental exploration of metal-graphene systems is limited, for example, there are only few TEM based studies on these systems. DFT calculations have emerged which present predictions of binding energies, adsorption sites relative to the hexagon, doping and relaxed structures of various metal ad-atoms and clusters on pristine and defected graphene structures. Therefore detailed experimental TEM observations of metal ad-atoms and their clusters on single- and few-layer graphene are desirable. Here metal-graphene interactions are studied for various metals on pristine and modified graphene. Different metal behaviours in terms of distributions, e.g, as individual ad-atoms and clusters, are observed on the graphene layers.

Initial investigations of metal atoms on pristine graphene revealed that none of the metals studied reacted with the clean (residue free) graphene surfaces but metals tend to cluster on the hydrocarbon contaminations. Thus to be able to amend this behaviour researchers proposed to attach hydrogen to carbon atoms in the graphene lattice. Hydrogen ad-atoms can trap small molecules to specific sites on the graphene surface and these molecules remain stable at room temperature [129]. This suggestion stimulated attempts of experimental proof; all results are presented in the attached publications. We found that as a result of the hydrogenation, the metal behaviour changed.

6.2 Sample Preparation

Graphene flakes used for the experiments were prepared by mechanical cleavage and CVD techniques. The graphene layers were then transferred to the TEM grids as detailed in Chapter 3. As well as pristine graphene, modified graphene in our case hydrogenation and fluorination was used. Hydrogenation of the samples was performed by exposing suspended membranes to a cold hydrogen plasma which consisted of a mixture of hydrogen and argon gases (10% H_2) at low-pressure (0.1 mbar). Plasma treatment was performed for different lengths of time; the samples used in the experiments shown here were hydrogenated for 1.5 hours. Using suspended graphene flakes on the TEM grids enabled atomic hydrogen to be absorbed on both side of the graphene surfaces.

Metal deposition has been performed on the suspended flakes, on the TEM grids, via electron-beam and thermal evaporation of Au and Cr to an amount of ~2Å, and Fe was found as a contaminant. Then different amounts of Au were evaporated onto the graphene surface to investigate gold nanostructure evolution. Both types of single layer graphene samples, exfoliated and CVD-grown, were investigated and compared upon metal deposition; almost no difference was seen in terms of metal behaviours. We continued the investigations mainly with CVD-grown graphene samples as it is easier to obtain larger flakes and to transfer and locate them on the grid. Metal evaporation has been also done for graphene layers that were on a SiO_2/Si substrate to find out whether the substrate can affect the metal behaviour. Their transfer to the grids for TEM studies was performed afterwards, however, no meaningful difference has been observed as both, suspended and supported graphene, exhibited the same tendency of the clean graphene regions, namely not to react with metal atoms.

Initially graphene regions were identified in a Tecnai F-30 ahead of metal deposition in terms of layer number, cleanliness and location of the graphene flakes. Again initial investigations including high resolution studies were carried out after metal deposition in a Tecnai at 300kV before HAADF-SuperSTEM investigations at 60kV.

Thickness of the metal layers on the graphene surfaces whether they are in 2D or 3D form, in particular in case of gold, was determined by intensity profiles.

6.3 Results and Discussion

The results of this project were published in Nano Letters and Small in 2011. In order to best present our work, the original manuscripts **"Metal-Graphene Interaction Studied**

Via Atomic Resolution Scanning Transmission Electron Microscopy" *(Nano Letters, 2011, 11(3), p.1087-1092)* and **"Evolution of Gold Nanostructures on Graphene"** *(Small, 2011, 7(20), p.2868-2872)* are presented below.

Metal-Graphene Interaction Studied Via Atomic Resolution Scanning Transmission Electron Microscopy

Recep Zan, Ursel Bangert, Quentin Ramasse and Konstantin S. Novoselov

Nano Letters, 2011, 11(3), p.1087-1092

ABSTRACT

Distributions and atomic sites of transition metals and gold on suspended graphene were investigated via high resolution scanning transmission electron microscopy, especially using atomic resolution high angle dark field imaging. All metals, albeit as singular atoms or atom aggregates, reside in the omni-present hydro-carbon surface contamination; they do not form continuous films, but clusters or nano-crystals. No interaction was found between Au-atoms and clean single-layer graphene surfaces, i.e., no Au-atoms are retained on such surfaces. Au- and also Fe-atoms do, however, bond to clean few-layer graphene surfaces, where they assume T- and B-sites, respectively. Cr-atoms were found to interact more strongly with clean mono-layer graphene, they are possibly incorporated at graphene lattice imperfections, and have been observed to catalyse dissociation of C-C bonds. This behaviour might explain the observed high frequency of Cr-cluster nucleation, and the usefulness as wetting layer, for depositing electrical contacts on graphene.

TOC

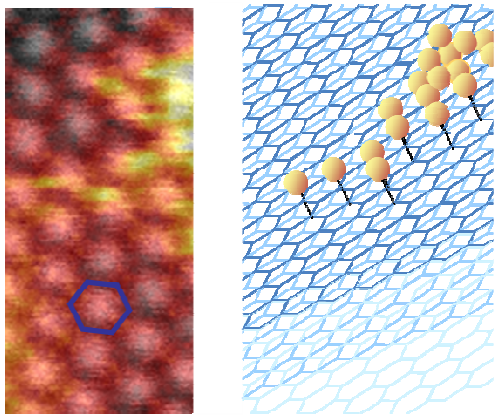

Graphene, just one atom layer thick, has spurred a flurry of investigations into its structural properties, morphology and chemistry.[1, 2] One of the fields of study concerns the interaction between metal and graphene. Our knowledge about this interaction to date is mainly based on theoretical calculations, many of these based on Density Functional Theory (DFT). However, experimental exploration of the metal-graphene systems is still limited; especially transmission electron microscopy (TEM) observations are practically non-existent. Such observation would be of great interest to prove predicted positions of metal atoms in the hexagonal graphene structure. This is of importance not least in gaining an understanding of, e.g., the influence of metal contacts on macroscopic electrical transport.

Positions of foreign atoms on graphene have been calculated for a wide range of metals. H-sites (center of the hexagon) are predicted mainly for alkaline metals, such as K, Na, Cs and Ti, Fe; T-sites (top of carbon atom) for Au, Cu, Ni, Sn and F, whereas Pt, Cr, Cl, S, O, N and P are expected to bind strongly to B sites, i.e., on top of a carbon-carbon bond (bridge site) as schematically shown in fig. 2.[3, 4] The two common approximation for DFT calculations, local density approximation and generalized gradient approximation – the latter does not represent Van-der-Waals forces very well[5]-, lead to different binding energies and thereby to different sites for Au atoms, T-sites for the former and B-sites for the latter method.[6] In addition, arbitrary variables used in the calculation, such as cut-off energy[7] and size of the supercell[8] can affect the result of DFT calculations. It was furthermore found, theoretically and experimentally, that point defects (carbon vacancies) in graphene provide nucleation sites and even further substitutional incorporation of metals.[4, 9-13]

Contrarily to high resolution phase contrast imaging (HREM) in a transmission electron microscope, due to the approximate Z^2-sensitivity dependency of high angle annular dark field (HAADF) image contrast[14], sites of singular metal atoms on graphene can directly be revealed. Because of the extremely bright (~100pA), highly focussed (1Å) electron probe, dedicated scanning transmission electron microscopes with cold field emission guns and probe corrector (AC STEMs) are prime tools to achieve this; but there are very few of these in existence worldwide, and HAADF studies of graphene are practically non-existent. Here we present a study of atomic sites of metal atoms on suspended, single and few-layer graphene, primarily using atomic resolution HAADF imaging in an AC STEM.

Two different techniques for the preparation of suspended graphene membranes were used, micromechanical cleavage and lift-off of CVD films grown on Ni- and Cu-substrates.[15-17] Au- and Cr- atoms were deliberately introduced by either thermal or e-beam evaporation at thicknesses of 0.2 and 5 Å. Fe-atoms have been identified as residual impurities, presumably originating from acid treatment (Ferric Chloride).

Additionally to identifying the graphene layer number via the plasmon energy[18] we have simulated HAADF and bright field (BF) STEM images of pristine mono-, bi-, tri- up to 8-layer graphene using Kirkland's HREM simulation software[19]. Further to HAADF analysis all atom species were identified by ultra-high spatially resolved electron energy loss spectroscopy (EELS).

Metal atom deposition can be affected by many factors, such as the substrate[20, 21], which the graphene is placed upon, the temperature during the deposition as well as the deposition rate, all resulting in different surface morphologies[22] and transport properties.[23] Extensive HAADF investigations in combination with electron energy loss spectroscopy (EELS)[24], in which we have scrutinised many clean single-layer graphene patches for foreign atoms, never revealed impurity atoms with Z≥9 attached to single layer graphene sheets. However, we observed many types of impurities within the hydrocarbon contamination on single and multiple sheets, and we did also observe impurity atoms on clean areas in multi-layer graphene. It was found previously that an energetically favourable path for all metal atoms is to form clusters[11], either at contamination sites and defects (in the case of single layers) or directly on the clean graphene surface of few-layer membranes.

First-principle calculations of ***gold*** atoms and dimers on graphene surfaces show that the gold–gold interaction is significantly stronger than the gold–graphene interaction[6] (for this reason gold is highly mobile on graphene), as is experimentally confirmed by Gan et al.[10] with observation of gold clusters –rather than atoms- on the graphene sheet. For a single gold atom the favourable energy configuration is found to be directly above a carbon atom on graphene sheet. An interesting result for the Au doping mechanism from DFT calculations, proposed by Pinto et al.[25] is that Au does not dope single layers, however it dopes bilayer graphene. We note that the following images are representative of a vast number of images obtained from many samples. We especially want to emphasize that the graphene surface seen as background in fig.1a) has a similar appearance in all graphene samples ever obtained by us, albeit via micromechanical exfoliation, from CVD grown samples, after cleaning in solvents or after plasma treatment: nm-size pristine graphene

patches, constituting overall less then ~30% of the total surface, are surrounded by hydro-carbon based deposits. The latter are more or less mobile under the electron beam depending on their thickness.

We found that gold atoms form nano-crystalline clusters on graphene as shown in fig 1a), and the gold cluster size increases with increasing evaporated Au-amount. These clusters form exclusively on hydrocarbon contamination, revealed by greyish contrast in HAADF images (fig. 1b) or structural irregularities, e.g., defect sites, but never on clean graphene; we have never observed singular Au-atoms. This demonstrates the extreme mobility of gold on pure graphene, suggesting that the interaction between graphene and gold is weak, similar to observations by Charlier et al., of Au-doped carbon nanotubes.[9]

Figure 2a) shows an area in atomic resolution, where a monolayer of gold has formed on graphene (bottom left corner). The HAADF image in fig. 2b), by the dark greyish surround of this gold-atom raft, reveals that even this monolayer sits amidst hydrocarbon contamination. We did, however, observe individual Au atoms on clean few-layer graphene patches. It thus appears that atoms in sub-surface layers are needed to contribute to the bonding with surface gold atoms in order to prohibit dissociation and diffusion. Figure 2c) is a high resolution BF STEM phase contrast image of few-layer graphene. The electron beam is focussed on the exit surface of the sample, on which the gold is evaporated, hence proceeds through the graphene layers before it encounters the gold atoms. The aggregate of gold atoms, seen in the HAADF image in fig. 2d) is so thin, that it is invisible and not interpretable in phase contrast. However, the BF image

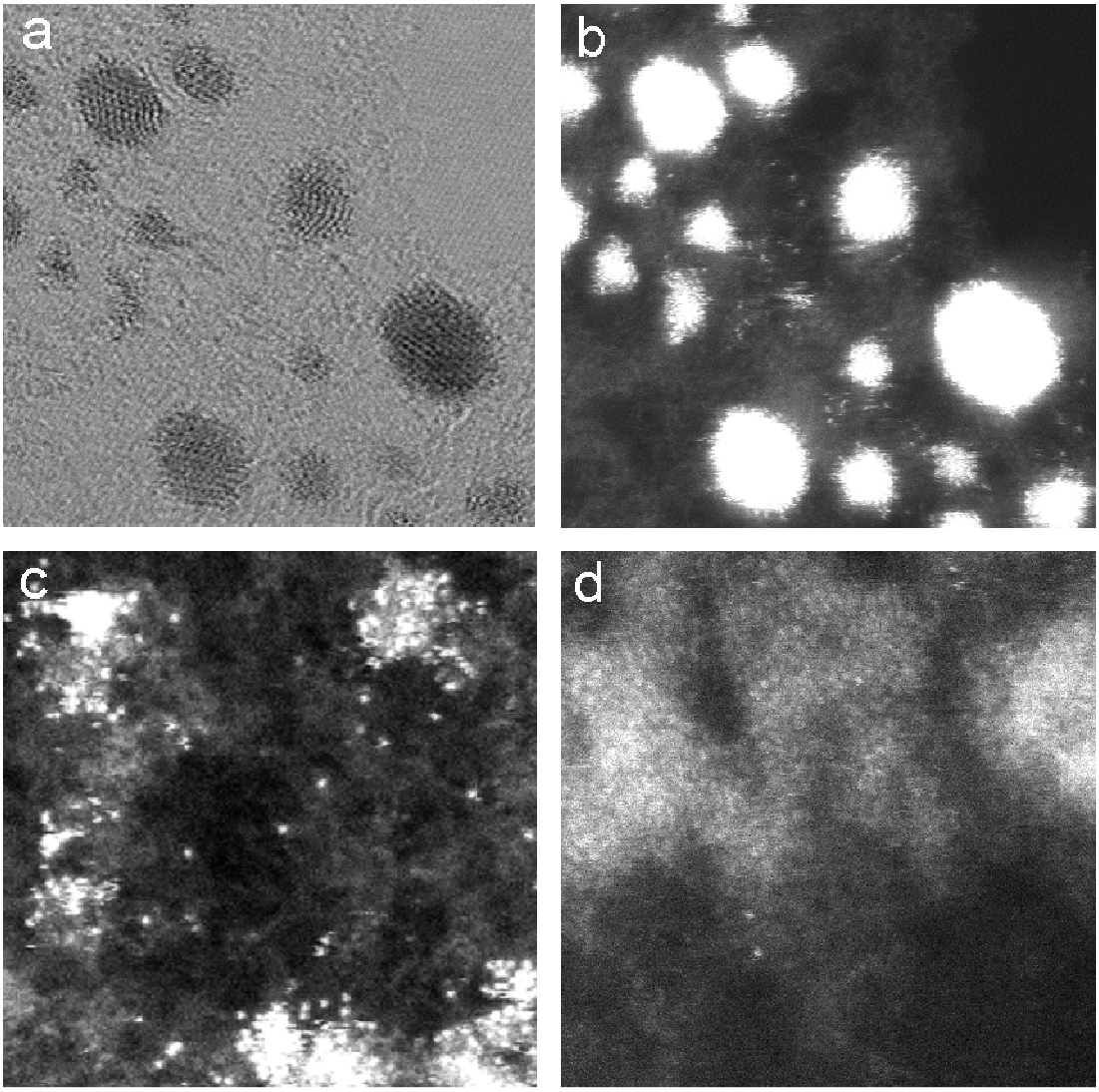

Figure 1. a) BF and b) HAADF image of mono-layer graphene regions with 0.2 Å of Au evaporated on top. Au nano-crystals are clearly visible in both images, the HAADF image furthermore reveals single Au-atoms. Hydrocarbon contamination is manifest as 'worm-like' background in the BF and as dark-grey 'cloud-like' contrast in the HAADF image; c) HAADF image of Fe-atoms on mono-layer graphene. Note again the hydrocarbon deposit, which hosts the atoms; d) HAADF image of a mono-layer graphene region with 0.2 Å Cr evaporated on top. Cr-atoms are spread over wide areas in non-crystalline agglomerates predominantly amidst hydrocarbon deposits. The frame width in all images is 10 nm.

exhibits strong contrast and relatively little noise and shows the lattice periodicities well, so can be used as guide to identify positions in the corresponding, simultaneously acquired HAADF image (fig. 2d), which has inherently much lower intensity. Here the graphene atomic lattice is barely recognisable, but the gold atoms are clearly visible. They have

formed a loose aggregate with single atoms in their vicinity, some of which have been numbered. In order to locate the benzene rings we have carried out BF- and HAADF-STEM image simulations for few-layer graphene (with 3 layer simulations at -50 Å defocus giving the best match). These are shown as insets in 2c) and d). We note that the benzene ring centres of the top layer correspond to bright patches in the BF image (c) and are dark in the HAADF image (d). The model structure (red benzene rings) is overlaid in identical locations on the simulations as well as on the experimental BF and HAADF image (in the bottom left corners). Hence C-atoms –the hexagon corners- constitute bright contrast in HAADF images, and –under the current focusing conditions- dark contrast in BF images. Comparing locations of gold atoms spotted in the HAADF image (circled) with identical positions in the BF image, the sites can be identified as T-sites. This is in agreement with theoretical predictions.

Iron-atoms have not been deliberately deposited in our study, but reside as impurities on many samples, presumably as a result of chemical processing. The HAADF image in figure 1c) shows that as in the previous case, on uncontaminated single layer areas (black patches) the sticking probability is very small: all Fe clusters and single atoms (white spots) are located on top of or at the edges of hydrocarbon contamination (greyish areas). On the surfaces of multi-layer graphene on the other hand individual Fe-atoms can be seen. Figure 3a), shows a low-pass filtered atomic resolution HAADF image (noise reduced) of 2 and 3 staggered graphene sheets, using Fourier filtering provided in the Gatan imaging software. Fe-atoms are clearly visible as white spots.

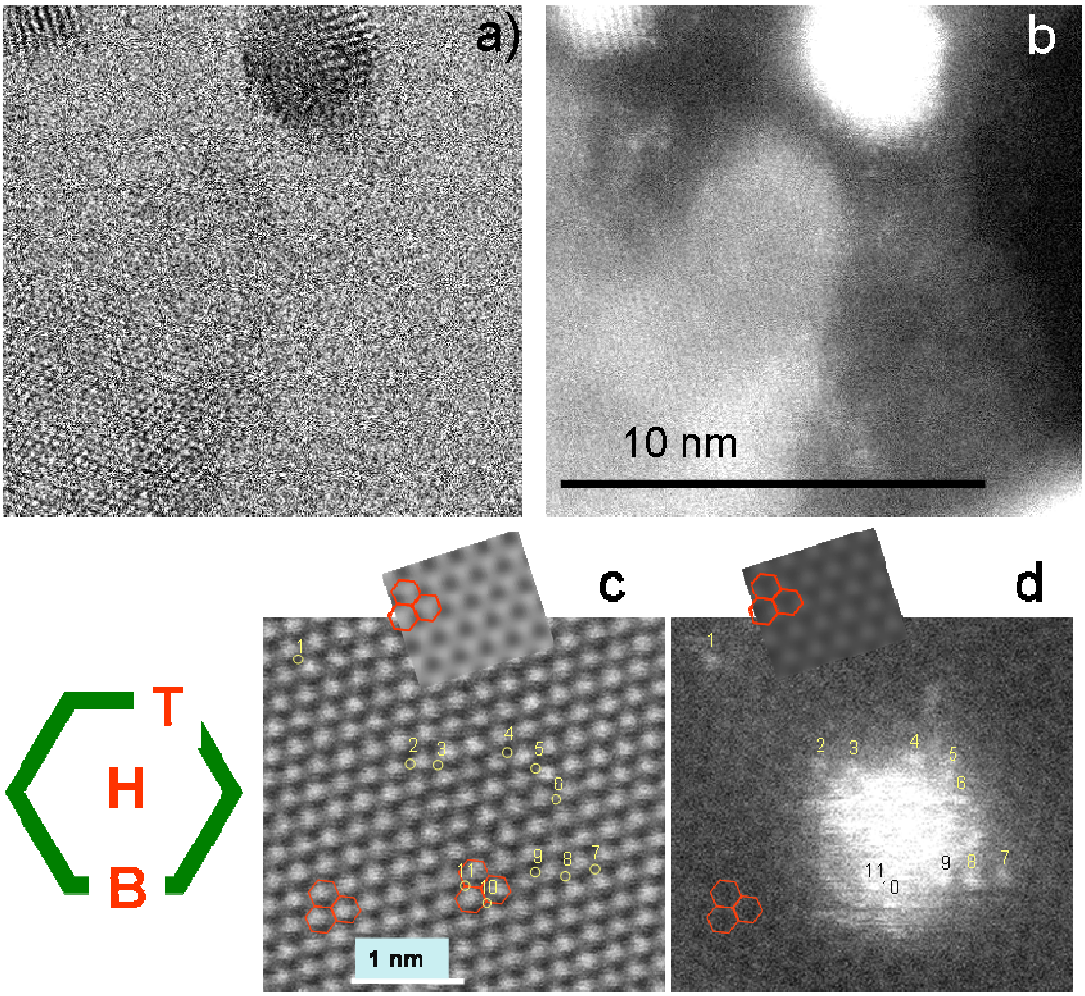

Figure 2. (a) BF STEM image of 0.2 Å gold evaporated on graphene, showing a mono-layer gold-atom raft in the left bottom corner and a gold nano-crystal at the top; (b) corresponding HAADF image; (c) atomic resolution BF and (d) corresponding HAADF STEM image depicting a few-layer patch in graphene evaporated with 5 Å of gold. In (d) individual gold atoms can be seen separated from the small cluster in the middle. Benzene rings are overlaid in red in both images, showing that bright contrast in the BF image corresponds to dark contrast in the centres of the top-layer benzene rings in the HAADF image, as derived from simulations of 3-layer graphene (at -50 Å defocus), shown in the insets in (c) and (d). Single atoms are marked with numbers 1-11 just above the atoms in the HAADF image; identical places are marked by yellow circles in the BF image, identifying them to be T-sites. The images represent raw, unfiltered data. Shown on the left of (c) is a schematic with metal sites on the benzene ring.

The EEL spectrum in the inset is taken on an individual Fe-atom, showing the characteristic $L_{2,3}$ absorption edge of Fe at ~708 eV. In the left and right hand panels of

fig.3a) the areas around Fe-atoms on 3-layer and 2-layer graphene, respectively, are enlarged with a model of the AB-stacked graphene lattice overlaid, the exact position of which was confirmed from simulated HAADF images (shown as insets). It becomes clear that the Fe-atoms in both cases sit on B-sites, in contradiction to calculations, which predict H-sites.

Chromium, similar to gold and iron, was found at large on hydrocarbon deposits (fig. 1d). Cr was evaporated to the same 0.2 Å layer thickness as Au, however, the fractional coverage was larger (fig. 1d); this indicates that the Cr-clusters are flatter or less dense than the Au clusters (e.g., compare figs 1b and d). Notably there does not appear to be a high degree of crystallinity in the Cr-deposits, suggesting that the Cr –in contrast to the Au-deposits in molecular form, possibly partially as Cr-oxide; indeed EEL spectrum images have proven that high Cr levels coincide with oxygen signals. Interestingly with Cr, singular atoms do appear in some images on mono-layer graphene. These atoms stay in place over several image scans. Figure 3b) shows an HAADF image of a Cr-atom on a clean mono-layer graphene patch. By overlaying the structural model, we identify the Cr position as a B-site, as predicted from DFT models. After several scans the Cr-atom has disappeared, leaving two vacancies behind (fig.3c). Hence Cr is more reactive with graphene than Au. Considering the relative stability of the Cr-atom and the double vacancy after its disappearance, we cannot exclude the possibility that the Cr-atom, rather than assuming a B-site, was indeed incorporated to substitute two C-atoms in the graphene sheet. Figure 3b) shows the edge of a hole in the graphene layer on the top right. The hole has become larger after repeated scanning in fig. 3c). From observations of many image scans in different areas we can derive a possible mechanism for the hole formation: Cr-atoms are frequently seen to decorate the edges of graphene layers (see bottom hole the HAADF image in figure 3d). The figure furthermore shows that Cr-atoms (dotted chain indicated by top arrow) migrate from larger clusters (white contrast in top right corner) to the edge of the (top) hole. When the Cr atoms dissociate during repeat scans, i.e., have vanished from the images, the holes have enlarged. This is a strong indication for Cr-mediated C-C dissociation and vacancy formation.

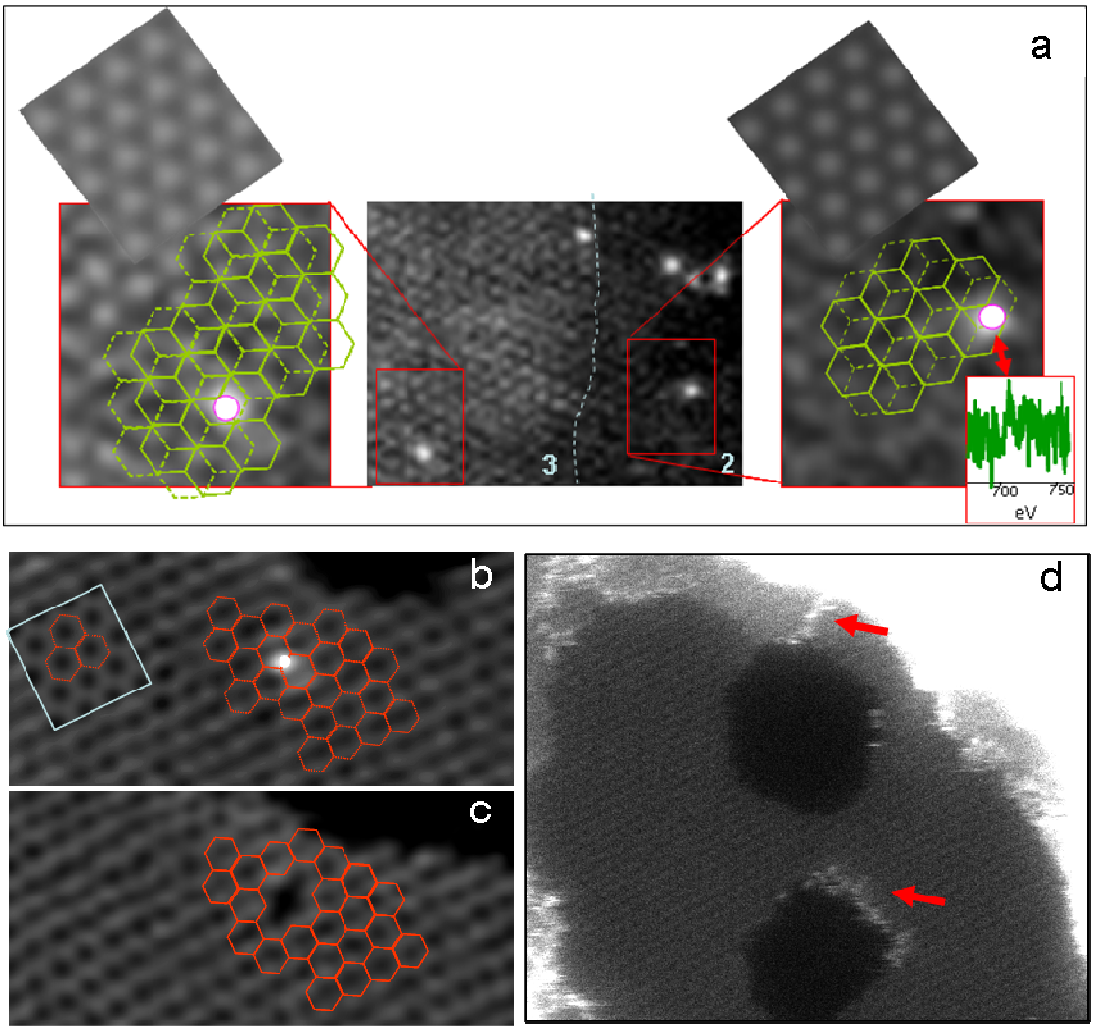

Figure 3. (a) Middle panel: noise reduced HAADF lattice image of 2- and 3-layer graphene with Fe-impurities (the blue line shows the approximate position of the sheet edge). The left- and right-hand panel are enlarged views of the red frames, with overlaid model structures (solid lines indicate the surface layer) to clarify the position of the Fe-atoms; these sit on the surface on B-sites. Shown in the insets are HAADF simulations of 3 layers (left) and 2 layers (right). The spectrum-inset shows the Fe-L2,3 absorption edge obtained on the single, arrowed atom; (b) noise-filtered HAADF image of a Cr-atom on mono-layer graphene; the HAADF image simulation is shown in the inset; (c) same area as in (b) after repeat scanning, revealing a di-vacancy, where the Cr-atom had been. Model structures are overlaid to show the sites of the defects; d) raw HAADF image of mono-layer graphene patch (dark grey) bordered by hydrocarbons (lighter grey). Cr-atoms sit on the hydrocarbon contamination; a chain of Cr-atoms (arrowed; top) can be seen moving from an area of Cr-clusters (white patch in the top right corner: the image is overexposed here due to the high Cr-concentration) towards the edge of the top hole (black area), and to decorate the edge of the bottom hole (arrowed; bottom).

We want to note here that in order to achieve improved 'sticking' and incorporation of metals in graphene we also introduced atoms (e.g., ***cobalt***) via low energy ion-implantation at 200 eV to a density of typically 1 atom nm^{-2}. The results were very similar to those of the Fe-impurities on graphene with all observed Co sitting on hydrocarbons. It was, however, not one possible to identify atomic Co-sites within/on top of the graphene sheet; not one single Co-atom could be detected in clean graphene areas (results not shown here).

In conclusion, investigation of transition metals and gold on graphene showed that clean single-layer graphene surfaces do not retain any significant amount of atoms of these species (notably none in the case of gold). All metals, albeit as singular atoms or clusters thereof reside in the abundant hydro-carbon surface contamination. This behavior might have consequences for macroscopic electrical transport properties in graphene. Although electrical transport measurements are usually obtained from graphene supported by substrates, the graphene membrane even in this case is still a 2-D object. Because contamination appears to be an issue with 2-D structures, it is very likely that charge transfer from mono-layer graphene into metal contacts proceeds in the largest part across a macromolecular layer (hydrocarbons). Individual Au and Fe atoms could be observed, however, on clean few-layer graphene surfaces and found to reside on top of carbon atoms, and on top of C-C bonds, respectively. Chromium appears to bond more strongly to mono-layer graphene and has been observed to catalyse dissociation of C-C bonds. Bonding of singular Cr-atoms to graphene, possibly via lattice defects, could be a precursor for the high frequency nucleation of Cr-clusters, which, in contrast to Au, provide more continuous contact throughout the membrane, and hence the importance of role of a Cr-'wetting layer' between Au and graphene in forming electrical contacts on graphene, which is commonly used in electrical transport studies, can be understood.

REFERENCES AND NOTES

1. Novoselov, K. S.; Geim, A. K.; Morozov, S. V.; Jiang, D.; Zhang, Y.; Dubonos, S. V.; Grigorieva, I. V.; Firsov, A. A. *Science* **2004,** 306, (5696), 666-669.
2. Geim, A. K.; Novoselov, K. S. *Nat Mater* **2007,** 6, (3), 183-191.
3. Chan, K. T.; Neaton, J. B.; Cohen, M. L. *Physical Review B* **2008,** 77, (23), 235430.
4. Boukhvalov, D. W.; Katsnelson, M. I. *Applied Physics Letters* **2009,** 95, (2), 023109.
5. Leenaerts, O.; Partoens, B.; Peeters, F. M. *Physical Review B* **2008,** 77, (12), 125416.
6. Akturk, U., Olcay; Tomak, M. *Physical Review B* **2009,** 80, (8), 085417.
7. Varns, R.; Strange, P. *Journal of Physics: Condensed Matter* **2008,** 20, (22), 225005.

8. Leenaerts, O.; Partoens, B.; Peeters, F. M. *Microelectronics Journal* **2009,** 40, (4-5), 860-862.
9. Charlier, J. C.; et al. *Nanotechnology* **2009,** 20, (37), 375501.
10. Gan, Y.; Sun, L.; Banhart, F. *Small* **2008,** 4, (5), 587-591.
11. Krasheninnikov, A. V.; Lehtinen, P. O.; Foster, A. S.; Pyykk; ouml; P.; Nieminen, R. M. *Physical Review Letters* **2009,** 102, (12), 126807.
12. Zhou, Y. G.; Zu, X. T.; Gao, F.; Lv, H. F.; Xiao, H. Y. *Applied Physics Letters* **2009,** 95, (12), 123119-3.
13. Okamoto, Y. *Chemical Physics Letters* **2006,** 420, (4-6), 382-386.
14. Wang, Z. L.; Cowley, J. M. *Ultramicroscopy* **1989,** 31, (4), 437-453.
15. Li, X.; Cai, W.; An, J.; Kim, S.; Nah, J.; Yang, D.; Piner, R.; Velamakanni, A.; Jung, I.; Tutuc, E.; Banerjee, S. K.; Colombo, L.; Ruoff, R. S. *Science* **2009,** 324, (5932), 1312-1314.
16. Kim, K. S.; Zhao, Y.; Jang, H.; Lee, S. Y.; Kim, J. M.; Kim, K. S.; Ahn, J.-H.; Kim, P.; Choi, J.-Y.; Hong, B. H. *Nature* **2009,** 457, (7230), 706-710.
17. Reina, A.; Jia, X.; Ho, J.; Nezich, D.; Son, H.; Bulovic, V.; Dresselhaus, M. S.; Kong, J. *Nano Letters* **2008,** 9, (1), 30-35.
18. Eberlein, T.; Bangert, U.; Nair, R. R.; Jones, R.; Gass, M.; Bleloch, A. L.; Novoselov, K. S.; Geim, A.; Briddon, P. R. *Physical Review B* **2008,** 77, (23), 233406.
19. Kirkland, E. J., *Advanced Computing in Electron Microscopy*. 1. ed.; Plenum Press: 1998.
20. Zhou, Z.; Gao, F.; Goodman, D. W. *Surface Science* **2010,** 604, (13-14), L31-L38.
21. Alpha, T. N. D.; et al. *New Journal of Physics* **2009,** 11, (10), 103045.
22. Sicot, M.; Bouvron, S.; Zander, O.; Rudiger, U.; Dedkov, Y. S.; Fonin, M. *Applied Physics Letters* **2010,** 96, (9), 093115-3.
23. McCreary, K. M.; Pi, K.; Swartz, A. G.; Han, W.; Bao, W.; Lau, C. N.; Guinea, F.; Katsnelson, M. I.; Kawakami, R. K. *Physical Review B* **2010,** 81, (11), 115453.
24. Bangert, U.; Bleloch, A.; Gass, M. H.; Seepujak, A.; van den Berg, J. *Physical Review B* **2010,** 81, (24), 245423.
25. Pinto, H.; Jones, R.; Goss, J. P.; Briddon, P. R. *physica status solidi (a)* **2010,** 207, (9), 2131-2136.

SUPPORTING INFORMATION

Sample preparation

In this study we employ two different techniques for the preparation of graphene membrane, which are micromechanical cleavage process and growth on different substrates (Ni and Cu) with CVD method as reported previously.[15-17] Firstly we started with transferring of graphene from different substrates to TEM grid. This was followed by identification the number of layers of graphene and distinguish single layer from few layer graphene through selected area diffraction pattern by comparing first and second ring spots intensities.[26, 27] After having obtained clean graphene membranes, Au and Cr atoms have been deliberately introduced into the graphene sheet by using either thermal or e-beam evaporation at different deposition rates, giving nominal Au-layer thicknesses of 0.2 and 5 Å for monolayer and few-layer graphene, respectively. None of the evaporation conditions resulted in uniform coverage of the graphene flakes. Behavior and positions of individual gold atoms on graphene were investigated via high resolution HAADF and BF electron microscopy. HAADF can reveal the atomic nature of species at single-atom level through the approximate Z^2-dependence of the scattering probability. It is thus feasible for detection of atom species on/in graphene of Z equal to and larger than carbon.[28-31] Gold atoms due to their high atomic number (Z_{Au}:79) compared to the carbon (Z_C:6) are identified easily, yielding a contrast ratio of ~6241:36.

We note that metal atoms are extremely mobile under the scanning electron beam; in some cases they were dissociated from the graphene during the scan, which became obvious by bright streaks in the HAADF images. In examples we present here, despite undergoing vibrations, the atoms relax back to their original positions. This is evidenced by the fact that they can actually be imaged, i.e., appear as distinct, localized Å-size bright patches.

Co-ion implantation was carried out in the University of Salford low-energy ion implanter at an energy of 200 eV and areal ion densities of 10^{14} and 10^{15} cm^{-2}.

EM tools and evaluations

The structural and topographic properties of doped-graphene (mono and few-layer) have been studied by using conventional transmission electron microscopy (TEM) using a

Tecnai F-30 at 300 keV at the Materials Science Centre of the University of Manchester and the AC corrected scanning transmission electron microscopes (SuperSTEMs at CCLRC Daresbury) at 60 and 80 keV.

We mostly used raw images in this paper, however, in order to reduce noise in the HAADF images, Fourier Filtering was carried out in some instances, using the Digital Micrograph routines. In all these cases either a Gaussian convolution function or a smooth-edge circular mask including all visible diffraction spots was used.

Electron energy loss spectroscopy was carried out with a UHV Enfina EEL spectrometer in all cases to verify the nature of the elements present. Point spectroscopy or spectrum imaging[24] were used, the latter to obtain spatial distribution map of elements. Au was monitored using the characteristic plasmon structure as well as the O- and N-absorption edges and Fe, Cr and Co using the $L_{2,3}$ absorption edges. Contaminants, such as Si and O were also monitored.

Layer numbers were obtained from relative HAADF intensities of the layers calibrated to the vacuum intensity as well as from π-plasmon energy and shape.[18]

Image simulation

At the same time to support our experimental result we have simulated HRTEM images of pristine mono- and bi-layer graphene as well as Au-contaminated mono- and bi-layer graphene for different defocus by using TEMSIM Kirkland's HRTEM simulation software.[19]

Figure S1 shows a typical overview HAADF image of 0.2 Å gold evaporated on monolayer graphene. As can easily be recognized, gold atoms are not dispersed over the graphene surface form clusters (bright) on the contamination (dark grey). Also visible is pristine graphene (black), constituting typically ~30% and maximally up to 50% of the surface.

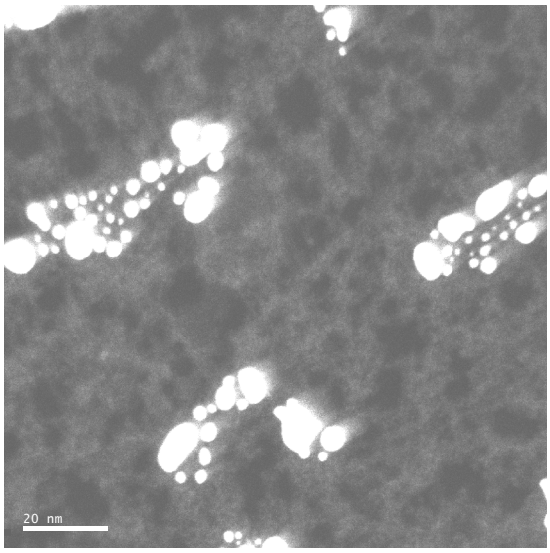

Figure S1. HAADF STEM image of 0.2 Å gold evaporated on monolayer graphene

Figure S2 shows whole BF and HAADF images, a section of which is presented in the main text in Figs.2 a) and b).

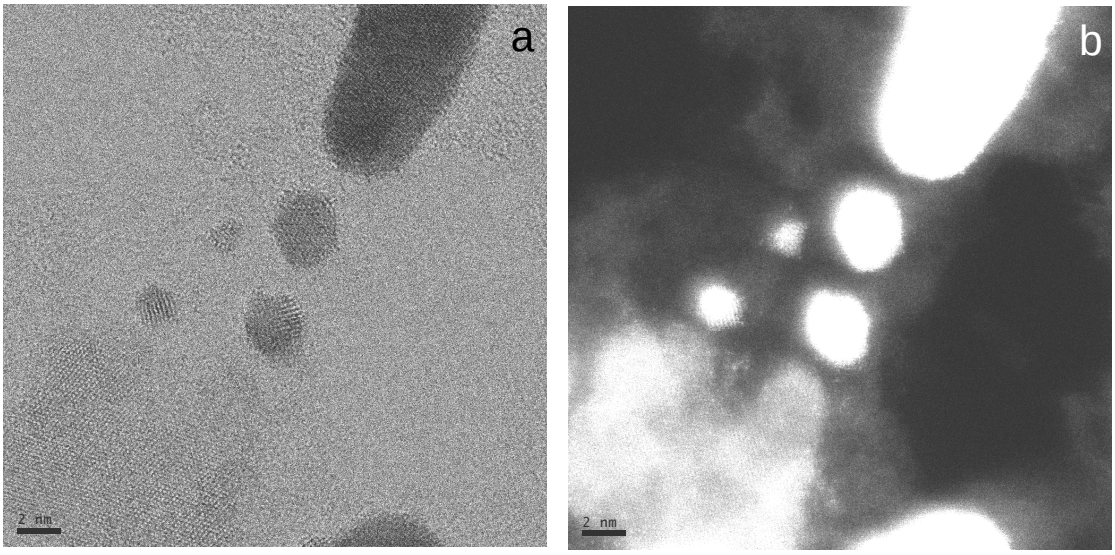

Figure S2. (a) BF STEM image of 0.2 Å gold evaporated graphene, (b) corresponding HAADF image

HAADF images of 0.2 Å Cr evaporated on mono-layer graphene are presented with different brightness in Figure S3. Figure S3a) shows that the Cr clusters are not crystalline. When the image brightness is increased the Cr-clusters can be seen surrounded by surface contaminants. Pristine graphene patches are very small in size, the cleanest (darkest part) is in the middle of Figure S3b).

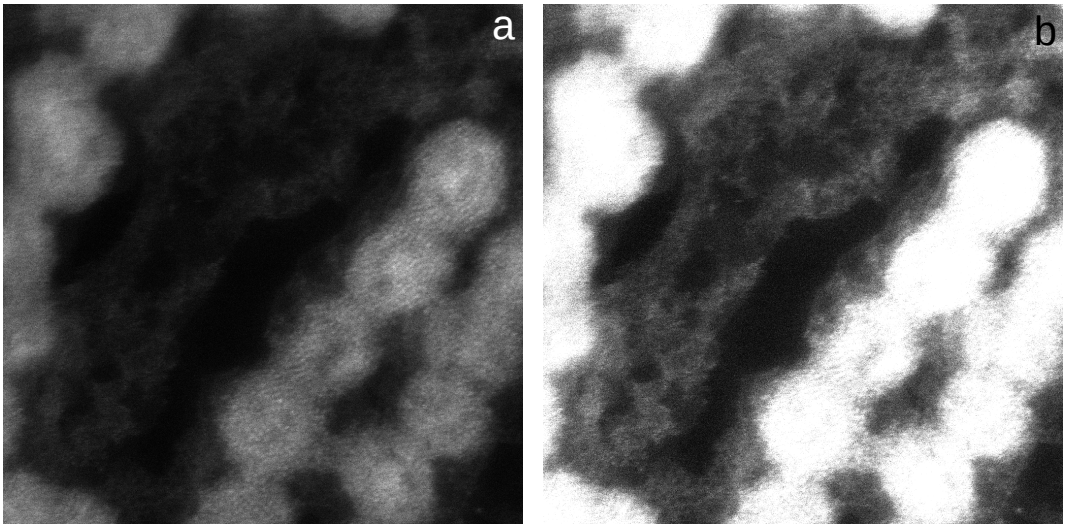

Figure S3. (a) HAADF images of a Cr-atom on mono-layer graphene; (b) same area as in (a) with different brightness.

The sequence of HAADF images in figure S4 is of the same area showing Cr-atoms on mono-layer graphene (the lattice of the latter is just visible). In Figure S4a) one Cr atom can be seen on pristine graphene, and a few Cr atoms are decorating the edges of a hole in graphene. After a few scan the Cr atoms at the edge of hole have disappeared as shown in fig. 4Sb). After many more scan on the same area the single Cr atom has also disappeared leaving a double vacancy behind. The hole is getting larger, too (fig. S4c). Enlarged sections of fig. S4 b) and c) are used in the main text in fig. 3a) and b).

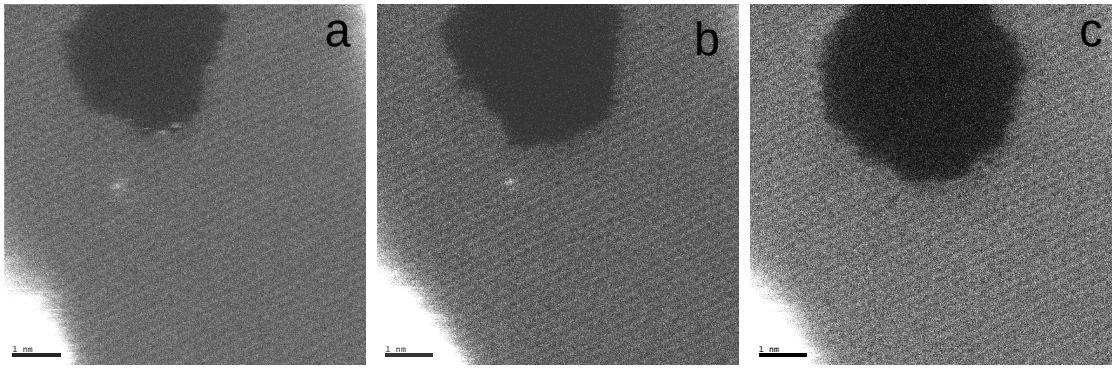

Figure S4. (a) HAADF images of a Cr-atom on mono-layer graphene; (b) same area as in (a) after few scans, Cr atoms having decorated the edge of hole have gone; (c) same area as in (a) and (b) after many scans; the Cr atom remote from the hole has disappeared, too, and left a vacancy-dimer behind. This suggests that the Cr atom was integrated in the graphene lattice.

REFERENCES

(1) Li, X.; Cai, W.; An, J.; Kim, S.; Nah, J.; Yang, D.; Piner, R.; Velamakanni, A.; Jung, I.; Tutuc, E.; Banerjee, S. K.; Colombo, L.; Ruoff, R. S. *Science* **2009,** 324, 1312-1314.

(2) Kim, K. S.; Zhao, Y.; Jang, H.; Lee, S. Y.; Kim, J. M.; Kim, K. S.; Ahn, J.-H.; Kim, P.; Choi, J.-Y.; Hong, B. H. *Nature* **2009,** 457, 706-710.

(3) Reina, A.; Jia, X.; Ho, J.; Nezich, D.; Son, H.; Bulovic, V.; Dresselhaus, M. S.; Kong, J. *Nano Letters* **2008,** 9, 30-35.

(4) Meyer, J. C.; Geim, A. K.; Katsnelson, M. I.; Novoselov, K. S.; Obergfell, D.; Roth, S.; Girit, C.; Zettl, A. *Solid State Communications* **2007,** 143, 101-109.

(5) Meyer, J. C.; Kisielowski, C.; Erni, R.; Rossell, M. D.; Crommie, M. F.; Zettl, A. *Nano Letters* **2008,** 8, 3582-3586.

(6) Duplock, E. J.; Scheffler, M.; Lindan, P. J. D. *Physical Review Letters* **2004,** 92, 225502.

(7) Crespi, V. H.; Cohen, M. L.; Rubio, A. *Physical Review Letters* **1997,** 79, 2093.

(8) Gass, M. H.; Bangert, U.; Bleloch, A. L.; Wang, P.; Nair, R. R.; Geim, A. K. *Nat Nano* **2008,** 3, 676-681.

(9) Bangert, U.; Gass, M. H.; Bleloch, A. L.; Nair, R. R.; Eccles, J. *Physica Status Solidi A* **2009,** 206, 2115-2119.

(10) Bangert, U.; Bleloch, A.; Gass, M. H.; Seepujak, A.; van den Berg, J. *Physical Review B* **2010,** 81, 245423.

(11) Eberlein, T.; Bangert, U.; Nair, R. R.; Jones, R.; Gass, M.; Bleloch, A. L.; Novoselov, K. S.; Geim, A.; Briddon, P. R. *Physical Review B* **2008,** 77, 233406.

(12) Kirkland, E. J., *Advanced Computing in Electron Microscopy*. 1. ed.; Plenum Press: 1998.

Evolution of Gold Nanostructure on Graphene

Recep Zan, Ursel Bangert, Quentin Ramasse, Konstantin S. Novoselov

Small, 2011, 7(20), p.2868-2872

TOC

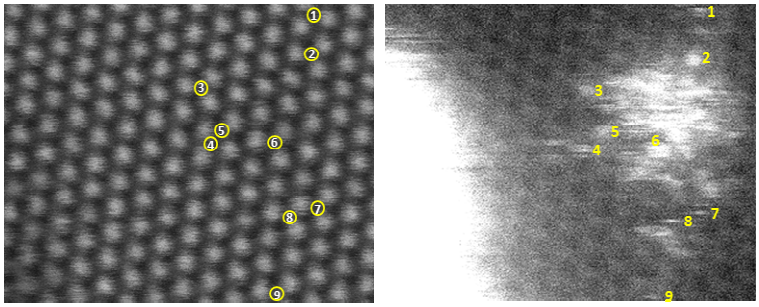

Ever since the first experimental observation of graphene[1] much of graphene research has concerned the control of its intrinsic properties. Attempts to achieve this have included doping or functionalising either with metals,[2, 3] molecules[4] or exposure to a hydrogen plasma.[5] Metal-graphene interactions have been much studied theoretically, in terms of the specific sites of the metals on the benzene ring, their binding energies etc. So for example, center-ring positions (H-sites) are predicted as preferred locations for most metals (e.g., Ti, Fe), corner sites directly above C-atoms (T-sites) for Sb, Sn and Ni, and bridge-sites above C-C bonds (B-sites) for Pd, Cr and Pt.[6-10] Some predictions are even in contradiction with each other because of different approximations for the calculations; the local density and the generalized gradient approximation lead to different binding energies and thereby to different sites. For Au atoms for example, T-sites are predicted by the former and B-sites by the latter method.[11] Furthermore, arbitrary variables used in the calculation, such as cut-off energies[12] and size of the supercell,[13] can affect the result of DFT calculations. Also, some calculations predict gold to dope graphene n-type, others predict p-type doping effects.[11, 14, 15] The contradictions in the calculations have so far not been resolved by experimental studies, for example McCreary et al.[16] predict n-type doping of graphene for gold deposition, whereas p-type doping is predicted from Raman spectroscopy studies of the gold-graphene interaction[17]. The gold–gold interaction is

expected to be significantly stronger than the gold–graphene interaction (for this reason gold is highly mobile on graphene).[12] This is experimentally confirmed by Gan et al.[14], who observed gold clusters (not individual atoms) on graphene. Indeed, on grounds of DFT calculations Pinto et al.[15] propose Au does not at all dope single layer but bilayer graphene. However, as theoretically predicted and experimentally confirmed, point defects in graphene can provide nucleation sites and even mediate substitutional incorporation of metals.[14, 18-22]

Au is one of the most widely used metals for a range of graphene applications, including making contacts to circuits,[1] electrochemical catalysis,[23] biosensors[24] and studying interfaces.[25] So direct observation of the gold behaviour on graphene –e.g., nucleation and coverage– in particular via TEM, is one of the key requirements to understand the nature of the interaction, and to gain a better understanding of the properties of metal contacts on suspended single layer graphene and their effect on macroscopic electrical transport. The graphene surface, due to its π-electron system, is inherently reactive, especially with regards to adsorbing hydro-carbon chains, which in turn are strong competitors as metal nucleation sites and will impose impedances on electrical transport into the metal, greatly defying the objective of exploiting the outstanding properties, such as the phenomenal carrier mobilities in graphene. On the other hand, 'extrinsic' nucleation sites might prove crucial because of the weak interaction of graphene with metals, as also predicted above. In this case it is essential to identify the right amount and nature of essential extrinsic nucleation sites, e.g., hydro-carbon contamination, in order to prevent deterioration of the electrical properties. Several groups have studied the deposition of gold nanoparticles on functionalised graphene in solutions.[26-28] These studies point out that oxy-functional groups, which act as nucleation sites, facilitate seeding and growth of Au clusters. However, in this article we explore the structural evolution of gold films evaporated on graphene, which has been obtained via exfoliation or CVD-growth methods.

Figure 1 shows results of various gold depositions: we never observed gold atoms on single or de-coupled (turbostratic) layers, however, gold clusters and nano-crystals form in the hydrocarbon contamination, revealed by the worm-like contrast in the HREM images. This demonstrates the extreme mobility of gold on pure graphene, similar to observations by Charlier et al., of Au-doped carbon nanotubes.[19]

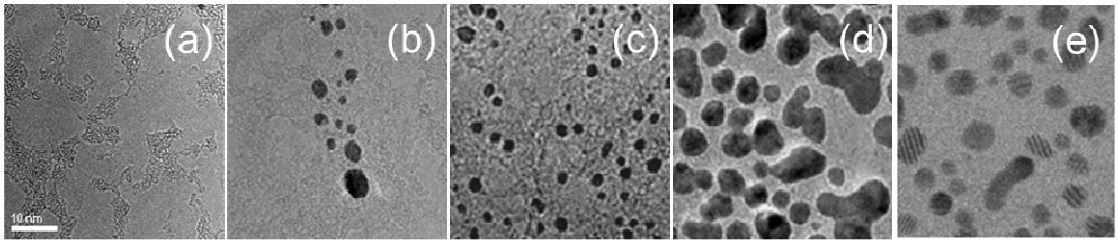

Figure 1. (a)-(d) TEM images of different gold coverages of the same graphene sample, which was repeatedly exposed to gold evaporation amounting to nominal thicknesses of <0.1, 0.12 and 2.12 nm. (a) Sparse coverage and (b) the occasional group of clusters at 0.1 nm gold thickness. (c) Higher cluster densities at 0.12 nm (1 s evaporation with 1.2 Å/s evaporation rate) and d) coalescence of clusters at 2.12 nm (2nm evaporation on the same sample) gold thickness. (e) STEM bright field (BF) image showing coverage following a single gold evaporation to nominally 0.5 nm thickness. The scale bar, 10 nm, is the same in all images.

The gold cluster density increases initially with increasing evaporated Au-amount, and at a nominal gold thickness of >1 nm clusters start to coalesce as a result of continued evaporation. The images in Figure 1 a)-d) demonstrate this in samples evaporated with <0.1, 0.12 and 2.12 nm of gold, respectively.

Figure 2 shows merging of clusters. The clusters stay surrounded by contamination, indicating that even at high nucleation densities preferred nucleation points remain within the contamination. There are, however, lighter areas within the clusters. This is due to the fact that the clusters overlay clean graphene patches. Two such positions are encircled in yellow; the left one occurs at the coalescence front of two particles, the right one in the middle of a particle. The gold layer is also thinner in these regions, suggesting that gold atoms prefer deposition on existing gold clusters before they are finally forced to spread across, or indeed, bridge clean graphene areas. Lattice images are less clear in these ‘bridging’ regions, suggesting disturbance of the electron wave function possibly due to decoupled, randomly oriented lattices between the two materials. Particles contain planar faults in the coalescence planes or undergo twinning (top and bottom arrow in figure 2b).

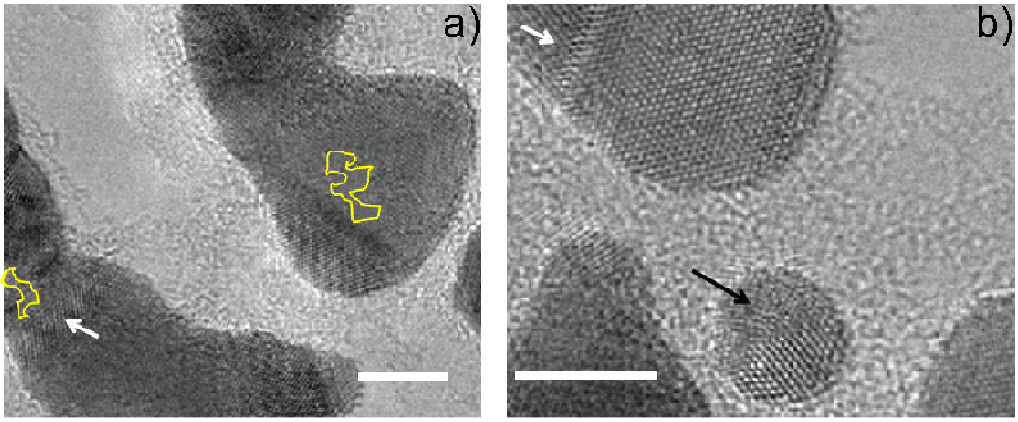

Figure 2. Coalesced clusters after 2.12 nm gold evaporation showing (a) variations in thickness and relative crystallographic orientations and (b) planar faults like stacking faults (white arrows) and twin boundaries (black arrow). The scale bar in both images is 5 nm.

Single gold atoms can only be observed on few-layer graphene films, where the bonding contribution from sub-surface layers appears to prohibit their diffusion and increases interaction with the graphene surface. **Figure 3**a) is a BF (i.e., phase contrast) STEM image with the beam focused onto the graphene and not onto the gold cluster (which is positioned at the exit surface); hence the gold atom aggregate is invisible. However, the benzene rings exhibit strong contrast and relatively little noise, and so the BF image can be used as a guide to identify positions in the corresponding, simultaneously acquired HAADF image (fig. 3b), which has inherently much lower intensity, but in which the gold atoms are clearly visible. The loose aggregate (on the right in figure 3b) with single atoms in its vicinity (some of which have been numbered) has formed as a result of repeated electron beam scans, during which atoms were dissociated from a larger gold nano-crystal (bright area on the left in figure 3b. To correlate the BF- and HAADF-contrast with the location of the benzene rings, STEM image simulations were carried out (3 layer simulations at -5 nm defocus giving the best match) and shown as insets in figure 3c and d). The benzene ring centres of the top layer correspond to bright patches in the BF (c) and to dark patches in the HAADF image (d). The model structure (black benzene rings) is overlaid in identical locations on both images. Hence C-atoms constitute dark contrast in BF and bright contrast in HAADF images. Comparing locations of gold atoms in the HAADF image with identical positions in the BF image (circles), the sites can be identified as T-sites.

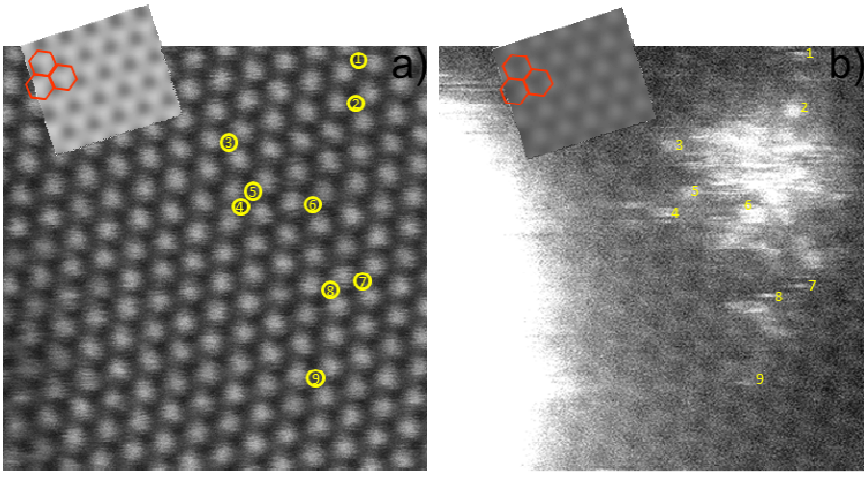

Figure 3. (a) BF and (b) HAADF STEM image of 0.5 nm gold evaporated on few-layer graphene. In the HAADF image individual gold atoms can be seen to have separated from a gold cluster on the left hand side. Identical positions of the benzene rings are marked in red in the image simulations overlaid on the experimental images, showing that bright contrast in the BF image and dark contrast in the HAADF image corresponds to the centres of benzene rings. Single atom positions 1-9 are marked with numbers just to the right of the bright atoms in the HAADF image; identical places are marked by yellow circles with the numbers inside in the BF image, showing that Au-atoms sit on T-sites on the sample surface. All images represent raw, unfiltered data. The frame width is 3nm.

As mentioned before these singular gold atoms are always found exclusively in close vicinity of very thin gold clusters, from which they have presumably been separated by the scanning electron beam. On few-layer graphene small gold clusters were found to sit directly on the pristine surface, giving rise to Moiré effects. The wide fringes in the cluster in **Figure 4**a) arise from rotational Moiré effects, where the Moiré fringe spacing depends on the difference in lattice spacing between gold and graphene as well as on the rotation angle of the two lattices with respect to each other. The largest proportion of gold clusters shows Moiré fringe spacing as seen in figure 4a). Analysis of the patterns shows that the graphene 100-type planes with spacing 2.1 Å conform to the (200) planes of the gold crystals (2.035 Å). The latter present themselves in [110] orientation on the graphene surface, and due to the mismatch, undergo rotations (~ 5°). Figure 4b) is a noise filtered HAADF image, using the circular low pass filter in the FFT in the inset. Image 4b) is taken simultaneously with the BF image 4a). Both, the graphene and the gold lattice can be seen in the HAADF image. Sections of the two lattices are shown enlarged next to each other in the inset: the gold (111) planes are slightly rotated with respect to two sets of the graphene

(100) planes; this achieves maximum coincidence of plane spacings in the gold [110] and the graphene [001] zone. Further matching is achieved by the gold 200-planes being oriented parallel to the third set of the graphene (100) planes, as can be observed in the FFT inset in figure 4b; the spacings of these planes are the most similar in the two structures. Rotation will, however, reduce contact points between gold and graphene.

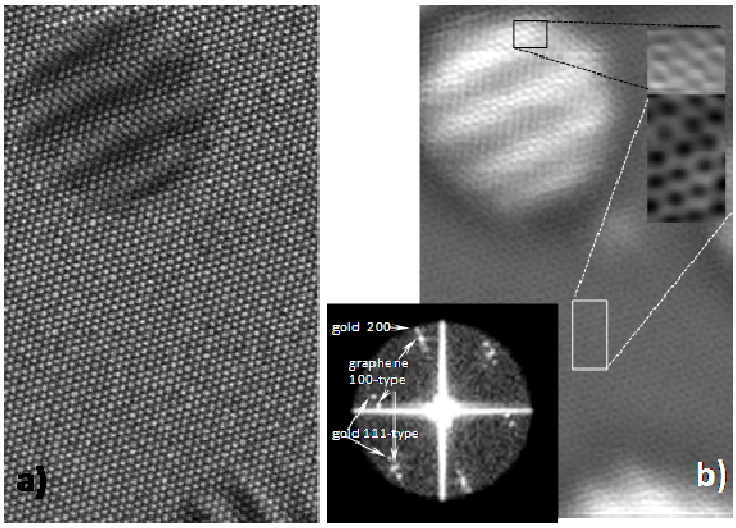

Figure 4. (a) Atomic resolution BF STEM image of few layer graphene with gold clusters revealed by Moiré effects. (b) Noise filtered HAADF STEM image of same area as in (a), showing both, the graphene and the gold lattice. The bottom inset is the FFT of the raw HAADF image showing the low pass filter that was used to obtain image (b). The FFT also reveals rotation of the gold (111) planes and orientation coincidence of the gold 200 planes and the graphene planes. The top inset shows enlarged gold and graphene lattice structure, revealing directly the gold and graphene lattice orientation relationship.

Further to doping with metals, an alternative way to modify and functionalize graphene is by dosing, for example with hydrogen and fluorine[5, 29, 30]. Hydrogenation breaks graphene sp^2 bonds and leads to sp^3 bond formation, thereby opening up a band gap. We have carried out gold deposition on graphene surfaces, which have been hydrogenated. The reason for this experiment was to investigate whether hydrogenated surfaces might increase the sticking probability for gold atoms. To conduct a fair comparison, gold evaporation was performed for the same amount (0.2 nm) and simultaneously on hydrogenated and pristine graphene surfaces. As can be seen in **Figure 5**a) the hydrogenated sample has a higher gold coverage, and gold cluster distributions and cluster sizes are of higher uniformity than in the pristine graphene sample, as shown in the image in Figure 5b), taken at the same magnification. In the latter case less than half of the

area is covered with gold and cluster sizes vary. The diffraction pattern of the sample in Figure 5a) (inset) shows a ring, which arises from small, randomly oriented clusters. In contrast the diffraction pattern of the pristine sample in Figure 5b shows distinct spots, arising from few clusters with bigger sizes. Both diffraction patterns clearly show graphene spots. However, similar to pristine graphene, gold is only retained in the contamination in the hydrogenated sample, as can be seen in the higher magnification images in figure 5c) and d).

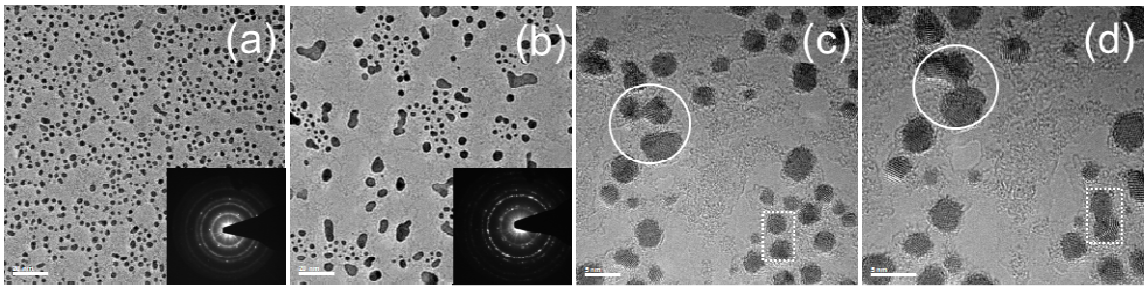

Figure 5. (a)-(b) TEM images of 0.2nm gold evaporated onto hydrogenated and pristine graphene shown at the same magnification (scale bar 20 nm). The corresponding diffraction patterns are shown as insets. (c)-(d) Images of gold evaporated onto hydrogenated graphene, taken in subsequent scans, and showing how gold cluster have coalesced (the solid circles and the dashes rectangles; scale bar 5 nm).

The above observations can be explained as follows: Gold does not stick to (uncontaminated) graphene surfaces, pristine or hydrogenated. A possible reason why hydrogen-modified graphene does not show an increase the sticking probability might be due to the fact that hydrogenation takes place predominantly in the contamination; here it appears to provide increased bonding, as it causes the gold to adhere indeed more effectively, hence the higher nucleation rate of gold clusters in the contamination. This might also explain the observable coalescence of gold cluster under the electron beam in the hydrogenated sample, which is not seen in the pristine sample. An example of this process in the hydrogenated sample is shown in Figure 5c) and d); the time elapsed between the acquisition of the images is less than 10 second. Hence agglomeration of clusters (indicated with solid circles and dashed rectangles in Figure 5c and d) occurs relatively rapidly. In contrast, in the pristine sample coalescence of small clusters has most likely already happened during evaporation; here the process carries on between already coalesced larger clusters after prolonged e-beam exposure (several minutes), comprising the unfavourable route of bridging clean graphene patches (see Fig 2a, white shapes). This

confirms the aforementioned suggestion that hydrogenation of the contaminants, which appear to act as 'the substrate', enables stronger interaction with the gold clusters; hence a diffusion barrier has to be overcome in the first place -with the aid of the e-beam- to initiate coalescence of gold clusters.

In conclusion, it appears that gold atoms do not adhere to clean single-layer graphene, but, already at the lowest deposition thickness of <0.1 nm, form clusters (2-3 nm in diameters), which nucleate exclusively in the abundant hydro-carbon surface contamination. Higher deposition thicknesses result in a higher density of clusters. At a thickness of >1 nm, the density remains rather constant; however gold particles grow to coalesce. During this stage clean graphene areas inevitably have to be bridged, however, whether and how gold actually bond with graphene, and whether charge transfer into electrical contacts deposited in this way proceeds, in the largest part, across a macromolecular (hydrocarbon) layer, requires further investigation. Gold thicknesses on the hydrocarbon contamination are much larger, and 3-D crystals grow under extended fault and twin formation. 2-D gold nano-clusters as well as single gold atoms do, however, adhere to clean surface areas in few-layer graphene The 2-D clusters here undergo rotation to achieve matching of planes in the gold (110) and graphitic [001] zone, and the sites of single gold atoms were identified as T-sites, i.e., on top of carbon atoms. Gold nucleation on hydrogenated graphene surfaces is confined to the contamination; however, the gold coverage is higher than on pristine graphene for the same evaporated amount of gold, with a greater uniformity of cluster size and distribution. This is thought to be due to provision of stronger bonding within the hydrogen-modified surface contamination.

Experimental Section

We employ two different techniques for graphene preparation, (i) exfoliation from HOPG graphite (few-layer sample)[1] and (ii) the CVD method, in which graphene is grown on copper (Cu) (mono-layer samples).[31] We have evaporated various amounts of gold, from less than 0.1 up to 2.12 nm, using electron beam and thermal evaporators. Evaporation was performed at room temperature and ~10^{-8} mbar pressure. Hydrogenation has been carried out by exposing graphene on a TEM grid to a cold hydrogen plasma. For this purpose a low-pressure (0.1 mbar) hydrogen-argon mixture (10% H_2) was used. Because the graphene is freely suspended on the TEM grid, hydrogenation occurred on both surfaces. Graphene samples were kept in the hydrogen plasma for one hour; the

system pressure before plasma formation was about $5x10^{-6}$ mbar. Details about the hydrogenation can be found in the literature.[5]

For high resolution imaging, including atomic resolution lattice imaging of gold crystals and atoms on the graphene surface, transmission electron microscopy was carried out in stationary mode (TEM) as well as in scanning mode (STEM), the former in a Tecnai F30, the latter in an aberration corrected dedicated STEM (Daresbury SuperSTEM), where advantage was taken of the high angle dark field imaging mode, the contrast of which has an approximate Z^2 dependence and is therefore suited to directly reveal atomic sites of singular metal atoms on graphene. Details of the method and first results have been reported previously.[32] Here we present an in-depth study of the behaviour of Au-atoms evaporated onto pristine and hydrogenated graphene surfaces.

STEM image simulations of graphene layers were performed by using the Kirkland TEMSIM program.[33] The multislice approximation was employed to calculate the electron wave function exiting the specimen. The simulations have been carried out with the microscope parameters used to acquire the experimental STEM images. These parameters are: beam energy 60 keV, Cs -0.03 mm, convergence angle 27 mrad, BF detector angular range 0-6 mrad and HAADF angular range 70-210 mrad.

Acknowledgements

This work is supported by EPSRC (UK).

References

[1] K. S. Novoselov, A. K. Geim, S. V. Morozov, D. Jiang, Y. Zhang, S. V. Dubonos, I. V. Grigorieva, A. A. Firsov, *Science* **2004**, *306*, 666.

[2] S. Huh, J. Park, K. S. Kim, B. H. Hong, S. B. Kim, *ACS Nano* **2011**, *5*, 3639.

[3] Y. Shi, K. K. Kim, A. Reina, M. Hofmann, L.-J. Li, J. Kong, *ACS Nano* **2010**, *4*, 2689.

[4] R. Erni, M. D. Rossell, M.-T. Nguyen, S. Blankenburg, D. Passerone, P. Hartel, N. Alem, K. Erickson, W. Gannett, A. Zettl, *Physical Review B* **2010**, *82*, 165443.

[5] D. C. Elias, R. R. Nair, T. M. G. Mohiuddin, S. V. Morozov, P. Blake, M. P. Halsall, A. C. Ferrari, D. W. Boukhvalov, M. I. Katsnelson, A. K. Geim, K. S. Novoselov, *Science* **2009**, *323*, 610.

[6] K. T. Chan, J. B. Neaton, M. L. Cohen, *Physical Review B* **2008**, *77*, 235430.

[7] Y. Y. Mao, Jianmei; and Zhong, Jianxin *Journal of Physics: Condensed Matter* **2008**, *20*, 115209.

[8] H. Sevincli, M. Topsakal, E. Durgun, S. Ciraci, *Physical Review B* **2008**, *77*, 195434.

[9] I. F. Suarez-Martinez, Alexandre; Pireaux, Jean Jacques; Bittencourt, Carla; Ewels, Christopher P., *Journal of Nanoscience and Nanotechnology* **2009**, *9*, 6171.
[10] B. Uchoa, C. Y. Lin, A. H. Castro Neto, *Physical Review B* **2008**, *77*, 035420.
[11] U. Akturk, Olcay, M. Tomak, *Physical Review B* **2009**, *80*, 085417.
[12] R. Varns, P. Strange, *Journal of Physics: Condensed Matter* **2008**, *20*, 225005.
[13] O. Leenaerts, B. Partoens, F. M. Peeters, *Microelectronics Journal* **2009**, *40*, 860.
[14] Y. Gan, L. Sun, F. Banhart, *Small* **2008**, *4*, 587.
[15] H. Pinto, R. Jones, J. P. Goss, P. R. Briddon, *physica status solidi (a)* **2010**, *207*, 2131.
[16] K. M. McCreary, K. Pi, A. G. Swartz, W. Han, W. Bao, C. N. Lau, F. Guinea, M. I. Katsnelson, R. K. Kawakami, *Physical Review B* **2010**, *81*, 115453.
[17] J. Lee, K. S. Novoselov, H. S. Shin, *ACS Nano* **2011**, *5*, 608.
[18] D. W. Boukhvalov, M. I. Katsnelson, *Applied Physics Letters* **2009**, *95*, 023109.
[19] J. C. Charlier, et al., *Nanotechnology* **2009**, *20*, 375501.
[20] A. V. Krasheninnikov, P. O. Lehtinen, A. S. Foster, Pyykk, ouml, P., R. M. Nieminen, *Physical Review Letters* **2009**, *102*, 126807.
[21] Z. Zhou, F. Gao, D. W. Goodman, *Surface Science* **2010**, *604*, L31.
[22] Y. Okamoto, *Chemical Physics Letters* **2006**, *420*, 382.
[23] R. Muszynski, B. Seger, P. V. Kamat, *The Journal of Physical Chemistry C* **2008**, *112*, 5263.
[24] W. Hong, H. Bai, Y. Xu, Z. Yao, Z. Gu, G. Shi, *The Journal of Physical Chemistry C* **2010**, *114*, 1822.
[25] Z. Lee, K.-J. Jeon, A. Dato, R. Erni, T. J. Richardson, M. Frenklach, V. Radmilovic, *Nano Letters* **2009**, *9*, 3365.
[26] G. Goncalves, P. A. A. P. Marques, C. M. Granadeiro, H. I. S. Nogueira, M. K. Singh, J. Gracio, *Chemistry of Materials* **2009**, *21*, 4796.
[27] P. V. Kamat, *The Journal of Physical Chemistry Letters* **2009**, *1*, 520.
[28] K. Jasuja, J. Linn, S. Melton, V. Berry, *The Journal of Physical Chemistry Letters* **2010**, *1*, 1853.
[29] R. R. Nair, W. Ren, R. Jalil, I. Riaz, V. G. Kravets, L. Britnell, P. Blake, F. Schedin, A. S. Mayorov, S. Yuan, M. I. Katsnelson, H.-M. Cheng, W. Strupinski, L. G. Bulusheva, A. V. Okotrub, I. V. Grigorieva, A. N. Grigorenko, K. S. Novoselov, A. K. Geim, *Small* **2010**, *6*, 2877.
[30] J. O. Sofo, A. S. Chaudhari, G. D. Barber, *Physical Review B* **2007**, *75*, 153401.
[31] X. Li, W. Cai, J. An, S. Kim, J. Nah, D. Yang, R. Piner, A. Velamakanni, I. Jung, E. Tutuc, S. K. Banerjee, L. Colombo, R. S. Ruoff, *Science* **2009**, *324*, 1312.
[32] R. Zan, U. Bangert, Q. Ramasse, K. S. Novoselov, *Nano Letters* **2011**, *11*, 1087.
[33] E. J. Kirkland, *Advanced Computing in Electron Microscopy*, 1. ed., Plenum Press, **1998**.

6.4 Conclusions

Investigation of Au, Cr and Fe on suspended graphene membranes showed that clean single-layer graphene surfaces do not retain any metal impurity atoms of these metal impurities. All investigated metals reside in/on the hydrocarbon contamination that is abundant on graphene surface. Metals tend to form clusters on the hydrocarbons rather than exist as individual ad-atoms even for the lowest amount of metal deposition on the graphene surface. Higher deposition thicknesses for the Au case result in a higher density of clusters which eventually coalesce. As a result of coalescing of the clusters, the clean graphene regions were bridged. Although neither individual ad-atoms nor clusters were not observed on the clean parts of single layer graphene, Au ad-atoms and their clusters were observed on few-layer graphene. However, the single atoms are believed to be dragged onto the few-layer graphene as a result of the scanning beam as no such observation was made in stationary mode (HRTEM) imaging.

On the other hand, Au behaviour on the hydrogenated graphene surfaces has changed in comparison to the pristine surface although again no Au was found on clean parts of the single layer areas. Individual ad-atoms and clusters of Au again preferentially nucleate on the hydrocarbon contamination. However, the gold coverage is more disperse for the same amount of gold, with smaller cluster size of greater uniformity. This is in contrast to much bigger (3D) cluster on the pristine surface. This behaviour also points out a stronger bonding of Au with the surface contamination of the hydrogenated sample that provides more nucleation side.

Although investigations on fluorinated graphene samples are at an early stage, based on initial results no observable difference has been seen for metals here in terms of their distribution, interaction with clean areas and clustering behaviour in comparison to pristine graphene samples, although the fluorination was expected (based on DFT calculations) to amend the metal behaviour on the graphene surface.

Cr shows a better distribution (homogeneous with similar sized clusters) on the graphene surface than Au for similar amounts of metal deposition. This indicates a more continuous contact throughout the membrane, and stronger bonding to graphene. A destructive behavior of Cr on graphene has been observed: Cr dissociates carbon bonds in the graphene lattice leading to the formation of vacancies in the graphene layer. These vacancies might act as nucleation points for metals in subsequent depositions; in practical devices this is generally Au, which is used to form contacts on graphene based devices.

The weak interaction between the metal and graphene and the preponderance of metals to reside on the hydrocarbons might have effects on the electrical transport properties (deterioration in mobility) of graphene as the hydrocarbon contamination on the graphene surface is unavoidable unless annealed at high temperatures in UHV.

Chapter 7

Metal-Mediated Etching and Healing of Suspended Graphene

7.1 Introduction

In addition to their potential application for enhancing device performance, metals have been widely used to etch, pattern and even to thin graphene layers for a variety of purposes. There are well-established methods making use of metals to cut graphitic slabs and it was recently shown that these techniques could also be applied to graphene [16, 112]. There, elevated temperatures and gaseous environments were systematically employed to activate the cutting reaction catalysed by the metallic nanoparticles. Species other than metals, such as SiO_2 whose reactivity on graphene surfaces at high temperatures is well-known, can also be used in these processes [135, 136].

In the process of investigating the interaction between metal species and graphene in the (S)TEM, an intriguing etching phenomenon was observed. Although, as explained above, metals have been used on the graphene surface for tailoring purposes, in these new observations the etching occurred in the microscope column in near-UHV conditions at room temperature. This behaviour was therefore distinct from existing report of graphene etching via metals at high temperature and under gas flow. On the other hand, recent DFT calculations have suggested that the mere presence of Al, Fe, Co and Ni metal atoms could cause an effective reduction of the defect formation energy of graphene layers [22]. Thus holes could potentially be created without extreme heat and gas environment. Interestingly this destructive behaviour was not predicted for Au, the presence of which did not appear to alter the vacancy formation energy [22].

In addition, holes created in graphene using this etching behaviour were later observed to fill spontaneously, in a unique self-healing mechanism. While hole-filling in graphene and graphite is reasonably well-known, all previous observations were achieved under extreme heat (>1000 ^{o}C) in the TEM, making these observations quite remarkable.

7.2 Sample Preperation

CVD-grown single-layer graphene samples were used for these experiments. The graphene layers were transferred to TEM grids as detailed in Chapter 3. An accurately controlled amount of Au, Ti, Pd, Al and Ni were deposited on the samples *via* electron-beam evaporators, corresponding to a 0.2 nm surface coverage. Alongside these metals unintentional dopants like silicon and silica, which are abundant on the graphene surface, were also studied.

Graphene layers were identified in a Tecnai F-30 microscope prior to metal deposition to ensure the samples consisted mostly of single layer graphene and were not heavily contaminated. HAADF and EELS investigations were carried out at SuperSTEM on an UltraSTEM 100 microscope at room temperature, at 60kV acceleration voltage. The UHV design of the column, its high brightness cold field emission electron gun along with its high stability made this microscope the ideal tool for these investigations. Metal species could be identified directly either through contrast analysis of HAADF images or *via* EELS. EEL spectra were recorded on a Gatan Enfina spectrometer.

In addition, first-principles calculations were performed to find out possible graphene etching mechanism in presence of silicon and silica. The SIESTA code with the generalized gradient approximation was used for the modelling.

7.3 Results and Discussion

The results of this project were published in ACS Nano and Nano Letters in 2012. The original manuscript for **"Direct Experimental Evidence of Metal-Mediated Etching of Suspended Graphene"** *(ACS Nano, 2012, 6(5), p.4063-4071)* and **"Graphene Reknits Its Holes"** *(Nano Letters, 2012, 12(8), p.3936-3940)* are presented below.

Direct Experimental Evidence of Metal-Mediated Etching of Suspended Graphene

Quentin M. Ramasse, **Recep Zan**, Ursel Bangert, Danil W. Boukhvalov, Young-Woo Son and Konstantin S. Novoselov

**The first two authors have contributed equally to the work.*

ACS Nano, 2012, 6(5), p.4063-4071

ABSTRACT

Atomic resolution high angle annular dark field imaging of suspended, single-layer graphene, onto which the metals Cr, Ti, Pd, Ni, Al and Au atoms had been deposited was carried out in an aberration corrected scanning transmission electron microscope. In combination with electron energy loss spectroscopy, employed to identify individual impurity atoms, it was shown that nano-scale holes were etched into graphene, initiated at sites where single atoms of all the metal species except for gold come into close contact with the graphene. The e-beam scanning process is instrumental in promoting metal atoms from clusters formed during the original metal deposition process onto the clean graphene surface, where they initiate the hole-forming process. Our observations are discussed in the light of calculations in the literature, predicting a much lowered vacancy formation in graphene when metal ad-atoms are present. The requirement and importance of oxygen atoms in this process, although not predicted by such previous calculations, is also discussed, following our observations of hole formation in pristine graphene in the presence of Si-impurity atoms, supported by new calculations which predict a dramatic decrease of the vacancy formation energy, when SiO_x molecules are present.

TOC

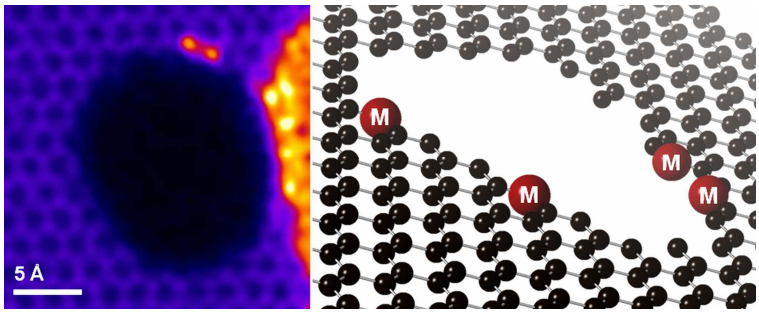

Since the first isolation of single layer graphite,[1] or graphene, a large body of research has been devoted to the remarkable electronic, structural and physical properties of this unique material, often with a view to utilising it for practical applications.[2] Almost by definition, however, the fabrication of any graphene-based device involves the incorporation of metal contacts, to exploit its thermal or electrical conductivity for instance. The use of either Au, Cr, Ti or Pd has been shown to dramatically affect the performance of the resulting devices and it follows that the choice of metal is therefore key to a successful design.[3, 4] Furthermore, metals like Zn,[5] Ni,[6, 7] Ag[8, 9] and Co[10, 11] or even non-metallic SiO_x[12] have all been used to tailor graphite and graphene into specific shapes such as nano-ribbons, by either oxidation or hydrogenation at elevated temperature, resulting in the formation of various by-products.[13] As a result, a number of recent studies have focused on the behaviour and interactions of deposited metal ad-atoms or nano-particles on graphene surfaces. Most of these are based on theoretical simulations such as Monte Carlo, molecular dynamics (MD) or density functional theory (DFT) to calculate the structure, bonding, and potential charge transfer of different adsorbed metal ad-atoms on materials.[14-18] Unfortunately, depending on the approach used for these calculations and in particular the choice of parameters and approximations, the results are not always consistent. Ni, for instance, was predicted to exhibit either strong[16, 19] or weak[18, 20] binding to graphene. As a general rule, however, transition metals (TM) have been predicted to bond covalently to the graphene surface resulting in significant lattice distortions whilst by contrast alkaline metals are ionically bonded to graphene and cause little distortion.[14, 21] In practice, it was recently demonstrated experimentally that instead of adhering to the free surface of graphene metals tend to cluster on top of the ubiquitous hydrocarbon-based contamination, which seems to indicate a very weak affinity between metals and graphene.[22] This weak TM-graphene interaction can be mediated by deliberately introducing vacancies (*i.e.* defective sites) into graphene sheets prior to deposition where some metal atoms can then be trapped[23-25] as a result of bonding rearrangements around the defects and a decrease of the adsorption energy barrier. In this case, it was recently calculated that with the exception of Au, whose interaction with graphene is consistently predicted to be weak, the presence of Al, Fe, Co and Ni metal atom impurities on or within the graphene layer can in turn lead to a dramatic reduction of the formation energies of further defects and therefore to the formation of large holes in the sheet. This would imply that graphene could be destroyed easily by the mere addition of metal atoms, a conclusion that has serious potential implications for graphene device fabrication.[26] It is therefore

essential to devote renewed experimental attention to metal-graphene interactions in order to confirm or disprove this predicted deleterious behaviour and perhaps to propose new mechanisms whereby it could be alleviated. Transmission electron microscopy (TEM) is the ideal tool for such studies, especially with the mounting interest in so-called suspended devices, which eliminate substrate effects and thus exploit the intrinsic properties of free-standing graphene.[2] Indeed, the technique's ability to image and identify directly each and every atom in 2D materials has already played a significant role in the establishment of graphene as one of the most studied materials of the 21st century by providing arguably the most visually striking proofs of its existence.[27]

Here we present a systematic scanning transmission electron microscopy (STEM) study of the interaction of suspended single-layer graphene sheets with metals, namely Au, Cr, Ti, Pd, Ni and Al, as well as with Si (present in our samples as an unintentional impurity: see Materials and Methods), through a model system consisting of individual ad-atoms and/or aggregates of atoms (clusters) deposited on free-standing graphene. The effects on the structure of graphene were observed at ambient temperature in ultra high vacuum (10^{-9} torr) and at a primary beam energy (60 kV) well below the knock-on damage threshold for carbon,[28] *i.e.* in conditions that are expected to allow for safe, prolonged, observation of the material without altering its structural integrity. A combination of chemically-sensitive Z-contrast imaging and electron energy loss spectroscopy (EELS) allowed us to confirm that in spite of these specific environmental conditions, etching does take place in the presence of all deposited elements with the exception of Au. Etching systematically initiated at the edges between clean graphene areas and the macro-molecular contamination layers where the metal clusters and impurity atoms tend to sit. Based on further theoretical results, we suggest that this behaviour is due to the local oxidation of the metallic ad-atoms, the oxygen activation energy barrier being possibly overcome by local heating as a result of energy transfer from the beam followed by C-atom dissociation through C-O formation.

Although only on a model system, the observation and elucidation of this metal-mediated etching behaviour is an essential result at a time when graphene is moving from the laboratory to the factory floor. A better understanding of the properties of metal contacts on suspended layer graphene is essential for device fabrication, patterning and improving performance and our results point to the need for more systematic studies of nucleation and coverage in order to determine optimal contacts.[3, 4]

Results and Discussions

The monolayer graphene sheets used for this study were grown by chemical vapour deposition (CVD) on a copper substrate according to the method described by Li *et al*.[29] and metals were introduced onto the graphene membranes by means of evaporation, prior to STEM measurements. Figure 1 shows low magnification HAADF images of Au (a), Cr (b), Ti (c), Pd (d), Ni (e) and Al (f) deposited on single layer graphene sheets (as verified using electron diffraction in a conventional TEM prior to deposition: see supplementary material, figure S1). The same amount of metal (2 Å) was evaporated in each case for accurate comparison. Consistent with recent observations, the deposited metals have formed clusters located exclusively on top of the ubiquitous hydrocarbon contamination (residues from the transfer, or contamination due to exposure to air) partially covering the surface of graphene.[22] No such clusters were observed directly on clean single-layer graphene (the darker patches on fig. 1) throughout this study, irrespective of the preparation method. A similar amount of Au was deposited on exfoliated single layer graphene (not shown here) resulting in a similar behaviour to the CVD-grown samples, on which we will concentrate for the rest of this study. This lack of adherence of transition metal atoms on pure graphene, or in other words their apparent high mobility on clean graphene surfaces, illustrates how significantly stronger the metal-metal interactions are than the metal–graphene interactions.[22, 30] Indeed this behaviour was predicted by DFT calculations[31] and MD simulations,[32] which suggested that clustering is more energetically favourable for transition metal atoms than remaining isolated. By contrast alkali metals are expected to form 2-dimensional continuous films on top of the graphene surface.[32]

In spite of identical deposition conditions the physiognomy of the samples varies significantly. Au clusters (fig. 1a) are larger and denser and as a result coverage is sparser than for the other metals. Pd (fig. 1d) and Ni (fig. 1e) also agglomerate into well-defined metallic nano-particles, albeit of much smaller sizes than Au, resulting in a more uniform coverage of the sample. Cr (fig. 1b) and particularly Ti (fig. 1c) and Al (fig. 1f) exhibit a much higher fractional coverage with loose, flat, atomic aggregates.

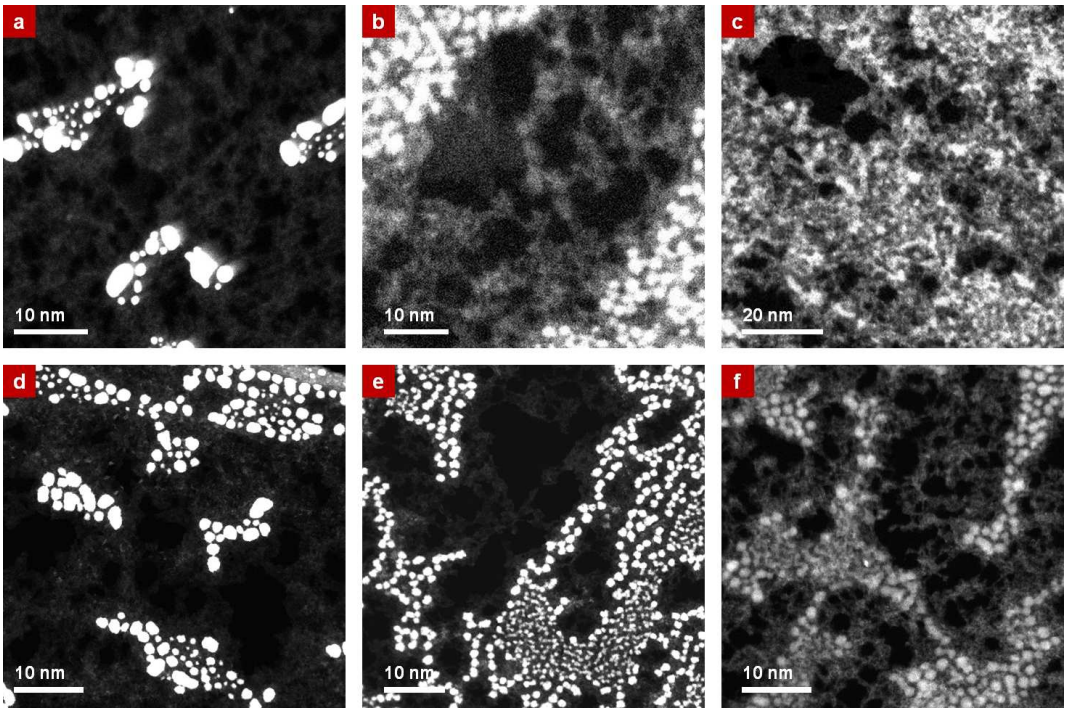

Figure 1. Low magnification HAADF images of metals on monolayer graphene show an overview of the metal distribution for: (a) Au; (b) Cr; (c) Ti; (d) Pd; (e) Ni and (f) Al. The contrast and intensity were adjusted to reveal areas of clean graphene (dark patches) and 'contamination' layers (light grey patches) where the metals (white clusters) sit preferentially.

The propensity of the latter to oxidise into alumina may explain the aspect of that particular sample as the deposited Al may have oxidised during sample transport from the deposition chamber to the microscope or upon contact with the hydrocarbon layer. A similar argument can be made for Ti and Cr, which are commonly used as a precursor for the fabrication of Au contacts on graphene: the better coverage of the sample after deposition of those two metals observed here may be an illustration of their effectiveness for such applications. Although none were applied here, surface pre-treatments such as hydrogenation (or oxidation) have been shown to affect the adherence of metals to the samples, resulting for instance in smaller Au clusters and a more uniform coverage which in turn is easily degraded by beam-induced coalescence of the clusters under the electron beam.[30]

Although as can be seen in the overview images of fig. 1 the metal clusters sit preferentially in the middle of the hydrocarbon contamination, after a few scans of the electron beam at mid- to high-resolution (for high signal-to-noise images each scan can take up to 30s), some of the clusters and/or individual atoms can be dragged by the beam to

the edge of the contamination layer. Figure 2a shows an HAADF image of such a Ni cluster positioned at the very edge of a contamination area. Individual Ni atoms can be also seen to form a raft above a region of clean single layer graphene at the edge of the particle. While some carbon chains may still be present immediately under these Ni atoms, such a configuration offers a great proximity between pure graphene and the metal atoms. After a few additional scans of the beam, a hole has formed (fig. 2b), decorated by individual Ni atoms as evidenced by the clear Ni $M_{2,3}$ signature in the EEL spectrum (fig. 2c), acquired by placing the electron probe exactly on top of the bright atom marked on fig. 2b. This hole formation is obviously dynamic and additional stills from a time series of over 90 consecutive images illustrate the process further (see supplementary material, fig. S2). After the initial hole formation, individual Ni atoms are observed to jump onto the exposed edge before the hole is further enlarged, producing bright horizontal streaks in the images (figure 2a) as they are being captured at different positions by the beam as it is being rastered in a line. They can only be imaged once in a more stable position at the edge of the hole, such as on figure 2b. A strong indication that the drilling process is indeed metal-mediated arises from the observation that when no Ni atom is decorating the hole, the latter merely re-shapes dynamically (as expected from earlier reports[33]) but does not grow further in size (see supplementary material, fig. S3). In other words, the drilling stabilises when the local reservoir of metal impurity atoms is exhausted and until more Ni atoms are drawn towards the energetically unstable edges of the hole *via* surface diffusion thanks to the high mobility of single metal impurities on single layer graphene.

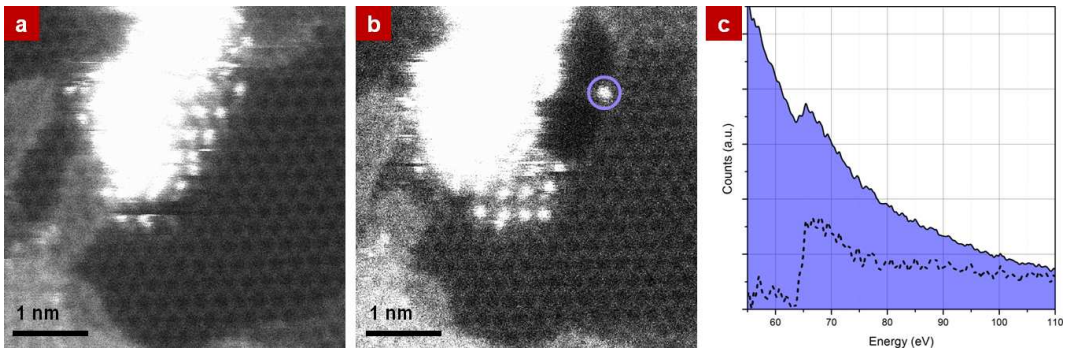

Figure 2. (a) HAADF image of a Ni cluster sitting on the very edge of the hydrocarbon contamination layer. Single Ni atoms have been dragged by the beam from the cluster and are in contact with the graphene monolayer. (b) After a few more scans, a hole has formed, whose edges are decorated by single Ni atoms, identified by their Ni $M_{2,3}$ EELS signal. (c) EELS spectrum acquired by positioning the beam for 1s on the bright atom circled in (b).

This behaviour (migration of the metal atoms under the beam to the edge of the contamination layer, drilling and hole enlargement) was reproduced identically when imaging single layer graphene samples on which palladium (fig. 3a), titanium (fig. 3b) and aluminium (fig. 3c) had been deposited, while in an earlier report a similar process had probably been at play but not recognised for the interaction of Cr with graphene.[22] In each case, the nature of the atoms decorating the edges of the newly formed holes was confirmed by placing the electron probe directly on top of them and recording an EELS spectrum, as shown on fig. 3.

Metals have been used as catalysts for patterning of graphene devices in hydrogen or oxygen flow at high temperatures,[6, 9, 11] and the addition of Ni in particular was predicted to lead to very low defect formation energies when interacting with single layer graphene.[26] However, neither gas environment nor high temperatures were used in our study, which is to our knowledge the first experimental evidence of electron beam-induced drilling of graphene through its direct interaction with metals. D. W. Boukhvalov and M. I. Katsnelson predicted this destructive behaviour (specifically for Fe, Co, Ni and Al) by calculating a drastic lowering of the formation energy for mono- and di-vacancies in single layer graphene when metal ad-atoms are present on the graphene surface.[26] The precise mechanism they propose in their *ab initio* calculations assumes a direct contact between a metal atom and the surface of free-standing graphene before the formation of the defects: as noticed above, some direct contact can be observed at the very edge of the contamination layer after a few scans of the electron beam, as illustrated on fig. 2a. While our observations seem to provide a direct experimental evidence of this metal-mediated destruction of graphene, it is important to consider other possible reasons for the severe drilling behaviour we observed.

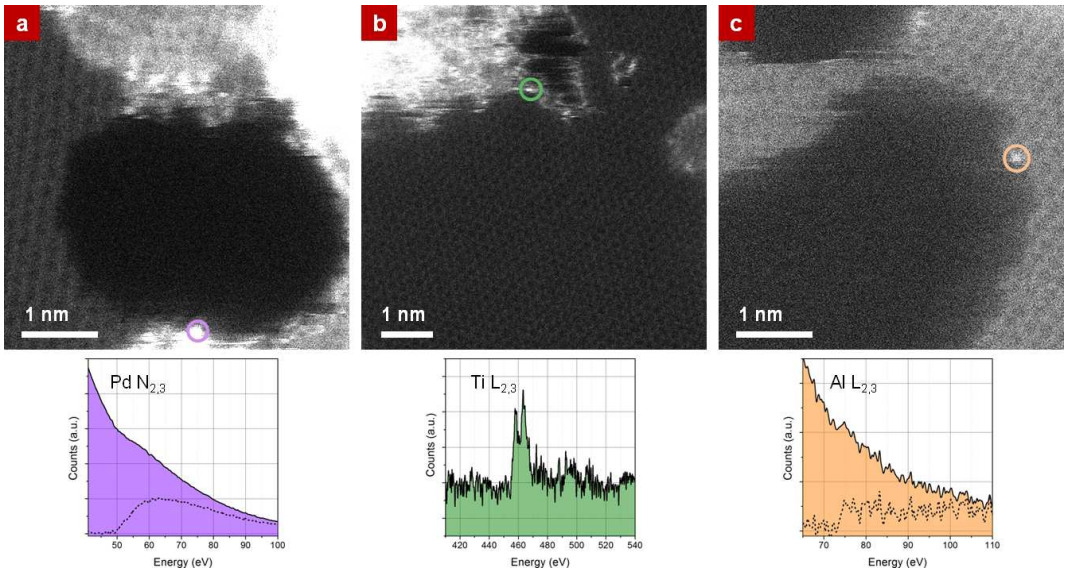

Figure 3. HAADF images of holes formed in monolayer graphene through metal mediated etching for (a) Pd, (b) Ti and (c) Al. EELS spectra acquired by positioning the beam for 1s on the atoms circled on the images are shown below. The dotted lines correspond to the EELS signal after background subtraction with a power law.

Although all are transition metals, these elements have been predicted to interact with graphene quite differently. Palladium has been used as an electrical contact in device fabrication for many years[34] and most recently in graphene devices[35] because of its lower cost compared to gold. Although it has a full d-shell, it is expected to bond covalently to graphene with a reasonably high adsorption energy.[14, 19] Recent DFT calculations also suggest that Pd atoms have a strong tendency to form three-dimensional rather than planar clusters on graphene, which indicate a weak Pd-graphene interaction[36] as evidenced by our observation, see fig 1d. Of all the metals used for this study, Ti is predicted to have the strongest interaction with graphene, bonding to its surface *via* chemisorption.[17, 19] Finally, Al is predicted to have ionic bonding to the graphene surface, similarly to the case of I-III metals, which unlike transition metals[14] are not seeing a significant modification of their electronic state. Furthermore, Al-doped graphene has been shown to be a promising material for hydrogen storage[37] while the deposition of a layer of aluminium oxide can be used as a gate insulator in graphene device fabrication.[38]

A constant trait of all those elements is their propensity to form oxides, which suggests that oxidation could be playing a major role in the effects we are observing. This theory could be further strengthened by the fact that by contrast no hole-forming was observed on Au-deposited samples (see supplementary material, fig. S4 and, for instance, Zan *et al.*[30]),

Au being of course not prone to oxidation except in very specific circumstances.[39] Nevertheless, even in the mono-vacancy formation model for the destruction of graphene proposed by Boukhvalov *et al.*,[26] Au is not expected to lead to a major loss in stability as its defect formation energy remains high so this observation cannot definitively point to a role of O in this etching process. As the depositions were conducted in thermal and e-beam evaporators where the vacuum is at least 10^{-7} torr, all metals being degassed prior to evaporation, the most likely sources of oxygen, should any be involved in this process, are therefore: the oxidation of the metal clusters and/or the retention of O by the hydrocarbon contamination during transport of the samples from the deposition chamber to the microscope; or a relatively high partial pressure of O in the microscope column. All samples were systematically left within the microscope vacuum for several days to ensure perfect thermal and mechanical equilibrium during observation: after such long waiting periods the slight pressure increase in the column due to sample insertion had subsided and the sample chamber was systematically at its base pressure of $<5\text{x}10^{-9}$torr. Sample degassing can be thus considered as an unlikely source of O. Graphene etching in oxygen environment is well-documented and the energy required for the oxidation of graphene is expected to be low.[40] Therefore, should a high partial pressure of O in the chamber be responsible for the observed hole formation it should be occurring everywhere, not only at the edges of the hydrocarbon contamination. Furthermore, at 60kV and in otherwise identical conditions perfectly clean patches of graphene were imaged by scanning the beam repeatedly for over an hour without any drilling. The hole formation mechanism we report here must therefore be either solely metal-mediated as in the model from Boukhvalov *et al.*,[26] or involve metal ad-atoms and oxygen from either oxidised metal clusters or oxidised surface contamination.

As a control experiment we studied a 'pristine' graphene sample, *i.e.* a single layer graphene sheet produced and processed in identical conditions but on which no metal was deposited. As mentioned previously, in the conditions used for our observations pristine single layer graphene patches can be imaged without any visible damage for extremely long periods of time, and with very large electron doses. Some carbon surface contamination may occasionally diffuse into the field of view depending on the area being observed (the C support film may act as a 'contamination reservoir'), but drilling or etching was never noticed when imaging clean areas of our samples. Although every attempt was made at obtaining extremely clean single layer graphene samples prior to metal deposition,

Si contaminants, either in the form of relatively large SiO_x clusters or of small single Si atoms are common[41] and were readily observed in our samples.

Substitutional Si impurities were found to be very stable. Figure 4a shows an HAADF image of a such a Si impurity, identified by EELS by placing the beam directly on top of it (figure 4b). Several such datasets were acquired sequentially, with the Si impurity atom always appearing on HAADF images recorded immediately after the 2s EELS acquisition took place, proof of the great stability of this structure. However, when imaging continuously the edge of a hydrocarbon contamination layer containing some Si impurities (identified by EELS), we were able to observe even on such 'pristine' samples the formation of a hole in the graphene sheet, although not as readily as with metal-deposited samples.

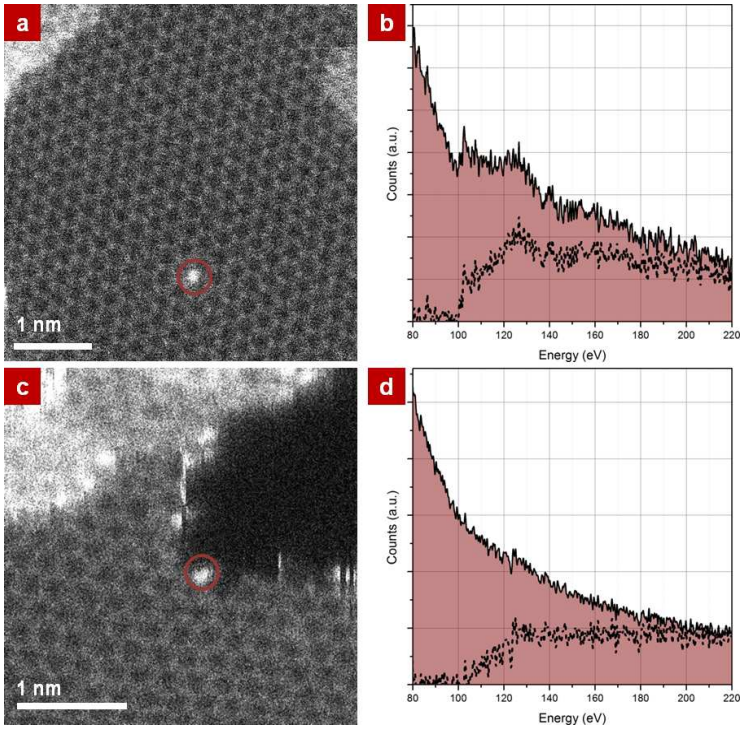

Figure 4. (a) HAADF image of a single substitutional Si atom within a graphene monolayer. An EELS point spectrum (b) acquired by positioning the beam for 1s on the atom confirms it is Si. This defect is extremely stable as it was possible to record several successive such datasets, the atoms remaining in position throughout. (c) HAADF image and corresponding EELS point spectrum (d) of a Si atom decorating a hole, just formed at the edge of the hydrocarbon contamination layer. The signal after background subtraction with a power law model is shown as the dotted line.

As in the metal case, the edges of the thus-formed hole were subsequently decorated by single atoms (figure 4c), identified as Si atoms by EELS (figure 4d). Again, the process was observed to continue until the local reservoir of Si impurity atoms is exhausted, at which point the drilling is halted and only a dynamic reshaping of the edges of the hole can be observed under the beam.

SiO_x has been shown to have potential applications in tailoring graphene sheets to specific shapes during annealing in hydrogen atmosphere around 900^{o}C, the high temperature, high pressure environment being crucial to the production of SiO_x particles from the surface of a Si/SiO_2 wafer.[12] The previously un-reported drilling mechanism observed on pristine samples is therefore quite different and may depend crucially on the vacancy formation energy barrier in case of a single Si ad-atom, Si cluster, SiO_2 molecules and/or SiO_2 cluster. We found computationally that single Si ad-atoms and crystalline Si clusters have similar vacancy formation energies (8.33eV and 8.36eV, respectively). These are close to the energy required for the formation of a single vacancy in graphene by irradiation (7eV)[42] and it can therefore be concluded that the presence of Si ad-atoms or crystalline clusters should not lead to any drilling behaviour. Similarly, un-passivated quartz (ordered SiO_2) was revealed to be relatively 'safe' for graphene: the energy required for the migration of a single oxygen from SiO_2 to the graphene surface is 3.14 eV (much higher than the energy required for the oxidation of graphene reported in the literature), while the unzipping of graphene along defect 'lines' of carbon monoxide molecules[43] is unlikely as the required energies for a single and a pair of epoxy groups are 6.94 eV and 9.69 eV, respectively. On the other hand, disordered silicon oxide molecules and clusters provide a plausible solution as both have a tendency to form metastable intermediate $Si_xO_yC_z$ structures.[44] The energies required for this process are 3.13 eV and 2.46 eV for silicon oxide molecules and silicon oxide clusters, respectively, which are very much comparable to the 2.5 eV energy formation of a mono-vacancy in the presence of Ni[26] (see supplementary material for details on the modelling parameters, fig. S5). We therefore propose that as in the case of metal-deposited graphene, disordered SiO_x molecules find themselves dragged to the edge of the contamination layer, where they interact with the graphene sheet. Upon formation of an initial unstable $Si_xO_yC_z$ structure, as suggested by our calculations, a hole appears and grows through the same mechanism, Si atoms or SiO_x clusters being drawn energetically to the exposed edges.

Finally, we point out that the exact role of the electron beam in either the metal-mediated drilling or in the Si case could not be directly elucidated from our sole observations. However, the formation of holes at the edge of the contamination layers away from the region being imaged (up to tens of nm) and the excellent conduction properties of graphene[45] point to a heat transfer mechanism, whereby local heating as a result of the irradiation by the beam is sufficient to overcome the defect formation energy barriers.

Conclusions

Using atomic resolution HAADF imaging and identification of single atoms by EELS, we have observed etching of suspended, single-layer graphene upon which metal atoms had been deposited. Etching occurred with all employed metals (Cr, Ti, Pd, Ni and Al) apart from gold. It also occurred in pristine samples with (unintentional) Si contamination. Metal clusters nucleate initially exclusively on hydrocarbon contamination. Nano-scale holes form in locations where metal atom clusters sit at the border of the contamination with pristine graphene, following the drag of individual metal atoms onto the pristine graphene surface during the e-beam scan. Theoretical modelling predicts that vacancy formation energies in graphene are substantially lowered in the presence of metal atoms. Although according to such calculations the presence of oxygen is not required in this metal-mediated vacancy formation, we suggest oxygen is present and indeed assists C-C bond dissociation *via* graphene oxidation. We derive this from the fact that vacancy formation in the presence of Si-oxide has much lower predicted energies -similar to these calculated for vacancy formation in the presence of Ni- than for Si-atoms or Si-clusters alone. The presence of O is further indicated by the fact that holes form at the edges of hydrocarbon contamination, added to observations that atoms from the deposits are being dragged onto the clean graphene. Lastly, etching does not occur in the presence of gold atoms, which do not oxidise, although the predicted vacancy formation energy is lowered. The role of the scanning electron probe is not fully established, but since hole formation also occurred in regions adjacent to but not directly in the e-beam scanned area, we suggest that the e-beam acts as a heat source.

Materials and Methods

The monolayer CVD grown graphene membranes were transferred to the TEM support grids using a standard wet chemistry methodology. Conventional TEM was used to

assess quality of the produced films: electron diffraction data confirmed near perfect coverage of the entire TEM grids with a single layer graphene sheet.[46] The samples were then placed either into an electron beam evaporator (for depositing Au, Cr, Ti and Pd) or a thermal evaporator (for depositing Al and Ni). In all cases, the same amount of material (2 Å of Au, Cr, Ti, Pd, Ni and Al) was deposited with a precisely calibrated rate of 0.1 Å/s, in a custom-made deposition chamber whose pressure ranged from 10^{-6} to 10^{-8} torr during the evaporation. While Si atoms were not introduced deliberately, they were consistently observed as a widely present contaminant both on metal-deposited samples and on pristine graphene samples. The presence of Si (and SiO_x) contaminants on graphene has been widely reported for both CVD-grown and exfoliated graphene[41]. The support films, another possible origin for the Si contaminants, were all but ruled out as a source in our case: Si single atoms and SiO_x clusters were indeed consistently observed on as-prepared pristine graphene samples transferred onto different types of support grids (lacey carbon film, holey carbon film and Quantifoil™) purchased from different suppliers.

All electron micrographs were acquired at the SuperSTEM Laboratory on a Nion UltraSTEM100™ dedicated scanning transmission electron microscope equipped with a cold field emission gun with a native energy spread of 0.35 eV and operated at 60 kV to prevent knock-on damage to the graphene samples. This instrument has an ultra-high-vacuum (UHV) design throughout, allowing pressures at the sample of below $5x10^{-9}$ torr. The beam was set up to a convergence semi-angle of 30 mrad with an estimated beam current of 45 pA at the sample. In these operating conditions the estimated probe size is 1.1 Å. The high angle annular dark field (HAADF) detector used to record the Z-contrast images had inner and outer radii of 86 mrad and 190 mrad respectively. Detectors with lower inner angles (medium and low angle annular dark field detectors, MAADF and LAADF) can provide an increased signal-to-noise in images of low atomic number materials while retaining good signal interpretability for ultra thin samples (there is no dynamical effect for samples one atom thick) and they have been used recently to great effect for atom-by-atom chemical analysis.[47] As this study is concerned with impurity atoms deposited on top of the graphene samples, HAADF imaging was used throughout to avoid potential non-linearity effects in MAADF images, thus retaining the approximate Z^2 dependence of the imaging process whereby the intensity recorded with the probe positioned on an atomic site is approximately proportional to the square of the average atomic number Z of this site.[47] Electron energy loss spectra were recorded on a Gatan

Enfina spectrometer with acquisition times between 1 s and 2 s (as specified in the text) for point spectra. The spectrometer acceptance semi-angle was calibrated at 33 mrad.

Interactions between graphene and silicon adatom (clusters) or Si_xO_y clusters were further studied using a first-principles calculation method implemented in the SIESTA code,[48] as was done in previous work.[25, 26, 40] In modelling these interactions, the generalized gradient approximation (GGA-PBE)[49] was adopted to describe the exchange-correlation energy, which has been used in understanding graphene destruction[26] and oxidation.[25, 40] Another theoretical consideration is the interaction between graphene and a quartz substrate. In this case, the local density approximation (LDA)[50] instead of the GGA-PBE is used because the latter fails to describe the weak graphene-substrate interactions.[51] The atomic positions were fully relaxed within the maximum force of 0.04 eV/Å on individual atoms. The ion cores are described by norm-conserving non-relativistic pseudo-potentials[52] with cut off radii 1.90, 1.15 and 1.25 a.u. for Si, O and C respectively, and the wavefunctions are expanded with localized atomic orbitals (a double-ζ plus polarization basis set). All calculations were carried out with an energy mesh cut-off of 360 Ry. We used a rectangular shaped supercell containing 48 carbon atoms to model interactions between graphene and silicon atoms or clusters.[40] For the modelling of the interaction of graphene with an un-passivated quartz (ordered SiO_2) surface we used a graphene supercell containing 32 carbon atoms over 9 Si atomic layers of α-quartz previously used in Ref. [51]. For these two models we used the k-point mesh of 8×6×1 and 4×4×1 in the Monkhorst-Pack scheme[53] respectively.

Acknowledgments

This work was supported by the EPSRC (UK). We acknowledge computational support from the CAC of KIAS. Y.-W. S. was supported by the NRF grant funded by the government of Korea, MEST (Quantum Metamaterials Research Center, R11-2008-053-01002-0).

References

1. Novoselov, K. S.; Geim, A. K.; Morozov, S. V.; Jiang, D.; Zhang, Y.; Dubonos, S. V.; Grigorieva, I. V.; Firsov, A. A. Electric Field Effect in Atomically Thin Carbon Films. *Science* **2004,** 306, 666-669.

2. Ponomarenko, L. A.; Geim, A. K.; Zhukov, A. A.; Jalil, R.; Morozov, S. V.; Novoselov, K. S.; Grigorieva, I. V.; Hill, E. H.; Cheianov, V. V.; Falko, V. I.; *et al.*

Tunable Metal-Insulator Transition in Double-Layer Graphene Heterostructures. *Nat. Phys.* **2011,** 7, 958-961.
3. Pi, K.; McCreary, K. M.; Bao, W.; Han, W.; Chiang, Y. F.; Li, Y.; Tsai, S. W.; Lau, C. N.; Kawakami, R. K. Electronic Doping and Scattering by Transition Metals on Graphene. *Phys. Rev. B* **2009,** 80, 075406.
4. Venugopal, A.; Colombo, L.; Vogel, E. M. Contact Resistance in Few and Multilayer Graphene Devices. *Appl. Phys. Lett.* **2010,** 96, 013512.
5. Dimiev, A.; Kosynkin, D. V.; Sinitskii, A.; Slesarev, A.; Sun, Z.; Tour, J. M. Layer-by-Layer Removal of Graphene for Device Patterning. *Science* **2011,** 331, 1168-1172.
6. Campos, L. C.; Manfrinato, V. R.; Sanchez-Yamagishi, J. D.; Kong, J.; Jarillo-Herrero, P. Anisotropic Etching and Nanoribbon Formation in Single-Layer Graphene. *Nano Lett.* **2009,** 9, 2600-2604.
7. Ci, L.; Xu, Z.; Wang, L.; Gao, W.; Ding, F.; Kelly, K.; Yakobson, B.; Ajayan, P. Controlled Nanocutting of Graphene. *Nano Res.* **2008,** 1, 116-122.
8. Booth, T. J.; Pizzocchero, F.; Andersen, H.; Hansen, T. W.; Wagner, J. B.; Jinschek, J. R.; Dunin-Borkowski, R. E.; Hansen, O.; Boggild, P. Discrete Dynamics of Nanoparticle Channelling in Suspended Graphene. *Nano Lett.* **2011,** 11, 2689-2692.
9. Severin, N.; Kirstein, S.; Sokolov, I. M.; Rabe, J. P. Rapid Trench Channeling of Graphenes with Catalytic Silver Nanoparticles. *Nano Lett.* **2008,** 9, 457-461.
10. Schaffel, F.; Warner, J.; Bachmatiuk, A.; Rellinghaus, B.; Buchner, B.; Schultz, L.; Rummeli, M. Shedding Light on the Crystallographic Etching of Multi-Layer Graphene at the Atomic Scale. *Nano Res.* **2009,** 2, 695-705.
11. Schaffel, F.; Wilson, M.; Bachmatiuk, A.; Rummeli, M. H.; Queitsch, U.; Rellinghaus, B.; Briggs, G. A. D.; Warner, J. H. Atomic Resolution Imaging of the Edges of Catalytically Etched Suspended Few-Layer Graphene. *ACS Nano* **2011,** 5, 1975-1983.
12. Gao, L.; Ren, W.; Liu, B.; Wu, Z.-S.; Jiang, C.; Cheng, H.-M. Crystallographic Tailoring of Graphene by Nonmetal SiOx Nanoparticles. *J. Am. Chem. Soc.* **2009,** 131, 13934-13936.
13. Biró, L. P.; Lambin, P. Nanopatterning of Graphene with Crystallographic Orientation Control. *Carbon* **2010,** 48, 2677-2689.
14. Chan, K. T.; Neaton, J. B.; Cohen, M. L. First-Principles Study of Metal Adatom Adsorption on Graphene. *Phys. Rev. B* **2008,** 77, 235430.
15. Sevincli, H.; Topsakal, M.; Durgun, E.; Ciraci, S. Electronic and Magnetic Properties of 3d Transition-Metal Atom Adsorbed Graphene and Graphene Nanoribbons. *Phys. Rev. B* **2008,** 77, 195434.
16. Giovannetti, G.; Khomyakov, P. A.; Brocks, G.; Karpan, V. M.; van den Brink, J.; Kelly, P. J. Doping Graphene with Metal Contacts. *Phys. Rev. Lett.* **2008,** 101, 026803.
17. Gong, C.; Lee Geunsik; Shan, B.; Vogel, E., M. ; Wallace, R. M.; Cho, K. First-Principles Study of Metal-Graphene Interfaces. *J. Appl. Phys* **2010,** 108, 123711.
18. Vanin, M.; Mortensen, J. J.; Kelkkanen, A. K.; Garcia-Lastra, J. M.; Thygesen, K. S.; Jacobsen, K. W. Graphene on Metals: A van der Waals Density Functional Study. *Phys. Rev. B* **2010,** 81, 081408.

19. Yazyev, O. V.; Pasquarello, A. Metal Adatoms on Graphene and Hexagonal Boron Nitride: Towards Rational Design of Self-Assembly Templates. *Phys. Rev. B* **2010,** 82, 045407.
20. Zólyomi, V.; Rusznyák, Á.; Koltai, J.; Kürti, J.; Lambert, C. J. Functionalization of Graphene with Transition Metals. *Phys. Status Solidi B* **2010,** 247, 2920-2923.
21. Liu, X.; Wang, C. Z.; Yao, Y. X.; Lu, W. C.; Hupalo, M.; Tringides, M. C.; Ho, K. M. Bonding and Charge Transfer by Metal Adatom Adsorption on Graphene. *Phys. Rev. B* **2011,** 83, 235411.
22. Zan, R.; Bangert, U.; Ramasse, Q.; Novoselov, K. S. Metal-Graphene Interaction Studied via Atomic Resolution Scanning Transmission Electron Microscopy. *Nano Lett.* **2011,** 11, 1087-1092.
23. Krasheninnikov, A. V.; Lehtinen, P. O.; Foster, A. S.; Pyykko; P.; Nieminen, R. M. Embedding Transition-Metal Atoms in Graphene: Structure, Bonding, and Magnetism. *Phys. Rev. Lett.* **2009,** 102, 126807.
24. Okamoto, Y. Density-Functional Calculations of Icosahedral M13 (M = Pt and Au) Clusters on Graphene Sheets and Flakes. *Chem. Phys. Lett.* **2006,** 420, 382-386.
25. Boukhvalov, D. W.; Katsnelson, M. I. Chemical Functionalization of Graphene with Defects. *Nano Lett.* **2008,** 8, 4373-4379.
26. Boukhvalov, D. W.; Katsnelson, M. I., Destruction of Graphene by Metal Adatoms. *Appl. Phys. Lett.* **2009,** 95, 023109.
27. Gass, M. H.; Bangert, U.; Bleloch, A. L.; Wang, P.; Nair, R. R.; Geim, A. K. Free-Standing Graphene at Atomic Resolution. *Nat. Nanotechnol.* **2008,** 3, 676-681.
28. Egerton, R. F.; Wang, F.; Crozier, P. A. Beam-Induced Damage to Thin Specimens in an Intense Electron Probe. *Microsc. Microanal.* **2006,** 12, 65-71.
29. Li, X.; Cai, W.; An, J.; Kim, S.; Nah, J.; Yang, D.; Piner, R.; Velamakanni, A.; Jung, I.; Tutuc, E.; *et al.* R. S., Large-Area Synthesis of High-Quality and Uniform Graphene Films on Copper Foils. *Science* **2009,** 324, 1312-1314.
30. Zan, R.; Bangert, U.; Ramasse, Q.; Novoselov, K. S. Evolution of Gold Nanostructures on Graphene. *Small* **2011,** 7, 2868-2872.
31. Akturk, U., Olcay; Tomak, M. Au_nPt_n Clusters Adsorbed on Graphene Studied by First-Principles Calculations. *Phys. Rev. B* **2009,** 80, 085417.
32. Neek-Amal, M.; Asgari, R.; Tabar, M. R. R. The Formation of Atomic Nanoclusters on Graphene Sheets. *Nanotechnology* **2009,** 20, 135602.
33. Girit, C. O.; Meyer, J. C.; Erni, R.; Rossell, M. D.; Kisielowski, C.; Yang, L.; Park, C.-H.; Crommie, M. F.; Cohen, M. L.; Louie, S. G.; *et al.* Graphene at the Edge: Stability and Dynamics. *Science* **2009,** 323, 1705-1708.
34. Raub, C. J. Electroplating of Palladium for Electrical Contacts. *Platinum Met. Rev.* **1982,** 26, 158-166.
35. Xia, F.; Perebeinos, V.; Lin, Y.-m.; Wu, Y.; Avouris, P. The Origins and Limits of Metal-Graphene Junction Resistance. *Nat. Nanotechnol.* **2011,** 6, 179-184.
36. Cabria, I.; Lopez, M. J.; Alonso, J. A. Theoretical Study of the Transition from Planar to Three-Dimensional Structures of Palladium Clusters Supported on Graphene. *Phys. Rev. B* **2010,** 81, 035403.

37. Ao, Z. M.; Jiang, Q.; Zhang, R. Q.; Tan, T. T.; Li, S. Al Doped Graphene: A Promising Material for Hydrogen Storage at Room Temperature. *J. Appl. Phys.* **2009,** 105, 074307.
38. Wang, X.; Tabakman, S. M.; Dai, H. Atomic Layer Deposition of Metal Oxides on Pristine and Functionalized Graphene. *J. Am. Chem. Soc.* **2008,** 130, 8152-8153.
39. Boyen, H. G.; Kastle, G.; Weigl, F.; Koslowski, B.; Dietrich, C.; Ziemann, P.; Spatz, J. P.; Riethmuller, S.; Hartmann, C.; Moller, M.; *et al.* Oxidation-Resistant Gold-55 Clusters. *Science* **2002,** 297, 1533-1536.
40. Boukhvalov, D. W.; Son, Y.-W., Oxygen Reduction Reactions on Pure and Nitrogen-Doped Graphene: a First-Principles Modeling. *Nanoscale* **2012**. 4, 417-420.
41. Zhou, W.; Prange, M.; Oxley, M.; Pantelides, S.; Pennycook, S.; Nanda, J.; Narula, C.; Idrobo, J. C. Atomic Scale Study of Point Defects in Graphene using STEM. *Microsc. Microanal.* **2011,** 17, (SupplementS2), 1498-1499.
42. Banhart, F.; Kotakoski, J.; Krasheninnikov, A. V. Structural Defects in Graphene. *ACS Nano* **2011,** 5, 26-41.
43. Li, J.-L.; Kudin, K. N.; McAllister, M. J.; Prud'homme, R. K.; Aksay, I. A.; Car, R. Oxygen-Driven Unzipping of Graphitic Materials. *Phys. Rev. Lett.* **2006,** 96, 176101.
44. Tribaudino, M.; Artoni, A.; Mavris, C.; Bersani, D.; Lottici, P. P.; Belletti, D. Single-Crystal X-ray and Raman Investigation on Melanophlogite from Varano Marchesi (Parma, Italy). *Am. Mineral.* **2008,** 93, 88-94.
45. Balandin, A. A.; Ghosh, S.; Bao, W.; Calizo, I.; Teweldebrhan, D.; Miao, F.; Lau, C. N. Superior Thermal Conductivity of Single-Layer Graphene. *Nano Lett.* **2008,** 8, 902-907.
46. Meyer, J. C.; Geim, A. K.; Katsnelson, M. I.; Novoselov, K. S.; Obergfell, D.; Roth, S.; Girit, C.; Zettl, A. On the Roughness of Single- and Bi-Layer Graphene Membranes. *Solid State Commun.* **2007,** 143, 101-109.
47. Krivanek, O. L.; Chisholm, M. F.; Nicolosi, V.; Pennycook, T. J.; Corbin, G. J.; Dellby, N.; Murfitt, M. F.; Own, C. S.; Szilagyi, Z. S.; Oxley, M. P.; *et al.* Atom-By-Atom Structural and Chemical Analysis by Annular Dark-Field Electron Microscopy. *Nature* **2010,** 464, 571-574.
48. Soler, J. M.; Artacho, E.; Gale, J. D.; Garcia, A.; Junquera, J.; Ordejon, P.; Sanchez-Portal, D. The SIESTA Method for Ab Initio Order- N Materials Simulation. *J. Phys. Condens. Matter* **2002,** 14, 2745.
49. Perdew, J. P.; Burke, K.; Ernzerhof, M. Generalized Gradient Approximation Made Simple. *Phys. Rev. Lett.* **1996,** 77, 3865-3868.
50. Perdew, J. P.; Zunger, A. Self-Interaction Correction to Density-Functional Approximations for Many-Electron Systems. *Phys. Rev. B* **1981,** 23, 5048-5079.
51. Cuong, N. T.; Otani, M.; Okada, S. Semiconducting Electronic Property of Graphene Adsorbed on (0001) Surfaces of SiO_2. *Phys. Rev. Lett.* **2011,** 106, 106801.
52. Troullier, N.; Martins, J. L. Efficient Pseudopotentials for Plane-Wave Calculations. *Phys. Rev. B* **1991,** 43, 1993-2006.
53. Monkhorst, H. J.; Pack, J. D. Special Points for Brillouin-Zone Integrations. *Phys. Rev. B* **1976,** 13, 5188-5192.

Supporting Information

All TEM samples were screened in a conventional TEM (Tecnai F30) prior to metal evaporation to assess the quality of graphene coverage of the grids and to identify the number of layers by using electron diffraction.

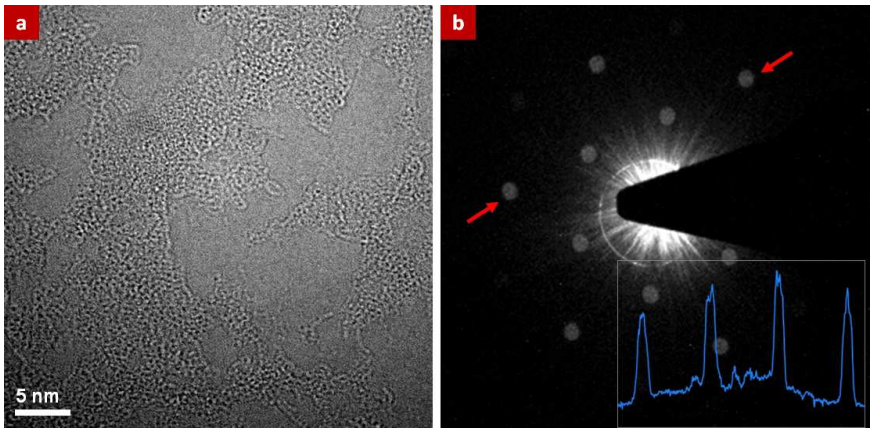

Figure S1. Bright field HRTEM image (a) and diffraction pattern (b) from the imaged area of a graphene sample prior to metal deposition. The intensity profile in the inset is taken between the two red arrows as indicated and confirms the presence of monolayer graphene.

Over 90% of the surface of the samples was consistently identified as a monolayer by comparing first and second ring spot intensities in the diffraction pattern, as illustrated in figure S1.

Holes were observed to form under the beam at the edge of the contamination layer where the deposited metals (0.2nm of Ni, Pd, Ti or Al) sit preferentially. These contamination layers are believed to be due in part to carbonaceous residues from the wet chemistry methodology used to transfer the graphene layers onto TEM grids, but mostly to post-transfer exposure of the graphene to air[1]. This drilling/etching behaviour is extremely dynamic and was captured as time series with large numbers of consecutive images with very short pixel times. Many such series were acquired for all metal deposited samples: Figure S2 illustrates the process with stills from a series of images of Ni-mediated drilling. The initial hole (top) can be seen to open up all along the metal clusters with single metal atoms decorating its edges before being 'drilled' away.

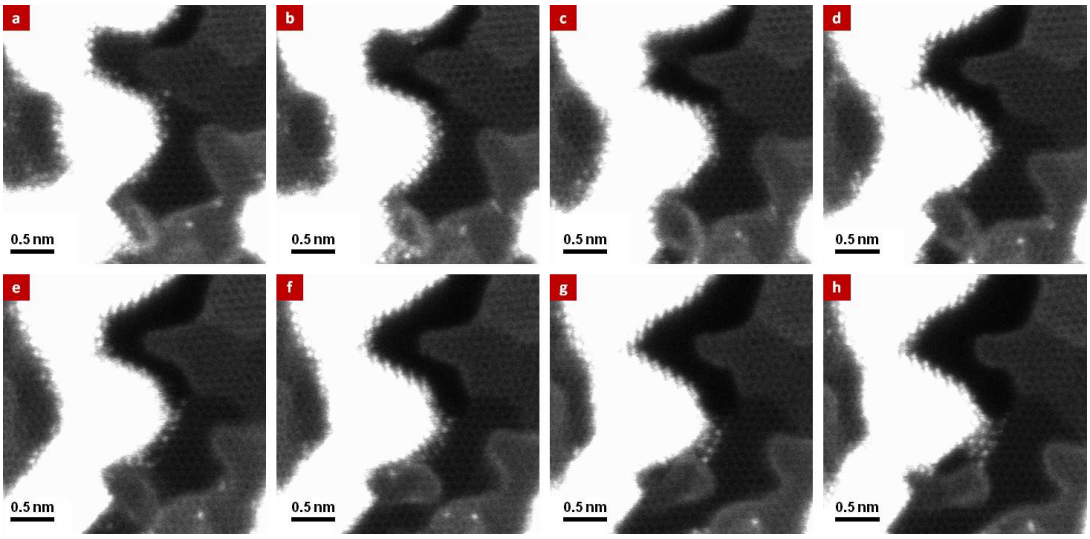

Figure S2. Stills from a time series showing the metal-mediated formation of hole at the edge of a Ni cluster. The time elapsed between each image (a)-(h) is approximately 5s. To improve signal-to-noise, the images shown are the sum of 10 consecutive members of the time series.

The drilling or etching behaviour continues as long as new metal atoms jump to the edge of the holes from the neighbouring clusters, which act as a reservoir. The images in figure S3 are taken from another time series from the Pd-deposited sample. The hole is initially enlarged, with bright atoms decorating its edges jumping from the neighbouring cluster (figure S3(a)). This jumping process is too fast to be captured in a single frame, even with short pixel dwell times, so a detailed analysis of the atomic movement is difficult to provide. But bright horizontal streaks in the images, corresponding to the same atom being captured at different positions by the beam along a line, provide evidence of these jumps[1] and show that the metal atoms can travel at least a few nm within a single image line (a few ms). After a few seconds, the size of the hole stabilises (figure S3(b)) as the reservoir of mobile ad-atoms is exhausted. The dotted outlines on figure S3 (b) and (c) illustrate how the edges of the hole then simply reconfigure without any further expansion, in spite of the long time elapsed (40s between fig. S3 (b) and (c)).

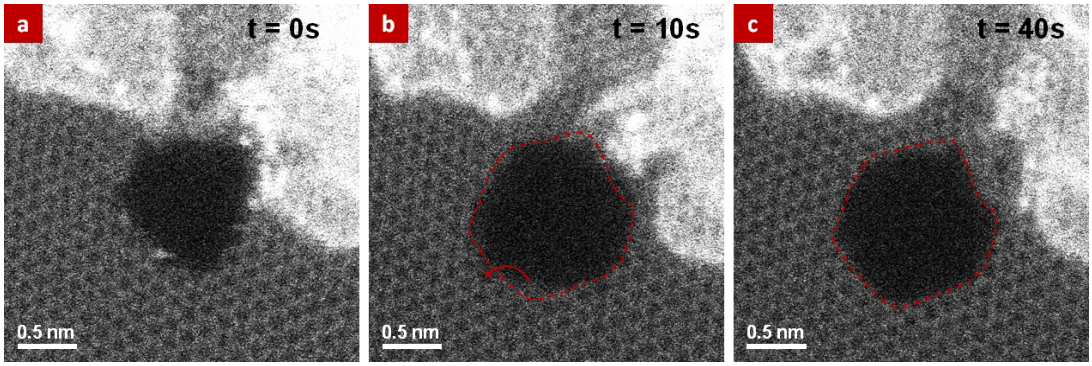

Figure S3. (a) A hole formed in monolayer graphene at the edge of a Pd cluster is further enlarged as metal atoms jump onto the exposed edge, until the reservoir of impurity atoms is exhausted (b), approximately 10s later. The hole merely reshapes dynamically (c) in spite of a further 40 scans (approximately 20s), as indicated by the dotted outline of the hole and the arrow.

The type of metal mediating the etching process did not appear to influence the shapes of the holes formed, nor the speed or ease with which their sizes grew. Such relationships may not be entirely ruled out but the variations in metal cluster sizes and distribution, and more generally the large number of parameters that would need to be controlled (exact size of the clean graphene patch being drilled, geometry of the contamination patch, proximity to the edge of the metal reservoir, etc...) make it difficult to draw any statistically significant conclusion.

This metal mediated etching was observed for all studied metals with the exception of Au, in spite of extensive observations due to the importance of Au as a potential contact in the metal-graphene system[3]. Figure S4 shows simultaneously acquired bright field and HAADF STEM images of Au-evaporated monolayer graphene, obtained in conditions identical to the other metal-deposited samples, but showing no hole formation.

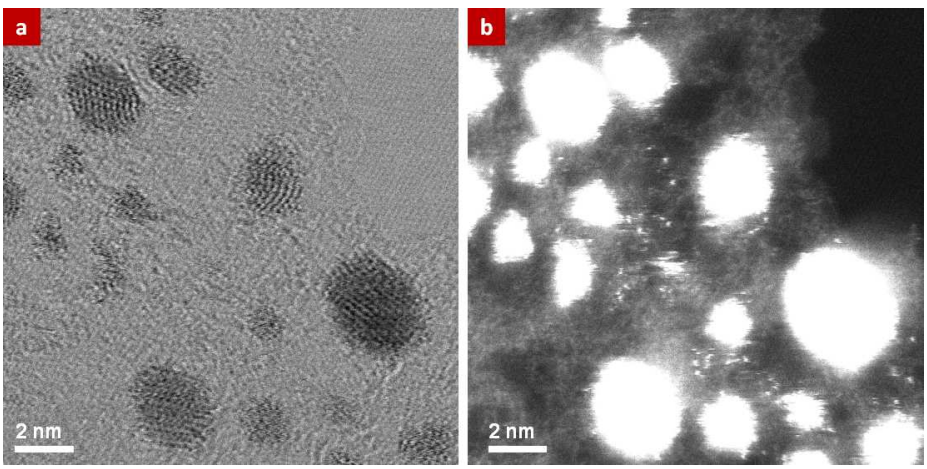

Figure S4. Bright field (a) and HAADF (b) images of Au-evaporated monolayer graphene, observed in the same conditions as all other metal-deposited samples. No hole formation was observed with Au.

Although the destruction of graphene by metal ad-atoms was predicted by theoretical calculations in the literature[4], we also observed this etching process on 'pristine' samples, consisting of monolayer graphene processed in identical conditions but on which no metal was deposited. In this case, Si atoms were found to decorate the holes and to mediate their formation. Si/SiO_2 are commonly found contaminants on pristine graphene[5] but were not previously thought of as potentially deleterious. Additional calculations were thus carried out to shed light on this behaviour.

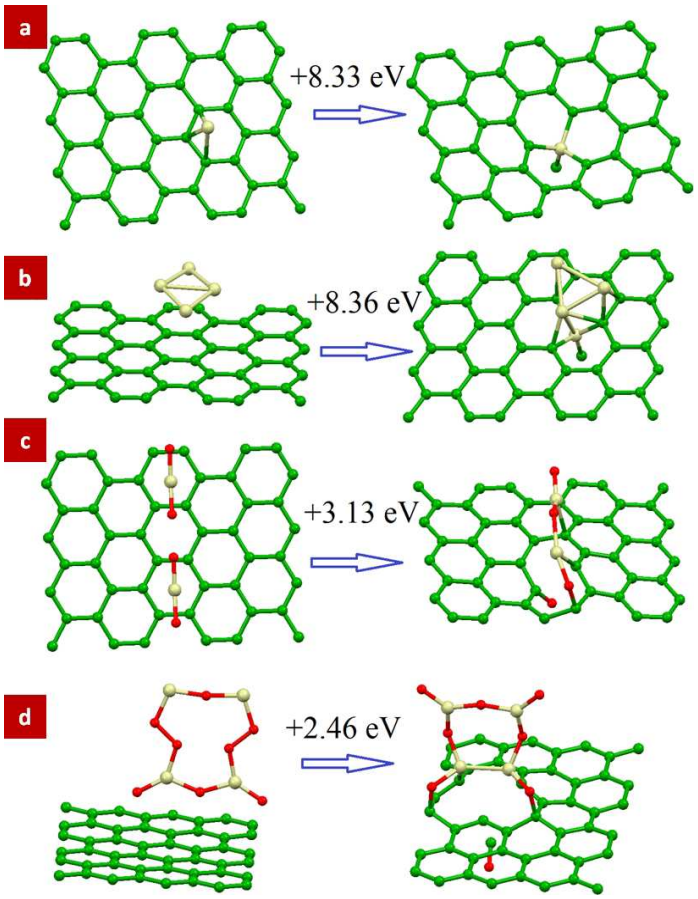

Figure S5. Optimised atomic structure and energetics for initial (left column) and final (right column) steps of the formation of C vacancies in the presence of (a) a single Si atom, (b) a metallic Si cluster, (c) a SiO_2 molecule and (d) a SiO_2 cluster.

When modelling the formation of vacancies in graphene in the presence of a single silicon ad-atom (Fig. S5(a)) or of a pure silicon cluster (fig. S5(b)), we calculated that the

energies required for are in both cases higher than the energy required for the formation of a single vacancy by mere irradiation (about 7 eV). Any mechanism involving pure Si is therefore unlikely to result in the drilling behaviour we observed and it can be concluded that pure silicon is safe for graphene.

Another model involves the possible migration of oxygen atoms from unpassivated quartz (arising from the sample preparation) to the graphene surface. The energy required here for the activation of graphene with the formation of a carbon monoxide molecule is for a single epoxy group 6.94 eV, and 9.69 eV for a pair of epoxy groups[6]. Again, these calculations suggest that perfect SiO_2 is rather safe for graphene.

Lastly we modelled the vacancy formation energy in the presence of disordered silicon oxide, either in the form of SiO_2 molecules (fig. S5c) or of SiO_2-based loose clusters (fig. S5d). The energies required here are much lower and the interaction of graphene with the non-stoichiometric surface of SiO_2 nanoparticles could provide a path for the formation of metastable $Si_xO_yC_z$ structures and thus the unzipping of the graphene structure.

References

1. van Dorp, W.F.; Zhang, X.; Feringa, B.L.; Wagner, J.B.; Hansen, T.W.; De Hosson, J.Th.M. Nanometer-Scale Lithography on Microscopically Clean Graphene, *Nanotechnology* **2011,** 22, 505303.
2. Krivanek, O.L.; Dellby, N.; Murfitt, M.F.; Chisholm, M.F.; Pennycook, T.J.; Suenaga, K.; Nicolosi, V. Gentle STEM: ADF Imaging and EELS at Low Primary Energies, *Ultramicroscopy* **2010**, 110, 935-945.
3. Zan, R.; Bangert, U.; Ramasse, Q.; Novoselov, K. S. Evolution of Gold Nanostructures on Graphene. *Small* **2011**, 7(20), 2868–2872.
4. Boukhvalov, D. W.; Katsnelson, M. I. Destruction of Graphene by Metal Adatoms *Applied Physics Letters* **2009,** 95, (2), 023109.
5. Zhou, W.; Prange, M.; Oxley, M.; Pantelides, S.; Pennycook, S.J.; Nanda, J.; Narula, C.; Idrobo, J.-C. Atomic-Scale Study of Point Defects in Graphene Using STEM. *Microscopy and Microanalysis* **2011,** Vol. 17, Suppl. S2, 1498-1499.
6. Boukhvalov, D.W.; Son, Y.-W. Oxygen Reduction Reactions on Pure and Nitrogen-Doped Graphene: a First-Principles Modeling. *Nanoscale* **2012,** 4, (2), 417-420.

Graphene Reknits Its Holes

Recep Zan, Quentin M. Ramasse, Ursel Bangert and Konstantin S. Novoselov

Nano Letters, 2012, 12(8), 3936-3940

ABSTRACT

Nano-holes, etched under an electron beam at room temperature in single-layer graphene sheets as a result of their interaction with metal impurities, are shown to heal spontaneously by filling up with either non-hexagon, graphene-like, or perfect hexagon 2D structures. Scanning transmission electron microscopy was employed to capture the healing process and study atom-by-atom the re-grown structure. A combination of these nano-scale etching and re-knitting processes could lead to new graphene tailoring approaches.

TOC

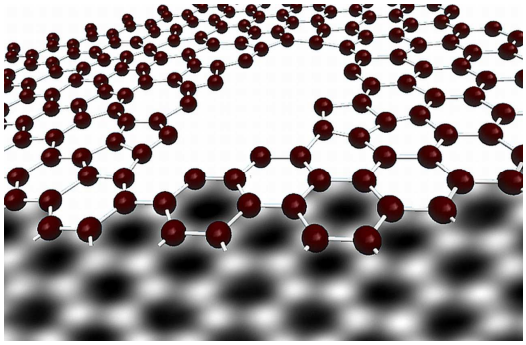

The development of graphene devices has entered a new era: graphene is rapidly moving from the laboratory to the factory floor with an increasing effort directed towards achieving devices that employ suspended membranes as well as graphene of defined geometries, e.g., nano-ribbons and quantum dots, because of their predicted novel, exceptional electronic properties.[77, 78] As a result, the interfaces between graphene and other components of the devices such as metal contacts are under intense scrutiny. We have recently shown that in the presence of metals graphene can be etched on the nano-scale[79,4] under exposure to an electron probe following a sequence of point defect reactions, a process different from previous attempts at graphene etching. In earlier studies,

graphene and graphite were etched or tailored in a gas environment (hydrogen or oxygen) at high temperatures.[35, 38, 39] In particular, the interaction of metals with the graphene surface in such extreme conditions was shown both experimentally[8] and theoretically[9] to provide an efficient means of controlling the etching process and effectively sculpt graphene/graphite nanostructures. A recent review of graphene tailoring and its applications can for instance be found in Xu.[10] Additionally, a number of papers have previously discussed defects in graphene, either following experimental transmission electron microscopy (TEM) studies,[27, 30, 57, 66, 80-82] where defects were introduced by the electron beam, or by simulations based on Density Functional Theory (DFT) calculations.[83-88] Defects studies in all those papers are based on reconstruction of the graphene lattice as a result of knock-on of carbon atoms from the graphene lattice (mono- and multi- vacancy) or/and as a result of bond rotations, e.g., the formation of Stone-Wales (55-77) and 8-ring defects. Dynamics, stability and favourable arrangements of the reconstructed lattice, with the occurrence of larger vacancy aggregates and holes, as well as edge reconstructions thereof, are further aspects of those studies. Furthermore, new structures with long range order, such as haeckelites[19] consisting of 5-, 6- and 7-member rings, or pentaheptides[18] incorporating 5- and 7-member rings, have been proposed as result of theoretical calculations. Here we report the first observations of reconstruction, *i.e.* the mending and filling of many-vacancy holes (over 100 vacancies) in graphene, in an electron microscope. We show that provided a reservoir of loose carbon atoms is readily available nearby, holes in graphene can be re-filled with either non-hexagonal near-amorphous or perfectly hexagonal 2-dimensional structures.

To study atomic arrangements we employ high angle annular dark field (HAADF) imaging in a Nion UltraSTEM100^{TM} aberration-corrected scanning transmission electron microscope (STEM). The microscope was operated in 'Gentle STEM' conditions[26] at 60 keV primary beam energy to prevent knock-on damage to the graphene sheets, even after long intervals of repeated scanning of small areas of a few square nanometers. The ultra-high-vacuum (UHV) design of this instrument allows clean imaging conditions with pressures below $5x10^{-9}$ Torr near the sample. The beam was set up to a convergence semi-angle of 30 mrad with an estimated beam current of 45 pA. In these operating conditions the estimated probe size is 1.1 Å, providing the perfect tool for atom-by-atom chemical analysis[27]. These experimental conditions (scanning probe, low primary beam energy, high vacuum conditions) are significantly different from other studies of the dynamics of defects and edges in graphene, which employ higher beam energies and are typically

carried out in much poorer vacuum conditions.[13,28,29] Samples were obtained by transfer of graphene membranes grown by CVD on copper substrates[15] to TEM grids. Two different metals were deposited by electron beam (Pd) and thermal (Ni) evaporation. Although there is no damage inferred to pristine graphene with a 60 keV electron beam, we have recently demonstrated[3,4] that in the presence of transition-metal or silicon atoms, hole formation does occurs under the e-beam. It is believed that the process occurs due to metal-catalysed dissociation of C-C bonds, which leads to point defect formation. The role of the electron beam in this is mainly to mobilise the metal atoms on graphene, and not to initiate the hole formation in the first place, i.e., by carbon atom displacement. The beam may also act as a local heat source and thus help overcome the defect formation energy barrier.[4] This process is however different from high-temperature TEM observations of graphene using a dedicated hot-stage holder, during which amorphous contaminations layers were shown to either be removed totally,[31] thus cleaning the graphene, or be transformed into crystalline patches.[32]

Here, the resulting defects are enlarged in the presence of further metal atoms, which have migrated under the electron beam to the edge of the incurred hole, upon which the process repeats itself. The nature of the intentionally-deposited metal impurities was confirmed by single-atom sensitive electron energy loss spectroscopy (EELS).[4] When the reservoir of metal atoms is exhausted, the process stops and the hole remains of almost the same size, although the edges undergo repeated reconstruction in consecutive scans. If metal impurities are not present and, at the same time, carbon atom supply is warranted, e.g. through near-by hydrocarbon contamination attracted towards the hole by the scanning probe, ‘filling’ occurs and the hole mends itself by non-hexagon arrangements. However, if no hydrocarbon contamination is present, healing can occur *via* reconstruction of the perfect graphene hexagon structure. The following Z-contrast images depict the hole evolution and two filling scenarios, by non-hexagon and by hexagon structures, in freely suspended graphene films where heavier foreign atoms are present either as residual impurities or as a consequence of metal evaporation.

The deposition of metal atoms on CVD-grown graphene results in the formation of nm-sized metal clusters sitting preferentially on patches of C-based surface contamination, ubiquitous in suspended graphene membranes.[33] Pd atoms, dislodged from a nearby Pd cluster by the electron beam and 'dragged' across the sample until they settle in a new stable position as the beam is being scanned, can be seen in fig. 1a to decorate a hole in graphene. Newly arriving Pd atoms lead to hole expansion (fig 1b), whereas in the absence

of metal atoms the hole formation slows down and edge reconstruction takes place under the electron beam (fig. 1c). Furthermore, figure 1 shows that the hole is bordered by hydrocarbon contamination, which constitutes the carbon reservoir for the hole healing described below.

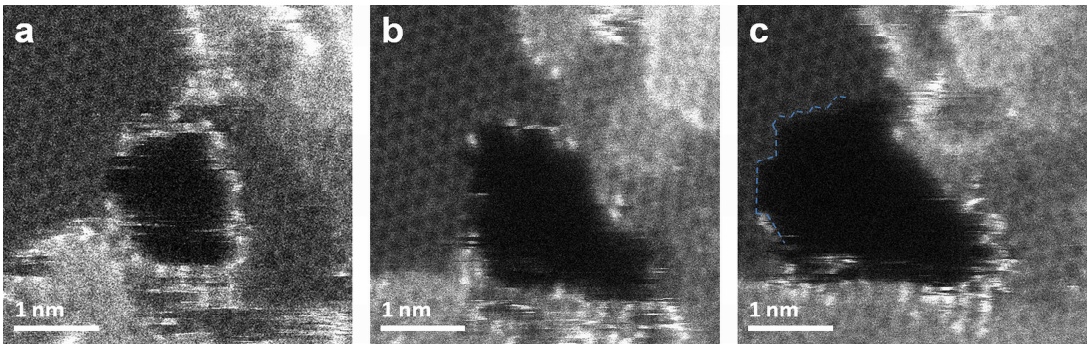

Figure 1. Atomic resolution HAADF images (raw data) from consecutive scans of suspended graphene, showing a) an etched hole decorated with Pd atoms; b) the enlargement of the hole following further supply of Pd atoms; c) the stabilization of the hole size in the absence of Pd atoms at the edge.

Figure 2 shows the same hole as in fig. 1. after the metal reservoir has been mostly exhausted. The hole then starts to heal with carbon atoms being supplied by the contamination patches (light grey features at the top and bottom of fig. 1 and 2). The image in figure 2a was taken after that in fig. 1c and illustrates the start of the healing process. The blue dotted line in fig. 2d shows the border of the hole at the pre-healing stage (immediately after fig. 1c was acquired). After a subsequent scan the hole has filled completely with what can be described as a 2-dimensional amorphous carbon patch (fig. 2b), constituted almost randomly of 5, 6-, 7- and even 8-member rings. Notably 5-7-/ 8-member ring pairs can arise from dissociation of lattice vacancies and constitute dislocation dipoles.[20] Additional impurity atoms are also captured within this newly-formed 'net': bright atoms are clearly seen on fig. 2a and 2b. Figure 2c is of a subsequent scan of the same area as in figs 2a and b. The deposition of carbon ad-atoms, which are dragged out of the hydrocarbon contamination by the scanning beam can be seen from slightly lighter patches and streaks on the carbon rings in fig. 2c, making atomic position identification slightly more difficult. Nevertheless, a redistribution of the defects is noticeable, indicating bond rotation during the scan: notably in fig. 2c the carbon atoms have re-organized themselves solely into 5-7 rings while the more unstable 8-member ring

structure has disappeared. The bottom row images are the same as in the top row but in order to reduce the noise levels and to improve the accuracy of the image analysis (to show the carbon-atom 'network' more clearly), a probe deconvolution algorithm based on maximum entropy methods was applied to the raw Z-contrast images. This algorithm also has the advantage of removing the contribution of the tails of the focussed electron probe to the neighbouring atom intensities, which is essential for quantitative contrast analysis.[27,34] This sequence of images shows clearly that the faults in the reconstructed graphene do not arise from damage by the e-beam, but are grown-in features as a result of an 'epitaxial'-like growth. The incorporation of sets of 5-, 6- and 7-member rings structures, called Haeckelites, into highly defected graphene was suggested by Terrones et al.[19] but had never been observed experimentally hitherto. Figure 2 shows clearly that this kind of structure can exist in suspended form although they form here an amorphous patch rather than organising themselves into an ordered array of polygons.

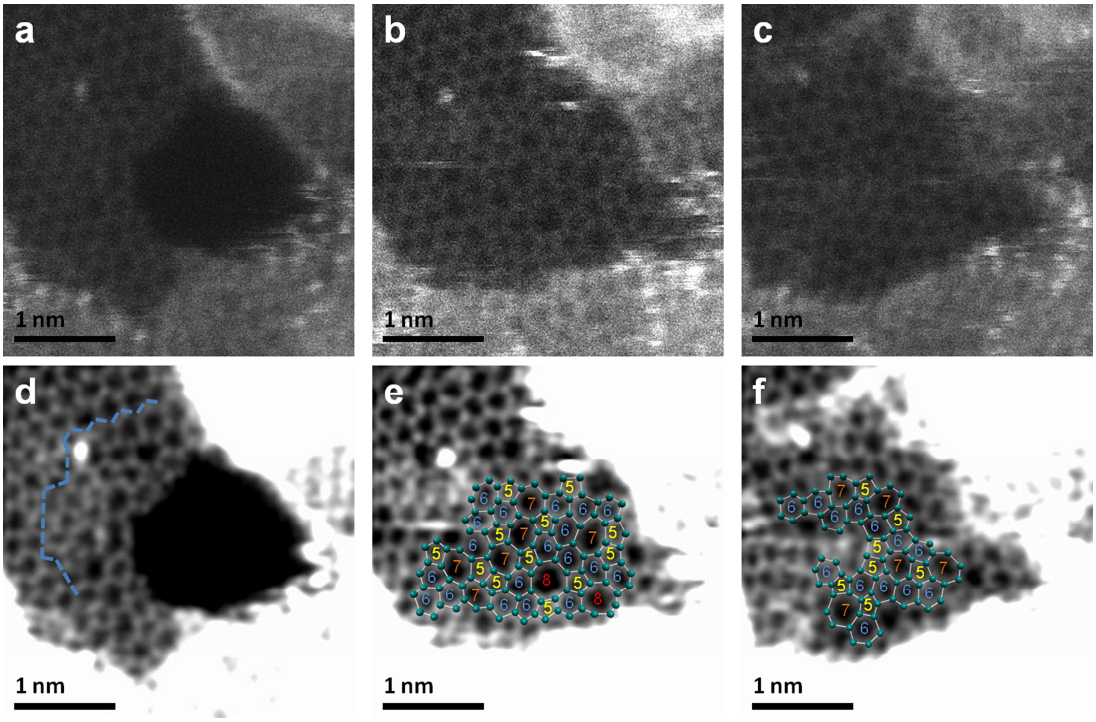

Figure 2. Atomic resolution Z-contrast images illustrating the hole filling process in suspended graphene. a) a hole created at the border of hydrocarbon contamination b) complete reconstruction with incorporation of 5-7 rings and two 5-8 rings, and c) redistribution of defects in the 'mended' region, by 5-7 rings. Images d-f are processed versions of a-c. A maximum entropy deconvolution algorithm was used and the contrast was optimised to visualise the carbon atoms. The carbon atom positions are highlighted by light green dots and polygons numbered according to the number of atoms in the rings.

Such 2-dimensional near-amorphous carbon layers can also grow 'epitaxially' on graphene, as illustrated on figure 3. After long observations of the same area of single layer graphene (more than 40 minutes of observation in this case) some contamination can occasionally 'creep in' and cover the graphene sheet. The circled region on figure 3a is a single additional carbon layer (as can be clearly deduced from the contrast in the image), which has formed on top of the clean, underlying (dark) graphene patch after repeated scanning. The presence of a Moiré pattern indicates that this additional layer has a similar structure to the underlying graphene, but the patter is highly irregular and interrupted (as highlighted by the arrows), unlike the patterns observed in pure Bernal-stacked graphene.[35]

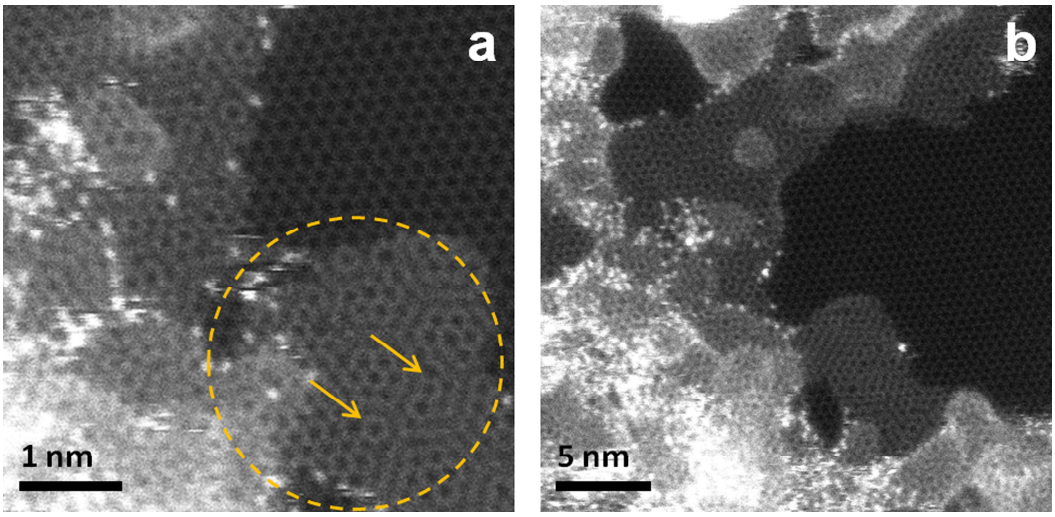

Figure 3. Atomic resolution HAADF image (raw data) obtained after repeated scanning of the same area; the circled area is an additional one-atom-thick carbon layer that has grown 'epitaxially' as a result of carbon atom supply from the hydrocarbon contamination surrounding the pristine graphene patch. The Moiré pattern, however, is non-regular (arrow), indicating the existence of random defected carbon ring networks in the newly-grown layer as well as in the already existing contamination.

The newly-grown layer must therefore be heavily faulted. It likely contains a high density of 5- and 7-member rings, similar to the 're-knitted' layer in fig 2b. This can again be interpreted as an amorphous 2-dimensional layer with some degree of short-range graphene-like order. The re-grown structures in figs. 2 and 3 provide a remarkable glimpse into the atomic arrangements of amorphous carbon structures; they show the precise atomic arrangements of a 2-D amorphous carbon material.[15] By close inspection of atomic resolution Z-contrast images of graphene films it can then be concluded that a large

fraction of the ubiquitous contamination (such as the lighter patches in fig. 3b) where material deposited on graphene sits preferentially, consists of stacks of these amorphous mono-layer carbon films.

By contrast, when a small hole is created away from the hydrocarbon contamination, the self-healing mechanism appears to lead to the formation of perfect hexagons. Two holes are apparent in fig. 4a, both created as a result of Ni-atom mediated graphene etching. The small hole was created when Ni atoms from the edge of the larger hole, which had formed earlier, were dislodged by the electron beam and 'dragged' onto a clean patch of graphene where the etching was initiated, through the e-beam scanning motion. In subsequent scans, after cessation of the migration of metal atoms to its edges, the small hole is observed to fill up with perfect carbon hexagons (fig. 4b). This 're-knitting' process happened within a much shorter time span (less than 10 seconds: two consecutive scans) compared to the previous case (figs. 1&2). Impurity atoms are again trapped within the newly formed lattice, such as the brighter atom indicated in fig. 4b by an arrow. After the contribution of the electron probe 'tails' to the raw HAADF images has been removed (using for instance a maximum-entropy-based probe deconvolution algorithm[34]), a careful comparison of atomic intensities vs. atomic number Z with the model value of $Z^{1.7}$ for HAADF imaging (in our experimental conditions) can enable the chemical identification of these impurities.[27] Figure 4c shows a histogram of the frequency of occurrence of atoms versus their HAADF intensity in the vicinity of the bright atom in Fig. 4b, obtained from the deconvoluted image in the inset in fig. 4c. The positions of the intensity maxima are in the ratio of 1:1.66, which is close to the $Z^{1.7}$ ratios for Z = 6 (C) and Z = 8 (O), of 1:1.63. Although there is only one such impurity in this image (and the statistics are therefore low) this is a good indication that the brighter atom is likely oxygen.

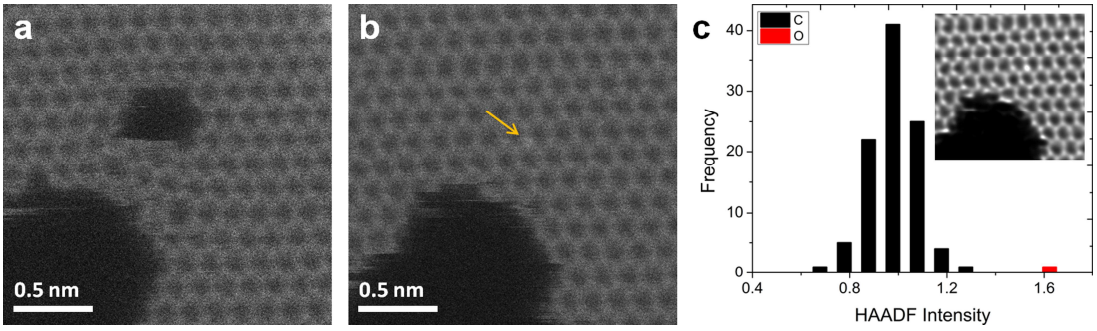

Figure 4. Atomic resolution HAADF images (raw data) from subsequent scans of suspended graphene, showing a) two holes as result of Ni-mediated etching, b) complete

reconstruction of small hole with perfect hexagon graphene structure. c) histogram of the atom intensities, in the vicinity of the brighter atom: the analysis was carried out after processing image 4b with a probe deconvolution algorithm (inset).

The size of the hole to fill is an obvious difference with the previous case and may explain the formation of perfect hexagons: arguably, defects are less likely to form across such a short growth distance. Moreover, the larger distance from the contamination reservoir and the proximity to a much larger perforation in the graphene sheet may also play a role. Edges in graphene are known to be more unstable even at low voltages[13,16]: atoms ejected from the edge of this larger neighbouring hole may have been captured during the re-knitting while the long edge may have reconfigured to accommodate the newly formed material into the usual, energetically favourable honeycomb pattern. Additionally, using a low primary beam energy (60 keV), clean vacuum conditions ($<5x10^{-9}$ Torr) to reduce the ionization damage probability, and a scanning probe, can help explaining our observations of hole-filling, which contrast with previous reports of hole-expansion at 80 keV with a stationary beam.[13,29]

In conclusion, etching of graphene occurs in the presence of metals; when the metal atom supply ceases graphene reconstructs its holes by forming perfect hexagonal or polygonal, *i.e.* 5-, 6-, 7- and 8-member ring structures, which can exist either in suspended form or grow 'epitaxially' on top of clean graphene. Carbon atoms knocked out from neighbouring edges, or supplied by nearby hydrocarbon contamination patches, are incorporated into the holes in a remarkable re-knitting process. This observation of self-healing of graphene might open up possibilities for the use of e-beam techniques in tailoring graphene in a ‘bottom-up’ fashion *via* nano-scale-controlled etching and epitaxial growth from sheet edges.

References

1. Geim, A. K.; Novoselov, K. S. *Nat Mater* **2007,** 6, (3), 183-191.
2. Ponomarenko, L. A.; Geim, A. K.; Zhukov, A. A.; Jalil, R.; Morozov, S. V.; Novoselov, K. S.; Grigorieva, I. V.; Hill, E. H.; Cheianov, V. V.; Falko, V. I.; Watanabe, K.; Taniguchi, T.; Gorbachev, R. V. *Nat Phys* **2011,** 7, (12), 958-961.
3. Zan, R.; Bangert, U.; Ramasse, Q.; Novoselov, K. S. *Journal of Physical Chemistry Letters* **2012,** 3, 953-958.
4. Ramasse, Q. M.; Zan, R.; Bangert, U.; Boukhvalov, D. W.; Son, Y. W.; Novoselov, K. S. *ACS Nano* **2012**, 6, (3), 4063-4071.

5. Severin, N.; Kirstein, S.; Sokolov, I. M.; Rabe, J. P. *Nano Letters* **2008,** 9, (1), 457-461.
6. Booth, T. J.; Pizzocchero, F.; Andersen, H.; Hansen, T. W.; Wagner, J. B.; Jinschek, J. R.; Dunin-Borkowski, R. E.; Hansen, O.; Boggild, P. *Nano Letters* **2011,** 11, (7), 2689-2692.
7. Dimiev, A.; Kosynkin, D. V.; Sinitskii, A.; Slesarev, A.; Sun, Z.; Tour, J. M. *Science* **2011,** 331, (6021), 1168-1172.
8. Biró, L. P.; Lambin, P. *Carbon* **2010,** 48, (10), 2677-2689.
9. Chan, K. T.; Neaton, J. B.; Cohen, M. L. *Physical Review B* **2008,** 77, (23), 235430.
10. Xu, Z. Nano-Engineering of Graphene and Related Materials. In *Physics and Applications of Graphene - Experiments*; Mikhailov, S., Ed., InTech: Rijeka, Croatia, **2011**, 3-22.
11. Hashimoto, A.; Suenaga, K.; Gloter, A.; Urita, K.; Iijima, S. *Nature* **2004,** 430, (7002), 870-873.
12. Meyer, J. C.; Kisielowski, C.; Erni, R.; Rossell, M. D.; Crommie, M. F.; Zettl, A. *Nano Letters* **2008,** 8, (11), 3582-3586.
13. Girit, C. O.; Meyer, J. C.; Erni, R.; Rossell, M. D.; Kisielowski, C.; Yang, L.; Park, C.-H.; Crommie, M. F.; Cohen, M. L.; Louie, S. G.; Zettl, A. *Science* **2009,** 323, (5922), 1705-1708.
14. Banhart, F.; Kotakoski, J.; Krasheninnikov, A. V. *ACS Nano* **2011,** 5, (1), 26-41.
15. Kotakoski, J.; Krasheninnikov, A. V.; Kaiser, U.; Meyer, J. C. *Physical Review Letters* **2011,** 106, (10), 105505.
16. Kotakoski, J.; Meyer, J. C.; Kurasch, S.; Santos-Cottin, D.; Kaiser, U.; Krasheninnikov, A. V. *Physical Review B* **2011,** 83, (24), 245420.
17. Gass, M. H.; Bangert, U.; Bleloch, A. L.; Wang, P.; Nair, R. R.; Geim, A. K. *Nat Nano* **2008,** 3, (11), 676-681.
18. Crespi, V. H.; Benedict, L. X.; Cohen, M. L.; Louie, S. G. *Physical Review B* **1996,** 53, (20), R13303-R13305.
19. Terrones, H.; Terrones, M.; Hernandez, E.; Grobert, N.; Charlier, J. C.; Ajayan, P. M. *Physical Review Letters* **2000,** 84, (8), 1716-1719.
20. Ewels, C. P.; Heggie, M. I.; Briddon, P. R. *Chemical Physics Letters* **2002,** 351, (3-4), 178-182.
21. Lee, G.-D.; Wang, C. Z.; Yoon, E.; Hwang, N.-M.; Kim, D.-Y.; Ho, K. M. *Physical Review Letters* **2005,** 95, (20), 205501.
22. Krasheninnikov, A. V.; Banhart, F. *Nat Mater* **2007,** 6, (10), 723-733.
23. Jeong, B. W.; Ihm, J.; Lee, G.-D. *Physical Review B* **2008,** 78, (16), 165403.
24. Lusk, M. T.; Carr, L. D. *Physical Review Letters* **2008,** 100, (17), 175503.
25. Kim, Y.; Ihm, J.; Yoon, E.; Lee, G.-D. *Physical Review B* **2011,** 84, (7), 075445.
26. Krivanek, O. L.; Dellby, N.; Murfitt, M. F.; Chisholm, M. F.; Pennycook, T. J.; Suenaga, K.; Nicolosi, V. *Ultramicroscopy* **2010,** 110, (8), 935-945.
27. Krivanek, O. L.; Chisholm, M. F.; Nicolosi, V.; Pennycook, T. J.; Corbin, G. J.; Dellby, N.; Murfitt, M. F.; Own, C. S.; Szilagyi, Z. S.; Oxley, M. P.; Pantelides, S. T.; Pennycook, S. J. *Nature* **2010,** 464, (7288), 571-574.

28. Warner, J. H.; Rummeli, M. H.; Ge, L.; Gemming, T.; Montanari, B.; Harrison, N. M.; Buchner, B.; Briggs, G. A. D. *Nat Nano* **2009,** 4, (8), 500-504.
29. Russo, C. J.; Golovchenko, J. A. *Proceedings of the National Academy of Sciences* **2012**, DOI: 10.1073/pnas.1119827109.
30. Li, X.; Cai, W.; An, J.; Kim, S.; Nah, J.; Yang, D.; Piner, R.; Velamakanni, A.; Jung, I.; Tutuc, E.; Banerjee, S. K.; Colombo, L.; Ruoff, R. S. *Science* **2009,** 324, (5932), 1312-1314.
31. van Dorp, W. F.; Zhang, X.; Feringa, B. L.; Wagner, J. B.; Hansen, T. W.; De Hosson, J. Th. M. *Nanotechnology* **2011,** 22, 505303.
32. Barreiro, A.; Boerrnert, F.; Avdoshenko, S. M.; Rellinghaus, B.; Cuniberti, G.; Ruemmeli, M. H.; Vandersypen, L. M. K. *arXiv:1201.3131v1* **2012**.
33. Zan, R.; Bangert, U.; Ramasse, Q.; Novoselov, K. S. *Nano Letters* **2011,** 11, (3), 1087-1092.
34. Ishizuka, K.; Abe, E. *Proc. of the 13th European Microscopy Congress, Instrumentation and Methodology* **2004,** 1, 117.
35. Zan, R.; Bangert, U.; Ramasse, Q.; Novoselov, K. S. *Journal of Microscopy* **2011,** 244, (2), 152-158.

7.4 Conclusions

Graphene etching was observed for all studied metals (Cr, Ti, Pd, Ni and Al) except Au. It was also observed in presence of unintentional Si impurities on the pristine samples. Deposited metals were seen to cluster exclusively on hydrocarbon contamination patches rather than on clean graphene areas. However, individual metal atoms could occasionally be dragged by the electron beam to the edge of the contamination patches and therefore placed in close contact with the clean graphene surface. As a result of the interaction between graphene and these metal atoms, nano holes were formed in the suspended graphene. Although it is know that the defect formation energies in graphene are substantially lowered in the mere presence of metal atoms, the actual etching mechanism at play here is not fully resolved. An oxidation mechanism may provide the most likely explanation, whereby oxygen released from nearby contamination may lead to a C-C bond dissociation mediated by the oxidation of the metal atoms. Our recent DFT calculations (unpublished work) may further support this scenario: the chemisorption energies of hydrogen and oxygen atoms onto the surface of graphene demonstrate a visible decrease in the presence of all studied metals compared to a pristine graphene sheet, even for very sparse oxygen or hydrogen environments.

Following this etching behaviour, once the metal atom reservoir is exhausted, the holes can be spontaneously mended through the formation of a quasi-amorphous 2-dimensional network of carbon atom polygons, the carbon atoms necessary being supplied from nearby hydrocarbon contamination patches. The growth of this kind of highly defected structure was also observed on top of clean graphene.

These metal-mediated etching and self-healing mechanisms might open up possibilities for the use of metal nano clusters for graphene tailoring applications under the electron beam.

Chapter 8

Summary and Future Work

The work presented in this thesis was aimed at investigating graphene on the atomic scale and in particular to probe the metal-graphene interaction. The thesis started by setting the scene with background information about graphene, followed by details of graphene fabrication and suspended sample preparation along with technical information concerning TEM and STM characterizations. TEM studies of suspended pristine graphene layers are presented and complemented by first ever STM investigations of them. Then, metal behaviours on suspended graphene were investigated via TEM and STEM; these studies led to unique observations.

Graphene layers used in this research were fabricated by two techniques, which were mechanical cleavage of graphite and CVD-growth on polycrystalline copper surface. After the fabrication, wet transfer technique was used to transfer the layers to TEM grids, as suspended membranes are required for both electron and probe microscopy investigations. Graphene layer identification and atomic scale investigations were performed in TEM and STEM. Single, two and few layer graphene were differentiated via diffraction patterns as was turbostratic graphene and the rotation angles between the layers. Hexagonal periodicity and individual carbon atoms were observed in TEM and STEM operated at an acceleration voltage below the knock-on threshold of carbon in graphene. Cleanliness, surface contamination and foreign ad-atoms on the graphene layers were identified in HAADF and EELS in the STEM. Structural studies of graphene grown on copper surface were performed at liquid nitrogen temperature in the STM and atomically resolved single layer graphene, ripples, wrinkles and moiré appearance on copper surface were observed. The structure of suspended graphene layers has been investigated for the first time in the STM. Annealing conditions and imaging techniques were established that enabled to observe atomically resolved graphene structure. Additionally, ripples in graphene were seen to be static and comparable to what was observed in TEM in terms of their amplitude and wavelength.

After studies of pristine graphene in (S)TEM and STM, in the main part of the project, the behaviour of the metals Au; Cr; Ti; Ni; Al; Pd as well as of the semi-metal Si on suspended graphene surfaces were investigated. As a general behaviour, all studied metals

did not interact with the clean graphene surface as none of them were observed on clean parts of the graphene. They were mainly clustered and found to be on the hydrocarbon chains. Although these surface contaminations on the graphene can be minimized by annealing in UHV they are unavoidable when the sample exposed to the air. The size and distribution of the clusters were found to vary on the graphene for different metals, for example Au clusters were the biggest and Ti is smallest in size for the same amount of metal deposition that indicates Ti has better distribution than Au as witnessed in STEM micrographs as well. Unequal distribution and irregular size of Au clusters were amended upon chemical modification of the graphene that was hydrogenation. However, none of Au ad-atoms or clusters has been observed on clean part of the graphene surface similar to Au-pristine interaction.

On the other hand, interesting results have been witnessed for all studied metals (except Au) and Si in that they etched the graphene layer during STEM investigations. Although the metals nucleated on the hydrocarbons they were dragged by the scanning electron beam to clean parts of the graphene surface. As soon as the metal interacted with carbon atoms of the graphene a vacancy appeared followed by creation of further vacancies that ended up as a hole. This was observed although the microscope column was kept in UHV and operated at 60 kV that is below the damaging threshold of carbon. However, another phenomenon, which is more interesting than graphene etching, graphene healing was observed in the STEM. Graphene healed its holes after their evolution as a result of metal mediated etching. Different healing mechanisms were observed; when the hole was near hydrocarbons it was filled with C-polygons, however, when it was away from the contaminated regions the filling took place with hexagons.

To be able to get detailed information about metal-graphene systems, graphene should be free from any residues and contaminations that were seen to host all metal species. Although contamination on the graphene surface can be minimized by annealing in UHV, when the sample are taken out of the UHV system for metal deposition or even during transport they are contaminated. Thus, annealing, metal deposition and measurement should be performed all in situ to minimize any possible contaminations. Commercially available TEMs and STEMs are not capable of doing all these together, Future work will employ STM for such in situ studies, Metal-suspended graphene interactions in the STM are currently under investigation; these will provide new insight along with spectroscopic data which enable electronic information about these systems.

There are also more future applications regarding the metal-graphene interaction in the (S)TEM with view of nano-sculpting. Firstly, defects can be introduced either by energetic particles, oxygen plasma or acid treatment to modify graphene layers; these defects can act as nucleation centres for metal species. The modifications can be done by functionalization as well, hydrogenation, fluorination or by exposing to other gases with varying time and temperature. Implantation is another way to introduce metal species to the graphene plane that is also under investigation.

As well as graphene, other 2D materials, such as BN, MoS_2 and WS_2 and heterostructure combinations thereof are gaining more attention and are heavily under investigation to uncover properties of these new materials. Understanding structural, topographic and transport properties of 2D materials are is immensely important in overcoming difficulties with graphene based devices for the 2D electronics era.

References

[1] K. S. Novoselov, A. K. Geim, S. V. Morozov, D. Jiang, Y. Zhang, S. V. Dubonos, I. V. Grigorieva, and A. A. Firsov, Science 306 (2004) 666.

[2] R. E. Peierls, Ann. Inst. Henri Poincare 5 (1935) 177.

[3] K. S. Novoselov, A. K. Geim, S. V. Morozov, D. Jiang, M. I. Katsnelson, I. V. Grigorieva, S. V. Dubonos, and A. A. Firsov, Nature 438 (2005) 197.

[4] C. Lee, X. Wei, J. W. Kysar, and J. Hone, Science 321 (2008) 385.

[5] J. S. Bunch, S. S. Verbridge, J. S. Alden, A. M. van der Zande, J. M. Parpia, H. G. Craighead, and P. L. McEuen, Nano Letters 8 (2008) 2458.

[6] A. A. Balandin, S. Ghosh, W. Bao, I. Calizo, D. Teweldebrhan, F. Miao, and C. N. Lau, Nano Letters 8 (2008) 902.

[7] I. Meric, M. Y. Han, A. F. Young, B. Ozyilmaz, P. Kim, and K. L. Shepard, Nat Nano 3 (2008) 654.

[8] K. Pi, K. M. McCreary, W. Bao, W. Han, Y. F. Chiang, Y. Li, S. W. Tsai, C. N. Lau, and R. K. Kawakami, Physical Review B 80 (2009) 075406.

[9] A. Venugopal, L. Colombo, and E. M. Vogel, Applied Physics Letters 96 (2010) 013512.

[10] D. C. Elias, R. V. Gorbachev, A. S. Mayorov, S. V. Morozov, A. A. Zhukov, P. Blake, L. A. Ponomarenko, I. V. Grigorieva, K. S. Novoselov, F. Guinea, and A. K. Geim, Nat Phys 7 (2011) 701.

[11] S. Fratini and F. Guinea, Physical Review B 77 (2008) 195415.

[12] S. V. Morozov, K. S. Novoselov, M. I. Katsnelson, F. Schedin, D. C. Elias, J. A. Jaszczak, and A. K. Geim, Physical Review Letters 100 (2008) 016602.

[13] M. H. Gass, U. Bangert, A. L. Bleloch, P. Wang, R. R. Nair, and A. K. Geim, Nature Nano 3 (2008) 676.

[14] J. C. Meyer, A. K. Geim, M. I. Katsnelson, K. S. Novoselov, T. J. Booth, and S. Roth, Nature 446 (2007) 60.

[15] O. L. Krivanek, N. Dellby, M. F. Murfitt, M. F. Chisholm, T. J. Pennycook, K. Suenaga, and V. Nicolosi, Ultramicroscopy 110 (2010) 935.

[16] L. C. Campos, V. R. Manfrinato, J. D. Sanchez-Yamagishi, J. Kong, and P. Jarillo-Herrero, Nano Letters 9 (2009) 2600.

[17] Z. M. Ao, Q. Jiang, R. Q. Zhang, T. T. Tan, and S. Li, J. Appl. Phys. 105 (2009) 074307.

[18] R. Zan, U. Bangert, Q. Ramasse, and K. S. Novoselov, Nano Letters 11 (2011) 1087.

[19] R. Zan, U. Bangert, Q. Ramasse, and K. S. Novoselov, Small 7 (2011) 2868.

[20] R. Zan, C. Muryn, U. Bangert, P. Mattocks, P. Wincott, D. Vaughan, X. Li, L. Colombo, R. S. Ruoff, B. Hamilton, and K. S. Novoselov, Nanoscale 4 (2012) 3065.

[21] Q. M. Ramasse, R. Zan, U. Bangert, D. W. Boukhvalov, Y.-W. Son, and K. S. Novoselov, ACS Nano 6 (2012) 4063.

[22] D. W. Boukhvalov and M. I. Katsnelson, Applied Physics Letters 95 (2009) 023109.

[23] R. Zan, U. Bangert, Q. Ramasse, and K. S. Novoselov, The Journal of Physical Chemistry Letters 3 (2012) 953.

[24] R. Zan, Q. M. Ramasse, U. Bangert, and K. S. Novoselov, Nano Letters 12 (2012) 3936.

[25] A. K. Geim and K. S. Novoselov, Nature Mater 6 (2007) 183.

[26] K. S. Novoselov, Z. Jiang, Y. Zhang, S. V. Morozov, H. L. Stormer, U. Zeitler, J. C. Maan, G. S. Boebinger, P. Kim, and A. K. Geim, Science 315 (2007) 1379.

[27] R. R. Nair, P. Blake, A. N. Grigorenko, K. S. Novoselov, T. J. Booth, T. Stauber, N. M. R. Peres, and A. K. Geim, Science 320 (2008) 1308.

[28] K. S. Novoselov, V. I. Falko, L. Colombo, P. R. Gellert, M. G. Schwab, and K. Kim, Nature 490 (2012) 192.

[29] A. S. Mayorov, R. V. Gorbachev, S. V. Morozov, L. Britnell, R. Jalil, L. A. Ponomarenko, P. Blake, K. S. Novoselov, K. Watanabe, T. Taniguchi, and A. K. Geim, Nano Letters 11 (2011) 2396.

[30] B. Guo, L. Fang, B. Zhang, and J. R. Gong, Insciences J. 1 (2011) 80.

[31] T. O. Wehling, M. I. Katsnelson, and A. I. Lichtenstein, Physical Review B 80 (2009) 085428.

[32] M. Y. Han, B. Ozyilmaz, Y. Zhang, and P. Kim, Physical Review Letters 98 (2007) 206805.

[33] Y.-W. Son, M. L. Cohen, and S. G. Louie, Physical Review Letters 97 (2006) 216803.

[34] O. V. Yazyev and S. G. Louie, Nature Mater 9 (2010) 806.

[35] X. Dong, Y. Shi, Y. Zhao, D. Chen, J. Ye, Y. Yao, F. Gao, Z. Ni, T. Yu, Z. Shen, Y. Huang, P. Chen, and L.-J. Li, Physical Review Letters 102 (2009) 135501.

[36] G. Giovannetti, P. A. Khomyakov, G. Brocks, V. M. Karpan, J. van den Brink, and P. J. Kelly, Physical Review Letters 101 (2008) 026803.

[37] H. Liu, Y. Liu, and D. Zhu, Journal of Materials Chemistry 21 (2011) 3335.

[38] T. Ohta, A. Bostwick, T. Seyller, K. Horn, and E. Rotenberg, Science 313 (2006) 951.

[39] Y.-W. Son, M. L. Cohen, and S. G. Louie, Nature 444 (2006) 347.

[40] Z. H. Ni, T. Yu, Y. H. Lu, Y. Y. Wang, Y. P. Feng, and Z. X. Shen, ACS Nano 2 (2008) 2301.

[41] G. Giovannetti, P. A. Khomyakov, G. Brocks, P. J. Kelly, and J. van den Brink, Physical Review B 76 (2007) 073103.

[42] S. Y. Zhou, G. H. Gweon, A. V. Fedorov, P. N. First, W. A. de Heer, D. H. Lee, F. Guinea, A. H. Castro Neto, and A. Lanzara, Nature Mater 6 (2007) 770.

[43] L. S. Panchakarla, K. S. Subrahmanyam, S. K. Saha, A. Govindaraj, H. R. Krishnamurthy, U. V. Waghmare, and C. N. R. Rao, Advanced Materials 21 (2009) 4726.

[44] F. Yavari, C. Kritzinger, C. Gaire, L. Song, H. Gulapalli, T. Borca-Tasciuc, P. M. Ajayan, and N. Koratkar, Small 6 (2010) 2535.

[45] D. C. Elias, R. R. Nair, T. M. G. Mohiuddin, S. V. Morozov, P. Blake, M. P. Halsall, A. C. Ferrari, D. W. Boukhvalov, M. I. Katsnelson, A. K. Geim, and K. S. Novoselov, Science 323 (2009) 610.

[46] R. Balog, B. Jorgensen, L. Nilsson, M. Andersen, E. Rienks, M. Bianchi, M. Fanetti, E. Laegsgaard, A. Baraldi, S. Lizzit, Z. Sljivancanin, F. Besenbacher, B. Hammer, T. G. Pedersen, P. Hofmann, and L. Hornekaer, Nature Mater 9 (2010) 315.

[47] Y. G. Zhou, X. T. Zu, F. Gao, H. F. Lv, and H. Y. Xiao, Applied Physics Letters 95 (2009) 123119.

[48] R. R. Nair, W. Ren, R. Jalil, I. Riaz, V. G. Kravets, L. Britnell, P. Blake, F. Schedin, A. S. Mayorov, S. Yuan, M. I. Katsnelson, H.-M. Cheng, W. Strupinski, L. G. Bulusheva, A. V. Okotrub, I. V. Grigorieva, A. N. Grigorenko, K. S. Novoselov, and A. K. Geim, Small 6 (2010) 2877.

[49] E. McCann, Physical Review B 74 (2006) 161403.

[50] Y. Zhang, T.-T. Tang, C. Girit, Z. Hao, M. C. Martin, A. Zettl, M. F. Crommie, Y. R. Shen, and F. Wang, Nature 459 (2009) 820.

[51] F. Xia, D. B. Farmer, Y.-m. Lin, and P. Avouris, Nano Letters 10 (2010) 715.

[52] C. R. Dean, A. F. Young, I. Meric, C. Lee, L. Wang, S. Sorgenfrei, K. Watanabe, T. Taniguchi, P. Kim, K. L. Shepard, and J. Hone, Nature Nano 5 (2010) 722.

[53] K. I. Bolotin, K. J. Sikes, Z. Jiang, M. Klima, G. Fudenberg, J. Hone, P. Kim, and H. L. Stormer, Solid State Communications 146 (2008) 351.

[54] L. A. Ponomarenko, A. K. Geim, A. A. Zhukov, R. Jalil, S. V. Morozov, K. S. Novoselov, I. V. Grigorieva, E. H. Hill, V. V. Cheianov, V. I. Falko, K. Watanabe, T. Taniguchi, and R. V. Gorbachev, Nature Phys 7 (2011) 958.

[55] L. Britnell, R. V. Gorbachev, R. Jalil, B. D. Belle, F. Schedin, A. Mishchenko, T. Georgiou, M. I. Katsnelson, L. Eaves, S. V. Morozov, N. M. R. Peres, J. Leist, A. K. Geim, K. S. Novoselov, and L. A. Ponomarenko, Science 335 (2012) 947.

[56] C. Jin, F. Lin, K. Suenaga, and S. Iijima, Physical Review Letters 102 (2009) 195505.

[57] X. Liang, B. A. Sperling, I. Calizo, G. Cheng, C. A. Hacker, Q. Zhang, Y. Obeng, K. Yan, H. Peng, Q. Li, X. Zhu, H. Yuan, A. R. Hight Walker, Z. Liu, L.-M. Peng, and C. A. Richter, ACS Nano 5 (2011) 9144.

[58] J. W. Suk, A. Kitt, C. W. Magnuson, Y. Hao, S. Ahmed, J. An, A. K. Swan, B. B. Goldberg, and R. S. Ruoff, ACS Nano 5 (2011) 6916.

[59] S. Bae, H. Kim, Y. Lee, X. Xu, J.-S. Park, Y. Zheng, J. Balakrishnan, T. Lei, H. Ri Kim, Y. I. Song, Y.-J. Kim, K. S. Kim, B. Ozyilmaz, J.-H. Ahn, B. H. Hong, and S. Iijima, Nature Nano 5 (2010) 574.

[60] M. D. Stoller, S. Park, Y. Zhu, J. An, and R. S. Ruoff, Nano Letters 8 (2008) 3498.

[61] E. Yoo, J. Kim, E. Hosono, H.-s. Zhou, T. Kudo, and I. Honma, Nano Letters 8 (2008) 2277.

[62] F. Xia, T. Mueller, Y.-m. Lin, A. Valdes-Garcia, and P. Avouris, Nat Nano 4 (2009) 839.

[63] A. N. Grigorenko, M. Polini, and K. S. Novoselov, Nature Photon 6 (2012) 749.

[64] S. Stankovich, D. A. Dikin, G. H. B. Dommett, K. M. Kohlhaas, E. J. Zimney, E. A. Stach, R. D. Piner, S. T. Nguyen, and R. S. Ruoff, Nature 442 (2006) 282.

[65] F. Schedin, A. K. Geim, S. V. Morozov, E. W. Hill, P. Blake, M. I. Katsnelson, and K. S. Novoselov, Nature Mater 6 (2007) 652.

[66] R. S. Pantelic, J. C. Meyer, U. Kaiser, and H. Stahlberg, Solid State Communications 152 (2012) 1375.

[67] T. Ramanathan, A. A. Abdala, S. Stankovich, D. A. Dikin, M. Herrera Alonso, R. D. Piner, D. H. Adamson, H. C. Schniepp, X. Chen, R. S. Ruoff, S. T. Nguyen, I. A. Aksay, R. K. Prud'Homme, and L. C. Brinson, Nature Nano 3 (2008) 327.

[68] C. Liu, Z. Yu, D. Neff, A. Zhamu, and B. Z. Jang, Nano Letters 10 (2010) 4863.

[69] J. H. Warner, M. H. Rummeli, A. Bachmatiuk, M. Wilson, and B. Bunchner, ACS Nano 4 (2009) 470.

[70] J. Sloan, Z. Liu, K. Suenaga, N. R. Wilson, P. A. Pandey, L. M. Perkins, J. P. Rourke, and I. J. Shannon, Nano Letters 10 (2010) 4600.

[71] R. R. Nair, P. Blake, J. R. Blake, R. Zan, S. Anissimova, U. Bangert, A. P. Golovanov, S. V. Morozov, A. K. Geim, K. S. Novoselov, and T. Latychevskaia, Applied Physics Letters 97 (2010) 153102.

[72] H. W. C. Postma, Nano Letters 10 (2010) 420.

[73] J. C. Meyer, C. O. Girit, M. F. Crommie, and A. Zettl, Nature 454 (2008) 319.

[74] Z. Lee, K.-J. Jeon, A. Dato, R. Erni, T. J. Richardson, M. Frenklach, and V. Radmilovic, Nano Letters 9 (2009) 3365.

[75] Z. Sun, D. K. James, and J. M. Tour, The Journal of Physical Chemistry Letters 2 (2011) 2425.

[76] C. Berger, Z. Song, X. Li, X. Wu, N. Brown, C. c. Naud, D. Mayou, T. Li, J. Hass, A. N. Marchenkov, E. H. Conrad, P. N. First, and W. A. de Heer, Science 312 (2006) 1191.

[77] A. Reina, X. Jia, J. Ho, D. Nezich, H. Son, V. Bulovic, M. S. Dresselhaus, and J. Kong, Nano Letters 9 (2008) 30.

[78] X. Li, W. Cai, J. An, S. Kim, J. Nah, D. Yang, R. Piner, A. Velamakanni, I. Jung, E. Tutuc, S. K. Banerjee, L. Colombo, and R. S. Ruoff, Science 324 (2009) 1312.

[79] H. Ago, Y. Ogawa, M. Tsuji, S. Mizuno, and H. Hibino, The Journal of Physical Chemistry Letters 3 (2012) 2228.

[80] G. Eda, G. Fanchini, and M. Chhowalla, Nature Nano 3 (2008) 270.

[81] Y. Hernandez, V. Nicolosi, M. Lotya, F. M. Blighe, Z. Sun, S. De, I. T. McGovern, B. Holland, M. Byrne, Y. K. Gun'Ko, J. J. Boland, P. Niraj, G. Duesberg, S. Krishnamurthy, R. Goodhue, J. Hutchison, V. Scardaci, A. C. Ferrari, and J. N. Coleman, Nature Nano 3 (2008) 563.

[82] M. Lotya, Y. Hernandez, P. J. King, R. J. Smith, V. Nicolosi, L. S. Karlsson, F. M. Blighe, S. De, Z. Wang, I. T. McGovern, G. S. Duesberg, and J. N. Coleman, Journal of the American Chemical Society 131 (2009) 3611.

[83] A. T. N'Diaye, S. Bleikamp, P. J. Feibelman, and T. Michely, Physical Review Letters 97 (2006) 215501.

[84] Z. Zhou, F. Gao, and D. W. Goodman, Surface Science 604 (2010) L31.

[85] L. Gao, J. R. Guest, and N. P. Guisinger, Nano Letters 10 (2010) 3512.

[86] Y. Zhu, S. Murali, W. Cai, X. Li, J. W. Suk, J. R. Potts, and R. S. Ruoff, Advanced Materials 22 (2010) 3906.

[87] J. N. Coleman, M. Lotya, A. O'Neill, S. D. Bergin, P. J. King, U. Khan, K. Young, A. Gaucher, S. De, R. J. Smith, I. V. Shvets, S. K. Arora, G. Stanton, H.-Y. Kim, K. Lee, G. T. Kim, G. S. Duesberg, T. Hallam, J. J. Boland, J. J. Wang, J. F. Donegan, J. C. Grunlan, G. Moriarty, A. Shmeliov, R. J. Nicholls, J. M. Perkins, E. M. Grieveson, K. Theuwissen, D. W. McComb, P. D. Nellist, and V. Nicolosi, Science 331 (2011) 568.

[88] P. Blake, E. W. Hill, A. H. C. Neto, K. S. Novoselov, D. Jiang, R. Yang, T. J. Booth, and A. K. Geim, Applied Physics Letters 91 (2007) 063124.

[89] A. C. Ferrari, J. C. Meyer, V. Scardaci, C. Casiraghi, M. Lazzeri, F. Mauri, S. Piscanec, D. Jiang, K. S. Novoselov, S. Roth, and A. K. Geim, Physical Review Letters 97 (2006) 187401.

[90] T. Eberlein, U. Bangert, R. R. Nair, R. Jones, M. Gass, A. L. Bleloch, K. S. Novoselov, A. Geim, and P. R. Briddon, Physical Review B 77 (2008) 233406.

[91] X. Jia, J. Campos-Delgado, M. Terrones, V. Meunier, and M. S. Dresselhaus, Nanoscale 3 (2011) 86.

[92] J. C. Meyer, A. K. Geim, M. I. Katsnelson, K. S. Novoselov, D. Obergfell, S. Roth, C. Girit, and A. Zettl, Solid State Communications 143 (2007) 101.

[93] F. Banhart, J. Kotakoski, and A. V. Krasheninnikov, ACS Nano 5 (2011) 26.

[94] C. P. Ewels, M. I. Heggie, and P. R. Briddon, Chemical Physics Letters 351 (2002) 178.

[95] A. Hashimoto, K. Suenaga, A. Gloter, K. Urita, and S. Iijima, Nature 430 (2004) 870.

[96] K. Suenaga, K. Akiyama-Hasegawa, Y. Niimi, H. Kobayashi, M. Nakamura, Z. Liu, Y. Sato, M. Koshino, and S. Iijima, Journal of Electron Microscopy 61 (2012) 285.

[97] H. Wang, Q. Wang, Y. Cheng, K. Li, Y. Yao, Q. Zhang, C. Dong, P. Wang, U. Schwingenschlogl, W. Yang, and X. X. Zhang, Nano Letters 12 (2012) 141.

[98] H. Tao, J. Moser, F. Alzina, Q. Wang, and C. M. Sotomayor-Torres, The Journal of Physical Chemistry C 115 (2011) 18257.

[99] A. Dimiev, D. V. Kosynkin, A. Sinitskii, A. Slesarev, Z. Sun, and J. M. Tour, Science 331 (2011) 1168.

[100] P. Y. Huang, C. S. Ruiz-Vargas, A. M. van der Zande, W. S. Whitney, M. P. Levendorf, J. W. Kevek, S. Garg, J. S. Alden, C. J. Hustedt, Y. Zhu, J. Park, P. L. McEuen, and D. A. Muller, Nature 469 (2011) 389.

[101] J. Kotakoski, A. V. Krasheninnikov, U. Kaiser, and J. C. Meyer, Physical Review Letters 106 (2011) 105505.

[102] C. J. Russo and J. A. Golovchenko, Proceedings of the National Academy of Sciences (2012)

[103] J. C. Meyer, C. Kisielowski, R. Erni, M. D. Rossell, M. F. Crommie, and A. Zettl, Nano Letters 8 (2008) 3582.

[104] A. V. Krasheninnikov, P. O. Lehtinen, A. S. Foster, and R. M. Nieminen, Chemical Physics Letters 418 (2006) 132.

[105] H. Terrones, M. Terrones, E. Hernandez, N. Grobert, J. C. Charlier, and P. M. Ajayan, Physical Review Letters 84 (2000) 1716.

[106] A. J. Stone and D. J. Wales, Chemical Physics Letters 128 (1986) 501.

[107] C. O. Girit, J. C. Meyer, R. Erni, M. D. Rossell, C. Kisielowski, L. Yang, C.-H. Park, M. F. Crommie, M. L. Cohen, S. G. Louie, and A. Zettl, Science 323 (2009) 1705.

[108] X. Wang and H. Dai, Nature Chem 2 (2010) 661.

[109] M. Pan, E. C. Girao, X. Jia, S. Bhaviripudi, Q. Li, J. Kong, V. Meunier, and M. S. Dresselhaus, Nano Letters 12 (2012) 1928.

[110] B. Song, G. F. Schneider, Q. Xu, G. Pandraud, C. Dekker, and H. Zandbergen, Nano Letters 11 (2011) 2247.

[111] N. Severin, S. Kirstein, I. M. Sokolov, and J. P. Rabe, Nano Letters 9 (2008) 457.

[112] T. J. Booth, F. Pizzocchero, H. Andersen, T. W. Hansen, J. B. Wagner, J. R. Jinschek, R. E. Dunin-Borkowski, O. Hansen, and P. Boggild, Nano Letters 11 (2011) 2689.

[113] D. V. Kosynkin, A. L. Higginbotham, A. Sinitskii, J. R. Lomeda, A. Dimiev, B. K. Price, and J. M. Tour, Nature 458 (2009) 872.

[114] Y. C. Cheng, H. T. Wang, Z. Y. Zhu, Y. H. Zhu, Y. Han, X. X. Zhang, and U. Schwingenschlogl, Physical Review B 85 (2012) 073406.

[115] J. Kotakoski, D. Santos-Cottin, and A. V. Krasheninnikov, ACS Nano 6 (2012) 671.

[116] P. Koskinen, S. Malola, and H. Hakkinen, Physical Review B 80 (2009) 073401.

[117] Y. Gan, L. Sun, and F. Banhart, Small 4 (2008) 587.

[118] R. Varns and P. Strange, Journal of Physics: Condensed Matter 20 (2008) 225005.

[119] S. Malola, H. Hakkinen, and P. Koskinen, Applied Physics Letters 94 (2009) 043106.

[120] A. V. Krasheninnikov, P. O. Lehtinen, A. S. Foster, P. Pyykko, and R. M. Nieminen, Physical Review Letters 102 (2009) 126807.

[121] M. Zhou, A. Zhang, Z. Dai, C. Zhang, and Y. P. Feng, The Journal of Chemical Physics 132 (2010) 194704.

[122] O. Cretu, A. V. Krasheninnikov, J. A. Rodriguez-Manzo, L. Sun, R. M. Nieminen, and F. Banhart, Physical Review Letters 105 (2010) 196102.

[123] J. A. Rodriguez-Manzo, O. Cretu, and F. Banhart, ACS Nano 4 (2010) 3422.

[124] U. Akturk, Olcay and M. Tomak, Physical Review B 80 (2009) 085417.

[125] K. T. Chan, J. B. Neaton, and M. L. Cohen, Physical Review B 77 (2008) 235430.

[126] Y. Okamoto, Chemical Physics Letters 420 (2006) 382.

[127] M. Zhou, A. Zhang, Z. Dai, Y. P. Feng, and C. Zhang, The Journal of Physical Chemistry C 114 (2010) 16541.

[128] H. Wang, K. Li, Y. Cheng, Q. Wang, Y. Yao, U. Schwingenschlogl, X. Zhang, and W. Yang, Nanoscale 4 (2012) 2920.

[129] R. Erni, M. D. Rossell, M.-T. Nguyen, S. Blankenburg, D. Passerone, P. Hartel, N. Alem, K. Erickson, W. Gannett, and A. Zettl, Physical Review B 82 (2010) 165443.

[130] A. V. Krasheninnikov and F. Banhart, Nature Mater 6 (2007) 723.

[131] O. Cretu, J. A. Rodriguez-Manzo, A. Demortiere, and F. Banhart, Carbon 50 (2012) 259.

[132] L. P. Biró and P. Lambin, Carbon 48 (2010) 2677.

[133] L. Ci, Z. Xu, L. Wang, W. Gao, F. Ding, K. Kelly, B. Yakobson, and P. Ajayan, Nano Research 1 (2008) 116.

[134] S. S. Datta, D. R. Strachan, S. M. Khamis, and A. T. C. Johnson, Nano Letters 8 (2008) 1912.

[135] L. Gao, W. Ren, B. Liu, Z.-S. Wu, C. Jiang, and H.-M. Cheng, Journal of the American Chemical Society 131 (2009) 13934.

[136] P. Nemes-Incze, G. Magda, K. Kamaras, and L. Biro, Nano Research 3 (2010) 110.

[137] L. Liu, S. Ryu, M. R. Tomasik, E. Stolyarova, N. Jung, M. S. Hybertsen, M. L. Steigerwald, L. E. Brus, and G. W. Flynn, Nano Letters 8 (2008) 1965.

[138] L. J. H. Eduardo, K. Balasubramanian, R. T. Weitz, M. Burghard, and K. Kern, Nature Nano 3 (2008) 486.

[139] C. Gong, Lee Geunsik, B. Shan, E. Vogel, M. , R. M. Wallace, and K. Cho, J. Appl. Phys 108 (2010) 123711.

[140] C. Gong, D. Hinojos, W. Wang, N. Nijem, B. Shan, R. M. Wallace, K. Cho, and Y. J. Chabal, ACS Nano 6 (2012) 5381.

[141] A. D. Franklin, H. Shu-Jen, A. A. Bol, and V. Perebeinos, Electron Device Letters, IEEE 33 (2012) 17.

[142] O. Leenaerts, B. Partoens, and F. M. Peeters, Microelectronics Journal 40 (2009) 860.

[143] B. Huard, N. Stander, J. A. Sulpizio, and D. Goldhaber-Gordon, Physical Review B 78 (2008) 121402.

[144] K. M. McCreary, K. Pi, A. G. Swartz, W. Han, W. Bao, C. N. Lau, F. Guinea, M. I. Katsnelson, and R. K. Kawakami, Physical Review B 81 (2010) 115453.

[145] J. C. Charlier, L Arnaud, I. V. Avilov, M. Delgado, F. Demoisson, E. H. Espinosa, C. P. Ewels, A. Felten, J. Guillot, R. Ionescu, R. Leghrib, E. Llobet, A. Mansour, H-N. Migeon, J. J. Pireaux, F. Reniers, I. Suarez-Martinez, G. E. Watson, and Z. Zanolli, Nanotechnology 20 (2009) 375501.

[146] H. Pinto, R. Jones, J. P. Goss, and P. R. Briddon, Physica Status Solidi (a) 207 (2010) 2131.

[147] Y. Mao, G. M. Stocks, and J. Zhong, New Journal of Physics 12 (2010) 033046.

[148] J. H. Chen, C. Jang, S. Adam, M. S. Fuhrer, E. D. Williams, and M. Ishigami, Nature Phys 4 (2008) 377.

[149] J. Lee, K. S. Novoselov, and H. S. Shin, ACS Nano 5 (2011) 608.

[150] F. Schedin, E. Lidorikis, A. Lombardo, V. G. Kravets, A. K. Geim, A. N. Grigorenko, K. S. Novoselov, and A. C. Ferrari, ACS Nano 4 (2010) 5617.

[151] J. Lee, S. Shim, B. Kim, and H. S. Shin, Chemistry – A European Journal 17 (2012) 2381.

[152] J. Huang, L. Zhang, B. Chen, N. Ji, F. Chen, Y. Zhang, and Z. Zhang, Nanoscale 2 (2010) 2733.

[153] A. N'Diaye, T., T. Gerber, C. Busse, J. Myslivecek, J. Coraux, and T. Michely, New Journal of Physics 11 (2009) 103045.

[154] B. Premlal, M. Cranney, F. Vonau, D. Aubel, D. Casterman, M. M. De Souza, and L. Simon, Applied Physics Letters 94 (2009) 263115.

[155] M. Sicot, S. Bouvron, O. Zander, U. Rudiger, Y. S. Dedkov, and M. Fonin, Applied Physics Letters 96 (2010) 093115.

[156] E. Ganz, K. Sattler, and J. Clarke, Surface Science 219 (1989) 33.

[157] T. Irawan, I. Barke, and H. Hovel, Applied Physics A 80 (2005) 929.

[158] D. B. Williams and C. B. Carter, Transmission Electron Microscopy, Plenum Press, 1996.

[159] P. Goodhew, in Aberration-Corrected Analytical Transmission Electron Microscopy (R. Brydson, ed.), John Wiley & Sons, Ltd, 2011, p. 1.

[160] A. V. Crewe, Reports on Progress in Physics 43 (1980) 621.

[161] O. L. Krivanek, M. F. Chisholm, V. Nicolosi, T. J. Pennycook, G. J. Corbin, N. Dellby, M. F. Murfitt, C. S. Own, Z. S. Szilagyi, M. P. Oxley, S. T. Pantelides, and S. J. Pennycook, Nature 464 (2010) 571.

[162] O. L. Krivanek, W. Zhou, M. F. Chisholm, J. C. Idrobo, T. C. Lovejoy, Q. M. Ramasse, and N. Dellby, in Low Voltage Electron Microscopy, John Wiley & Sons, Ltd, 2012, p. 119.

[163] A. V. Crewe, Science 154 (1966) 729.

[164] A. V. Crewe, J. Wall, and L. M. Welter, Journal of Applied Physics 39 (1968) 5861.

[165] P. Hartel, H. Rose, and C. Dinges, Ultramicroscopy 63 (1996) 93.

[166] S. J. Pennycook, B. Rafferty, and P. D. Nellist, Microscopy and Microanalysis 6 (2000) 343.

[167] K. Ishizuka and E. Abe, Proc. of the 13th European Microscopy Congress, Instrumentation and Methodology 1 (2004) 117.

[168] R. F. Egerton, Reports on Progress in Physics 72 (2009) 016502.

[169] R. Brydson and N. Hondow, in Aberration-Corrected Analytical Transmission Electron Microscopy, John Wiley & Sons, Ltd, p. 163.

[170] G. Tatlock, in Aberration-Corrected Analytical Transmission Electron Microscopy, John Wiley & Sons, Ltd, p. 21.

[171] S. J. Haigh and A. I. Kirkland, in Aberration-Corrected Analytical Transmission Electron Microscopy, John Wiley & Sons, Ltd, p. 241.

[172] A. Bleloch and Q. Ramasse, in Aberration-Corrected Analytical Transmission Electron Microscopy, John Wiley & Sons, Ltd, p. 55.

[173] ETH, ETH Zurich, 2012, [Online] Available: http://www.microscopy.ethz.ch.

[174] M. Morgenstern, physica status solidi (b) 248 (2011) 2423.

[175] H. S. Wong, C. Durkan, and N. Chandrasekhar, ACS Nano 3 (2009) 3455.

[176] A. Luican, G. Li, and E. Y. Andrei, Solid State Communications 149 (2009) 1151.

[177] P. Xu, Y. Yang, D. Qi, S. D. Barber, J. K. Schoelz, M. L. Ackerman, L. Bellaiche, and P. M. Thibado, Physical Review B 86 (2012) 085428.

[178] S. N. Magonow and M.-H. Whangbo, Surface Analysis with STM and AFM, VCH, Veinheim, 1996.

[179] U. Bangert, M. H. Gass, A. L. Bleloch, R. R. Nair, and J. Eccles, Physica Status Solidi (a) 206 (2009) 2115.

[180] K. Suenaga and M. Koshino, Nature 468 (2010) 1088.

[181] U. Bangert, M. H. Gass, A. L. Bleloch, R. R. Nair, and A. K. Geim, Physica Status Solidi (a) 206 (2009) 1117.

[182] J. H. Warner, M. H. Rummeli, T. Gemming, B. Buchner, and G. A. D. Briggs, Nano Letters 9 (2008) 102.

[183] R. Zan, U. Bangert, Q. Ramasse, and K. S. Novoselov, Journal of Microscopy 244 (2011) 152.

[184] J. H. Warner, M. H. Rummeli, L. Ge, T. Gemming, B. Montanari, N. M. Harrison, B. Buchner, and G. A. D. Briggs, Nat Nano 4 (2009) 500.

[185] A. Chuvilin, J. Meyer C., G. Algara-Siller, and U. Kaiser, New Journal of Physics 11 (2009) 083019.

[186] S. J. Haigh, A. Gholinia, R. Jalil, S. Romani, L. Britnell, D. C. Elias, K. S. Novoselov, L. A. Ponomarenko, A. K. Geim, and R. Gorbachev, Nature Mater 11 (2012) 764.

[187] T. J. Booth, P. Blake, R. R. Nair, D. Jiang, E. W. Hill, U. Bangert, A. Bleloch, M. Gass, K. S. Novoselov, M. I. Katsnelson, and A. K. Geim, Nano Letters 8 (2008) 2442.

[188] W. L. Wang, S. Bhandari, W. Yi, D. C. Bell, R. Westervelt, and E. Kaxiras, Nano Letters 12 (2012) 2278.

[189] A. Fasolino, J. H. Los, and M. I. Katsnelson, Nature Mater 6 (2007) 858.

[190] A. J. Pollard, R. R. Nair, S. N. Sabki, C. R. Staddon, L. M. A. Perdigao, C. H. Hsu, J. M. Garfitt, S. Gangopadhyay, H. F. Gleeson, A. K. Geim, and P. H. Beton, The Journal of Physical Chemistry C 113 (2009) 16565.

[191] D. L. Miller, K. D. Kubista, G. M. Rutter, M. Ruan, W. A. de Heer, P. N. First, and J. A. Stroscio, Physical Review B 81 (2010) 125427.

[192] J. Hass, F. Varchon, J. E. Millan-Otoya, M. Sprinkle, N. Sharma, W. A. de Heer, C. Berger, P. N. First, L. Magaud, and E. H. Conrad, Physical Review Letters 100 (2008) 125504.

[193] K. Kim, V. I. Artyukhov, W. Regan, Y. Liu, M. F. Crommie, B. I. Yakobson, and A. Zettl, Nano Letters 12 (2011) 293.

[194] R. F. Egerton, R. McLeod, F. Wang, and M. Malac, Ultramicroscopy 110 (2010) 991.

[195] A. Zobelli, A. Gloter, C. P. Ewels, G. Seifert, and C. Colliex, Physical Review B 75 (2007) 245402.

[196] N. Lu, J. Wang, H. C. Floresca, and M. J. Kim, Carbon 50 (2012) 2961.

[197] Y.-C. Lin, C.-C. Lu, C.-H. Yeh, C. Jin, K. Suenaga, and P.-W. Chiu, Nano Letters 12 (2012) 414.

[198] A. Barreiro, F. Borrnert, M. H. Rummeli, B. Buchner, and L. M. K. Vandersypen, Nano Letters 12 (2012) 1873.

[199] B. Westenfelder, J. C. Meyer, J. Biskupek, S. Kurasch, F. Scholz, C. E. Krill, and U. Kaiser, Nano Letters 11 (2011) 5123.

[200] A. Barreiro, F. Boerrnert, S. M. Avdoshenko, B. Rellinghaus, G. Cuniberti, M. H. Ruemmeli, and L. M. K., Vandersypen, Arxiv (2012)

[201] E. J. Kirkland, Advanced Computing in Electron Microscopy, Plenum Press, 1998.

[202] W.-T. Pong and C. Durkan, Physical Review B 81 (2010) 045403.

[203] V. Geringer, M. Liebmann, T. Echtermeyer, S. Runte, M. Schmidt, R. Ruckamp, M. C. Lemme, and M. Morgenstern, Physical Review Letters 102 (2009) 076102.

[204] E. Stolyarova, K. T. Rim, S. Ryu, J. Maultzsch, P. Kim, L. E. Brus, T. F. Heinz, M. S. Hybertsen, and G. W. Flynn, Proceedings of the National Academy of Sciences 104 (2007) 9209.

[205] J. Cho, L. Gao, J. Tian, H. Cao, W. Wu, Q. Yu, E. N. Yitamben, B. Fisher, J. R. Guest, Y. P. Chen, and N. P. Guisinger, ACS Nano 5 (2011) 3607.

[206] I. Horcas, R. Fernandez, J. M. Gomez-Rodriguez, J. Colchero, J. Gomez-Herrero, and A. M. Baro, Review of Scientific Instruments 78 (2007) 013705.

[207] Y. Zhang, T. Gao, Y. Gao, S. Xie, Q. Ji, K. Yan, H. Peng, and Z. Liu, ACS Nano 5 (2011) 4014.

[208] H. I. Rasool, E. B. Song, M. Mecklenburg, B. C. Regan, K. L. Wang, B. H. Weiller, and J. K. Gimzewski, Journal of the American Chemical Society 133 (2011) 12536.